2021

Damping and Ejection of Sloshing Liquid Drops from Elastic Substrates

MD Erfanul Alam
University of Central Florida

DAMPING AND EJECTION OF SLOSHING LIQUID DROPS FROM ELASTIC SUBSTRATES

by

MD ERFANUL ALAM
B.S. Bangladesh University of Engineering and Technology, Mechanical Engineering, 2014
M.S. Georgia Southern University, Applied Engineering, 2017

A dissertation submitted in partial fulfilment of the requirements
for the degree of Doctor of Philosophy
in the Department of Mechanical and Aerospace Engineering
in the College of Engineering and Computer Sciences
at the University of Central Florida
Orlando, Florida

Summer Term
2021

Major Professor: Andrew Dickerson

ABSTRACT

Liquid slosh is a potential source of disturbance of the motion of a moving structure. In this thesis, we probe the damping technique of sessile drop by absorbing a portion of the kinetic energy. The sloshing dynamics are typically represented by a mechanical model of a spring mass damper. However, damping by drop sloshing is dependent on viscosity, surface tension, drop size and drop location. We explore highly-coupled fluid-solid mechanics using singular liquid drop with varying viscosity and surface tension resting on a millimetric cantilever. Cantilevers are displaced 0.6 mm and their free end is allowed to vibrate freely. Cantilever vibration causes drops to deform, or slosh, which dissipates kinetic energy via viscous dissipation within the drop. A solid weight with the same mass as experimental drops is used to compare the damping imposed by liquids, thereby accounting for other damping sources. Neither the most viscous nor least viscous drops studied imposed the greatest damping on cantilever motion. Instead, drops of intermediate viscosity strike the most effective balance of sloshing and internal dissipative capacity. The removal of pinned drops from small, delicate surfaces such as sensors and flight surfaces on micro-flyers can be challenging due to remote location and small scale and they require large deflection. Robustness is enhanced when such surfaces, of comparable scale to deposited drops, can remove deposition without external influence. Drop ejection for drops larger than the capillary length, can be a complicated, multi-stage event in which fluid removal occurs through multiple mechanisms in sequence. In this combined experimental and theoretical work, we propose drop release mechanism from elastic materials and characterization of drop sloshing damping. In our primary work, we observe three principal modes of drop release that can be singly witnessed under the appropriate set of cantilevers and drop conditions. We categorize these three release modes as sliding, normal-to-cantilever ejection, and pinch-off. We found that, the selection of system variables such as cantilever length L (a proxy for stiffness), drop location, drop size and wettability allows for the solicitation of a particular ejection mode.

This work is dedicated to my parents for their love, guidance, encouragement and unwavering support throughout my every endeavor

ACKNOWLEDGMENTS

It is with utmost gratitude that I would like to express my appreciation to those individuals who have, through their help, guidance and support allowed for the completion of my dissertation. I would like to thank:

- My Ph.D. advisor and committee chair, Dr. Andrew Dickerson for his most insightful feedback and guidance throughout the course of my doctoral research. Through his advice, I was able to overcome challenges experienced during this study. Dr. Dickerson's time, motivation and support has served as a contributing factor towards the completion of this work, for which I am most appreciative. His guidance helped me in all the time of research, preparing manuscripts for journals and writing of this thesis. I could not have imagined having a better advisor and mentor for my Ph.D study.

- My thesis committee: Dr. Jeffrey Kauffman, Dr. Dazhong Wu and Dr. Kaitlyn Crawford for their insightful comments and encouragement. Their respective questions incented me to widen my research from various perspectives.

- My parents Khorshed Alam and Fahmida Alam and my siblings Rummana Zafrin, Mashbahul Alam and Didarul Alam for their sacrifice and understanding towards the pursuit of my dreams and ambitions.

- Nicholus Smith for his peaceful company during tea breaks.

- Daren Watson for late night conversation in lab to help keep sanity.

- Kamol Roy and Kishan Neupane for their contribution in ensemble model development using machine learning.

- Milos Krsmanovic, his sense of humor encouraged me to do more lame jokes during lab time.

- All the undergraduate students who worked with me during my Ph.D tenure. Special thanks to Samuel Klener, Michael Cassette and Kevin Shitaho for helping me during the experiments and data analysis. I know how boring and tiring tracking those beam videos were.

- All the other highschool and undrgraduates who I encountered on this journey, all your time spent assisting was truly appreciated and could not be summed up in its entirety within the confines of this manuscript.

- Didarul "kArTmAN" Alam for providing invaluable mentorship and inspiration throughout my life. Thank you for those refreshing DOTA games during my hard times.

- Colonel Mohammad Naser for his continuous support and encouragement throughout my academic life.

- Don Wasi's Gang (DWG), Javala mangoes of Buet (JMB), best group of friends one could ever ask for. Thank you for your companionship, accountability and support.

- G-11 family - Nahida Apu, Ananya Apu, Shantu da, Kishan, Mehedi, Rashed and Papia, thank you for the mini tours we did together during my PhD journey.

I offer my heartfelt thanks and gratitude to all.

TABLE OF CONTENTS

LIST OF FIGURES

LIST OF TABLES

CHAPTER 1: INTRODUCTION

1.1 Motivation

Technological advancements in fabrication, manufacturing and control systems implies that robots are becoming smaller, comparable in size to insects . Micro-aerial vehicles (MAVs) range in size from 10 cm down to a few millimeters [4, 5, 6, 7]. These small flying machines are engaging for search-and-rescue and military operations because of the greater control and the ability to reach remote places which humans or traditional robots can not reach. In parallel with the engineering of MAVs, vigorous efforts continue to be made into understanding flight in the natural world, such as the flight of birds and insects [8, 9]. Translational and rotational aerodynamics explain wing motion precision and sensitivity due to the change in morphology [10, 11, 12, 13, 14, 15, 16, 17, 18, 19, 20]. Flying insects face many different environmental challenges, contending with rain, fog, dew and other airborne particles which can deposit additional mass onto the wing surface [21, 1, 22, 23]. The accumulated drops across the insect body can be many times its mass, inhibiting or preventing flight [1, 24]. Insects provide a template that we emulate, as seen in Figure 1.1. To overcome this threat, mosquitoes apply a modified wingbeat during flight startup, the flutter stroke [1]. The flutter stroke persists for approximately 4 milliseconds at nearly double the in-flight wingbeat frequency, during which the wingtip deflection is around 10 percent of a normal stroke, imparting high-accelerations in excess of 2400 gravities to particles adhered to wings. This simple yet effective technique inspires further investigation of systems where the dynamics of the substrate and fluid are coupled, enhancing the paradigm of liquid drop motion control to a greater level of complexity.

Organisms are multi-degree-of-freedom, hierarchically organized, nonlinear systems. Their response to the environmental hazard come from visual and sensory system [25, 26]. Liquid drops prevent locomotion of insect wings by adding mass, changing shape, and changing contact line

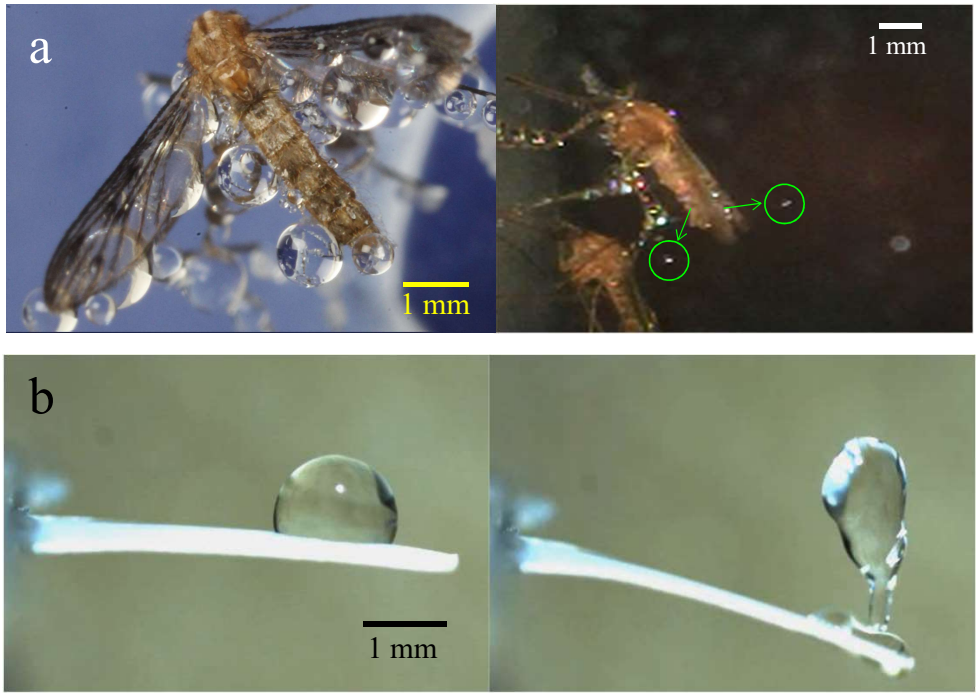

Figure 1.1: **(a)** In nature, dewfall loads flight critical surfaces with droplets. However, it has been observed [1] that mosquitoes have a special wingbeat, a 'flutter stroke,' specifically displayed for contaminant removal. **(b)** Our laboratory system, flexible polymeric cantilevers topped with drops is inspired by the mosquito.

hysteresis [27]. Generally insect wings are hydrophobic or superhydrophonic in nature [23]. It has been observed that liquid drop can move directionally in both static and dynamic states [27] which changes the drop mass and volume over time. An understanding of how liquid drops prevent natural motion of the insect wings will lead to better understanding of how the insect remove it.

1.2 Background & Previous Work

1.2.1 Damping by Drop Sloshing

Insect wings are considered to be a cantilever system. A simple cantilever motion is generally well-understood and numerous models are available to determine both aerodynamic damping [28, 29, 30] and the internal dissipation of energy[31, 32, 33]. Dissipative forces arise from the cantilever material and external forces such as air drag, decaying free vibration [34]. Mass placed at the

cantilever tip is a straightforward method to augment cantilever dynamics compared to naked cantilevers, including the nature of vibration damping. Rigid masses contribute no appreciable internal damping, but impart inertia that can prolong vibration. In contrast, particle impact dampers [35, 36, 37, 38, 39] (PIDs) hold hundreds to thousands of particles as a single concentrated mass that moves freely within a rigid shell to produce damping via particle impact [40, 41, 42], friction [42, 43, 44, 45], and hysteretic particle deformation [46, 47]. PIDs are effective over wide temperature and frequency ranges, and can be found on applications including tennis rackets[48], spacecraft [49], turbomachinary [50], and civil structures [51].

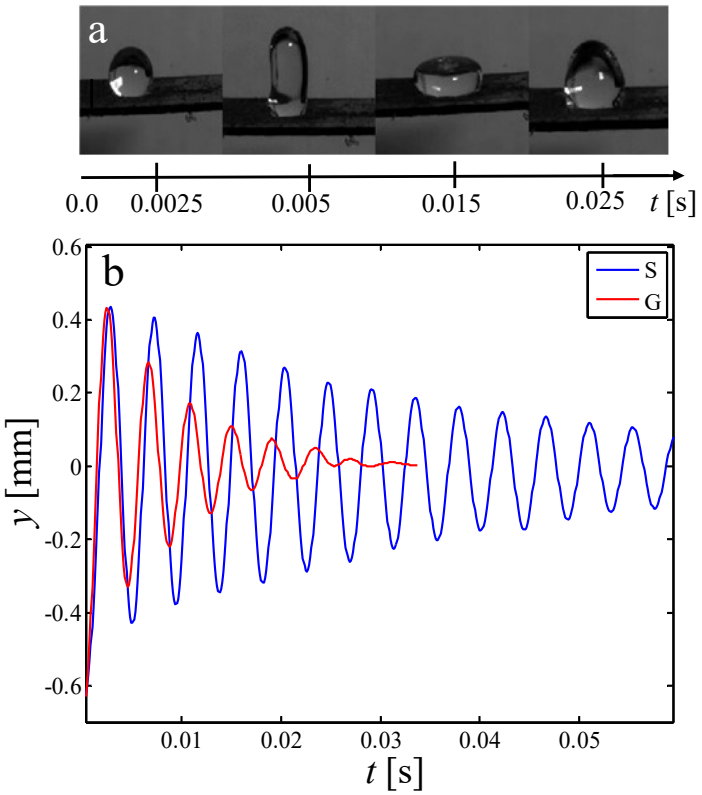

Figure 1.2: **(a)** Photo sequence of drop deformation for glycerin (G1). **(b)** Comparison of cantilever tip displacement with solid (S) and liquid (G1) masses.

Analogous to the impact of particles in a PID, liquid motion at all scales, both continuous flow and oscillatory motion, dissipates energy. Liquid sloshing in open containers with external excitation is an important phenomenon in engineering applications including trucking liquids [52, 53, 54], fuel sloshing and buffeting problems of aircraft [55, 56], and creation acoustic noise in automotive

fuel tank [57, 58, 59]. Both theoretical [60, 61, 62] and experimental [63, 64] analyses have been extensively employed to examine the physics of liquid motion damping by sloshing in a container by tracking the motion of the free surface. Energy dissipation is likewise pertinent for exceedingly small liquid bodies, singular drops. Inertial forces deform liquid drops while surface tension imparts sphericalness to gas-liquid interfaces. When a drop is deformed from equilibrium, its return to equilibrium is achieved by performing damped oscillations [65, 66, 67, 68, 69], or sloshing. The capability of drops to damp disturbances across ranges in size, viscosity, and surface tension remains understudied.

Millimetric cantilevers provide a simple dynamic system by which to investigate damping by liquid drops. Below critical accelerations, drops remain atop the cantilever and slosh, rather than eject, as the cantilever vibrates. At this scale, drops behave similar to miniature PIDs by contributing a mass which deforms with cantilever motion [70, 71, 67] as pictured in Figure 1.2a. A qualitative visual of drop damping compared to a solid mass of equivalent weight can be seen in Figure 1.2b. Surface tension constrains drop flow while governing an equilibrium shape. Viscosity acts in concert to further restrain flow and dissipate energy. Damping by a sloshing drop has been quantified for very narrow conditions when the cantilever base is excited in first-mode vibration [67, 72]. Damping by drops is known to depend on base frequency, cantilever surface wettability, drop position, drop size, and liquid viscosity [67, 72]. With a fixed cantilever base, free vibration is induced by an initial deflection of the free end.

1.2.2 Insect Flight Sensors and Wing-beat Modification

Some applications will require the removal of fluids from a solid substrate altogether. An example of the criticality of mass removal is the maintenance of small flight surfaces clean of debris, including moisture deposited from rain or dewfall [1, 73, 74]. For small flyers, such as insects and burgeoning robots of similar scale, the threat tendered by accumulated drops on flight surfaces is severe because the addition of mass alters both wing aerodynamics and the dynamics of motion. These small bodies

are tuned to operate within a narrow window of conditions [75, 76, 77, 78]. What is an effective method to quickly dry small surfaces with little input? Inspiration for our system of study comes from Dickerson *et al* (2014) [1], who made the observation that wet mosquitoes employ a modified wingbeat at flight startup to remove moisture. This maneuver is comparable to forcibly driving a free beam near one of its harmonic modes, such that free end deflection is greater than the fixed end. This 'flutter stroke' creates dramatic deflection in a mosquito's wings and disperses a number of small drops in milliseconds, as shown Figure 1.3a. During the flutter stroke phase lasting 4 ms, the wings beat at 875 Hz, more than twice the in-flight frequency of the *Anopheles freeborni* used in tests. During the flutter stroke, the wingtip amplitude, at less than 1 mm, is roughly 10% of a normal stroke, but produces higher acceleration on adhered drops. For an amplitude of 0.8 mm and frequency $f = 875$ Hz, the flutter stroke generates 2500 gravities (g). Thus, this motion shown in Figure 1.3b is explicitly for removing drops, and not for flight.

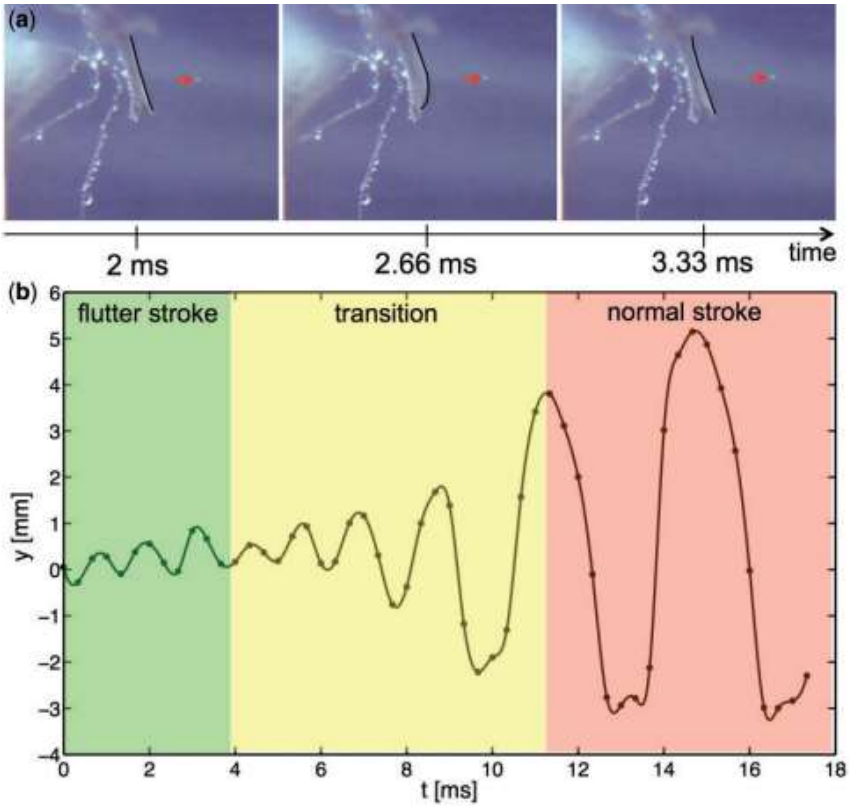

Figure 1.3: **(a)** Photographic sequence of a mosquito employing a flutter stroke to remove drops. **(b)** Time-course of the vertical position of the wingtip measured with respect to its initial state [1]

1.2.3 Drop Motion on Solid Surface

Inspired by insect wing-beat modification, we consider drop motion and release from flexible, millimetric cantilevers with a cantilever boundary condition, a simple fluid-structure system that moves in two dimensions. Motion from a forced base produces first-mode cantilever bending which, at sufficient acceleration, releases all or a portion of the fluid drop resting closer to the cantilever tip than the base. Such a simple system is of physical interest because temporal bending of a millimetric cantilever and a deforming drop are highly-coupled, complicating the predictions and conditions for drop release. Additionally, our chosen system is motivated by fluid control and the ability of surfaces to rapidly remove contaminants. It is often desirable to merge fluid drops, establish flow inside a drop, linearly displace drops, or remove drops from a surface altogether [79], all of which may be done with tuned motion of a supporting substrate.

Traditional studies of drop motion on a solid surface have been constrained to one-dimensional surface motion which deforms [80, 81, 79, 82, 83] or shatters drops [70], and those which consider sliding induced by wind shear [84, 85] or body forces [86]. Drops of radius of ∼5 mm and larger can be removed by gravity, but displacement of smaller drops in sliding or ejection type motion is difficult, particularly those smaller than the capillary length $\ell_c = \sqrt{\sigma/\rho g} = 2.7$ mm (for water), where ρ, σ, and g are fluid density, surface tension, and acceleration due to gravity respectively. For a drop to move, contact angle hysteresis must be overcome [80, 82]. This is perhaps most elegantly witnessed in sessile drops adhered to vertical surfaces. When the surface is vibrated parallel to gravity, the induced acceleration may permit the drop to remain static, fall, or climb upward [82]. Lateral vibration is diffused in the Stokes layer, but competing inertial and Laplace forces in the upper portions of the drop lead to the expression of capillary waves on the surface [81].

Drop motion control efforts have primarily aimed to displace drops linearly [87], merge multiple drops [88, 89], or establish internal flow [90]. In the simplest motions, however, complicating nonlinear drop deformation arises which is not fully understood for all substrate perturbations. Pre-

vious studies have investigated drop motion by moving contact lines [91, 92, 93, 94, 95, 96, 97] and pinch-off [98, 99] using ultrasound [79, 100] and vibration-induced motion [81, 83, 101, 85]. The transition between pinned motion and contact line movement occurs when the deviation of contact angle exceeds the contact angle hysteresis for both horizontally [102] and vertically [83] vibrated sessile drops. If contact angle hysteresis is sufficiently large, drops which are otherwise stationary on a vertical surface can be migrated against gravity with surface vibration [103]. Vertical perturbations of horizontal substrates induce axisymmetric, linear drop oscillations, and pinned contact lines at low amplitudes [83]. At high vibration amplitudes contact lines exhibit stick-slip motion and fluid oscillations are nonlinear, with nodes developing on the surface. The critical Bond number by which sliding, or contact line depinning, occurs under gravity can change with the history of inertial force [86]. At ultrasonic vibration frequencies, the drop can experience internal flow that deforms the free surface and unpins the contact line [79], or shatters the drop altogether[104, 70].

The aforementioned studies consider drop motion by one-dimensional substrate displacement. The two-dimensional drop-cantilever system studied here was first introduced to investigate the impact dynamics of drops on hydrophobic laminar leaves [105]. Environmental contaminants and seasonal changes to leaves which lower the water-repellency of foliage, increase the torque exerted to the leaf impacted by a raindrop. Inspired by insects, we study the drop-cantilever system from the opposing perspective–drop removal by the cantilever. Drop ejection from a beam occurs via three different modes: normal-to-substrate ejection, sliding, and pinch-off. Theoretical prediction of ejection modes with a given set of input variables is not a closed problem and complicated by drops' time-dependent deformation, or sloshing, which is neither periodic nor axisymmetric [60, 61, 62, 106]. Closing the problem would require solving coupled Navier-Stokes and elastica equations in time and space. At best, we can use semi-empirical relations [67] to predict the transition between complete and partial liquid removal for a fixed set of system properties. The number of system features including drop and cantilever properties, and drop location exacerbates the need for a data-driven approach. Data-driven predictive modeling of ejection modes is achievable by only a partial characterization of the ejection mode parameter space [99, 107, 108].

1.2.4 Data-Driven Predictive Model

Fluid mechanics has traditionally dealt with enormous amounts of data from experiments, field measurements, and large-scale numerical simulations. Machine learning techniques have recently received significant attention in fluid mechanics because of their ability to handle copious amounts of experimental and numerical data [109]. Big data has been a reality in fluid mechanics due to high-performance computing architectures and advances in experimental measurement capabilities [110, 111, 112]. Machine learning provides a modular and agile modeling framework that can be tailored to address many challenges in fluid mechanics, such as reduced-order modeling, experimental data processing, shape optimization [113, 114], particle image velocimetry (PIV) [115, 116, 117], turbulence closure [118, 119, 120, 121], and flow control [122, 123, 124].

It is difficult to perform parametric studies because of the vast nature of data in spatial resolution and scatteredness. The need for resource-intensive design iterations can be eliminated by modeling a data driven tool that predicts the performance of flow focusing droplet generation [125]. The relation between the satellite droplet formation and the 3D printing variables has been predicted using artificial neural networks for drop-on-demand bioprinting [126]. Wavelength analysis by the maximum entropy method can be used to predict the drop size distribution in the primary breakup of liquid jets [127]. Data-driven approaches in splash demonstration significantly improve the visual monitoring of the splash detail [128]. Ensemble learning, which combines different machine learning techniques has been successfully deployed to characterize interfacial kinetics [129] and droplet formation in ink-jet based bioprinting [3].

1.3 Thesis Outline

In this thesis we investigate the damping technique of sessile drop by absorbing portion of the kinetic energy. We explore highly-coupled fluid-solid mechanics using singular liquid drop with varying viscosityand surface tension resting on a millimetric cantilever. We also investigate Drop

ejection for drops largerthan the capillary length, can be a complicated, multi-stage event in which fluid removal occursthrough multiple mechanisms in sequence.

In Chapter 2 we begin with a description of our experimental methods. We report the experimental setup for damping by drop sloshing which is equivalent to a mass-spring-damper system and also the setup for drop ejection experiment. We also outline the video analysis and data analysis process in Chapter 2.

In Chapter 3 we describe the theoretical considerations that utilized during the model development. We report the dimensionless numbers used and energy balance equation in this chapter. We detail the elastica theory developed for calculation the inertial force of the cantilever during the drop ejection event.

In Chapter 4 we examine the damping produced by sessile drop pinned on a vibrating substrate. we consider the damping ring-down vibration of a fixed, 10-mm $\times$ 3.6-mm cantilever by a sessile drop placed at a fixed location on the dorsal surface of the cantilever. Initial tip deflection is applied so the ensuing inertial force does not overcome liquid-solid adhesion to eject the drop. Newtonian test drops vary in composition to obtain contrasting viscosity and a range of surface tension.

In Chapter 5 we use cantilever vibration to induce drop motion, and consider the physics of drop motion across a range of cantilever wetting properties, drop position, fluid properties, vibration amplitude, and vibration frequency. We describe of the drop release modes witnessed from our system and present models of acceleration for each type. A model is developed for the drop cantilever system using extended elastica theory and the shooting method which allows us to predict the onset of drop motion.

Chapter 6 extends the drop ejection analysis using a data-driven approach. We employ ensemble learning to tackle the classification problem of predicting drop ejection modes from a forced cantilever across a range of surface wettability, drop position, and drop size. Another set of base learners is used to perform regression analysis to predict the related inertial forces.

In Chapter 7, we conclude by discussing the implications of our work and suggesting directions for future research.

CHAPTER 2: METHODOLOGY

2.1 Damping by Drop Sloshing

We construct cantilevers from Kapton polymide film, elastic modulus $E = 2.5$ GPa, of length $\ell = 10$ mm (0.002 in) and width 3.60 mm (0.14 in), sourced from McMaster-Carr. Cantilevers are cut to size with a GlowForge laser cutter at sufficient power to make a cut while not charring and bevelling edges. We use three different thicknesses of Kapton which are $t_{\mathrm{h}} = 2$-mil (0.051 mm), 5-mil (0.127 mm) and 10-mil (0.254 mm) and prepare cantilevers of mass $m_{\mathrm{c}} = 2.2$ mg, 5.5 mg and 11.7 mg respectively. Cantilevers are attached to a fixed post with cyanoacrylate while a plucker produces the initial tip deflection. The plucker is a razor blade afixed to a micromanipulator. Trials in which cantilevers release from the plucker prematurely are disregarded. A schematic of our experimental setup is shown in Figure 2.1. NeverWet® hydrophobic coating is used to increase the equilibrium contact angle to $\theta_{\mathrm{c}} = 129 \pm 9.57$, N = 87. It should be noted that different liquids express different contact angles. Greater values of θ_{c} are achievable by multiple applications of NeverWet®, but superfluous hydrophobicity enables drop relocation [67, 72]. Drops of mass $m_{\mathrm{d}} = 2.0 \pm 0.1$ mg, N = 87, are placed atop the cantilever by hand using a syringe at a distance of $x_0 = 6.89 \pm 0.32$ mm, N = 87 from the fixed end. Trial-and-error ensures drop size matches the desired size, to match a desired mass, within 10%. Drop location was chosen such that drops rest near the cantilever tip without spilling over the tip when deformed. The desired drop contact radius is determined from formulas provided in the Appendix A.2.1. Liquid drop properties are augmented by mixing imitation honey (H) glycerin (G) and water (W) to various ratios by volume. With satisfactory drop size and placement, each condition has three replicates. Our naming scheme for liquid mixtures dictates the number of parts follows the liquid abbreviation. For example, 'G3W1' denotes the mixture is comprised of three parts glycerin and one part water by volume. We change the liquid surface tension by adding very small amount of dish soap to the mixture. Surface tension of the mixtures is measured with a SITA DynoTester^{+} surface tensiometer using the bubble pressure method and vi-

socity of the mixtures is measured using a Brookfield DV- II Pro Viscometer. Viscosity and surface tension our test liquids are given in Table 2.1.

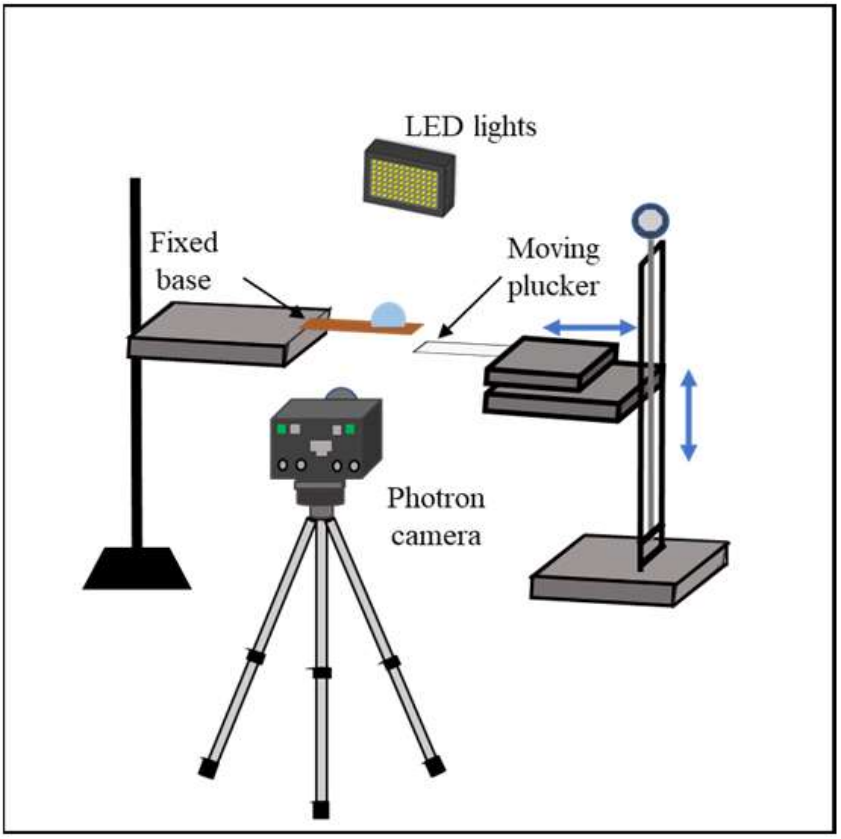

Figure 2.1: Experimental setup of vibrating cantilever using moving plucker produces the initial tip deflection.

2.2 Drop Ejection

We construct cantilevers from PTFE (Polytetrafluoroethylene) of elastic modulus $E = 480$ MPa, thickness 0.05 mm (0.002 in), and width 3.60 mm (0.14 in), sourced from McMaster-Carr. Cantilevers are cut to size with a Universal Laser Systems ILS12.150D laser cutter at sufficient power to make a cut while not charring and bevelling edges. Cantilevers are attached to the post of a K2007E01 electrodynamic shaker with cyanoacrylate adhesive. The shaker drives the cantilever base at $85-115$ Hz in linear motion parallel to gravity and is controlled by a Keysight 33210A signal

Table 2.1: Density, viscosity and surface tension of different liquid mixtures.

mixture	**symbol**	**density, ρ** [g/ml]	**viscosity, μ** [cP]	**surface tension, σ** [mN/m]	**Ohnesorge number** Oh
H1	○	1.39 ± 0.02	10,000	310**	17.06
H3G1	△	1.25 ± 0.02	3378 ± 6	100.2 ± 1.4	9.5
H1G1	▽	1.20 ± 0.01	1207 ± 5	97.4 ± 0.4	3.7
H1G3	*	1.21 ± 0.01	975.4 ± 3.3	92.6 ± 0.5	2.9
G1	◇	1.21 ± 0.01	520.7 ± 3.4	83.7 ± 1.6	1.76
G3W1	□	1.19 ± 0.02	32.8 ± 1.3	78.9 ± 1.4	0.12
G1W1	•	1.10 ± 0.01	9.26 ± 1.12	75.6 ± 0.7	0.036
G1W3	◁	1.06 ± 0.01	3.14 ± 0.35	73.2 ± 1.5	0.013
W1	▷	0.983 ± 0.004	0.981 ± 0.007	71.7 ± 0.6	0.004

**from [130]

generator for constant amplitude experiments, with impulsively started base motion. A schematic of our experimental setup is shown in Figure 2.2. We note the amplitude of the shaker post is not constant, and provide an experimentally measured amplitude curve for the shaker across the range of test frequencies, shown in Figure A.6. For experiments in which a a linearly increasing amplitude is required, we use a NI-9263 $\pm$10V 4-Channel C series module and a bus-powered, compactDAQ cDAQ-9171 USB chassis to interface with LabVIEW. NeverWet® hydrophobic coating is used to increase the range of cantilever wetting properties up to an equilibrium contact angle of $\theta_e = 155$. Greater values of θ_e are achievable by multiple applications of NeverWet®, but preclude drop placement onto the surface. We achieve lower values of θ_e by mechanically removing the coating by hand. Fluid properties are augmented by mixing glycerin and water, 1:1 by volume. The surface tension of the glycerin-water mixture is measured with a SITA DynoTester$^+$ surface tensiometer using the bubble pressure method. Drops are placed on the cantilever using a needle and syringe.

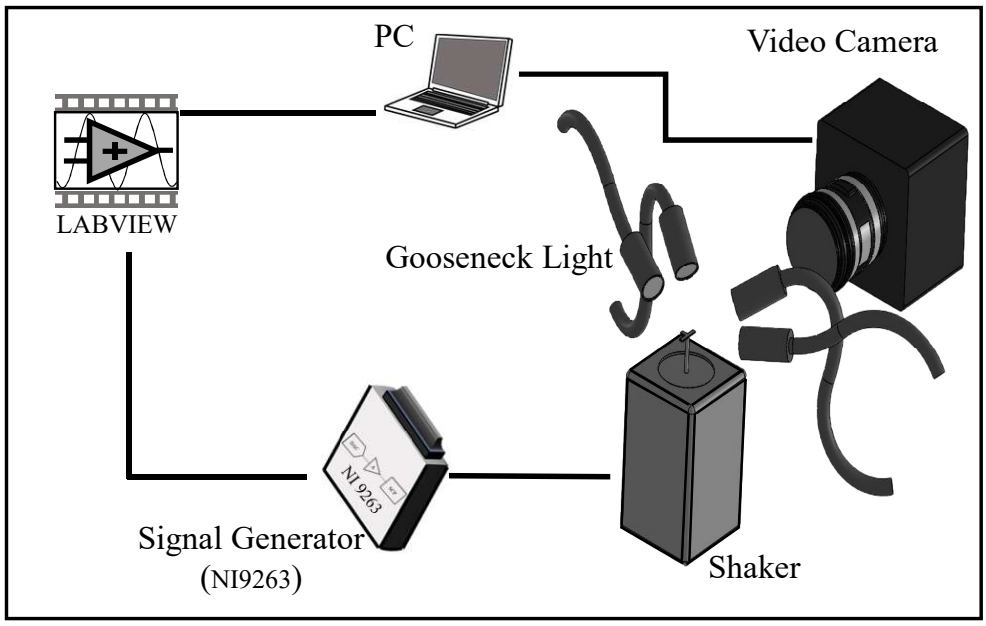

Figure 2.2: Experimental setup of drop ejection from cantilever with base motion.

2.3 Ensemble model preparation

Experimental data drop ejection experiments are fed to machine learning algorithms to build the classification and regression models. The flowchart of working principle of data driven modeling is schematized in Figure 2.3. The selection of appropriate learning algorithms is critical to the performance of any classification or regression problem [131, 132, 133]. Each ensemble learning algorithm is comprised of four base learners. For classification, the ensemble consists of random forests (RFs), gradient boosting machine (GBM), k-nearest neighbor (KNN), and support vector classification (SVC). For regression, the ensemble consists of RFs, GBM, ridge regression (RR), and support vector regression (SVR). The selection of base learners [131] is guided by data distribution. RF and GBM are advantageous when data has a high degree of nonlinearity and complex relationships between variables [134]. Small data size and small number of features motivate the use of KNN and support vector machine (SVM) [135, 136, 137]. All the physical system features influence inertial force, and the relative few we have identified motivates the use of RR, an L2 regularization [138] that ensures no elimination of features. More details about the base learners are

provided in the Appendix A.3.1.

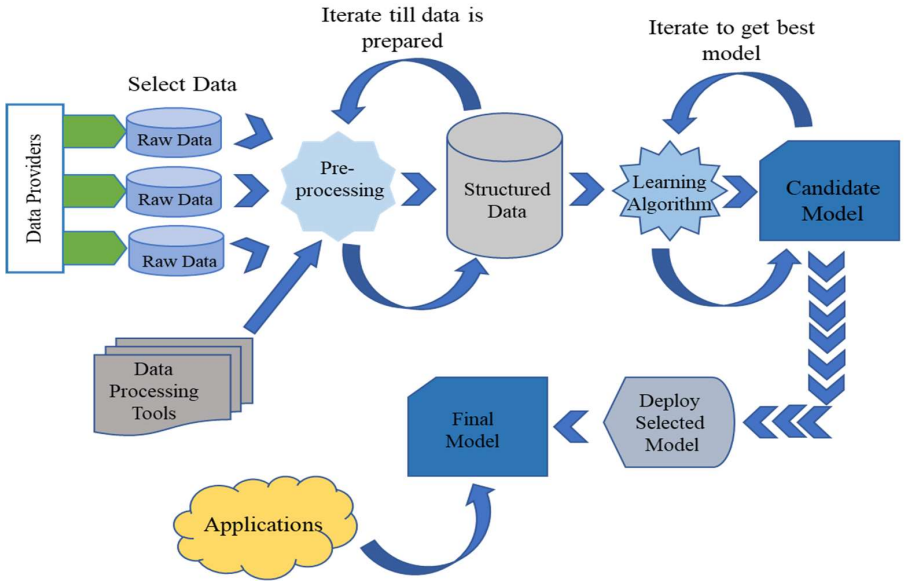

Figure 2.3: Flowchart of machine learning application for data-driven predictive modeling.

Ensemble learning is typically more effective compared to individual base learners by lowering error and cross-fitting [139] when individual base learners are selected properly [140]. To combine multiple machine learning algorithms we use bagging classification which is a combination of bootstrapping and aggregating. In bagging, base learners are selected to predict the class. For each base learner, we provide a sample dataset to all the base learners, re-sampling the training set each time for each base learner using row sampling with a replacement technique [141, 142, 143]. All the base learners are trained on a particular subset of the total dataset, the method of bootstrapping. The predictions from base learners are aggregated by obtaining a majority vote via application of a meta-classifier. A computational scheme of the bagging algorithm is shown in Figure A.8 of the Appendix. Bagging classifiers reduce overfitting compared to single independent models [141]. Sample size is also an important factor to consider in bagging, but the additional data points may not improve accuracy [144]. Our approach in bagging classification is to use small subsamples (starting with 10% of the total dataset) and obtain the accuracy from the meta-classifier. Our algorithm accepts the result from the meta-classifier if the accuracy is higher than the individual

algorithms. If the accuracy is lower than the individual model, a re-sampling process is carried out with larger subsamples.

We apply the non-negative least squares (NNLS) method to combine all the base learners to make the ensemble. NNLS was first introduced by Lawson and Hanson [145], formulated as

$$\min f(\alpha) = \frac{1}{2} \parallel G\alpha - \beta \parallel^2, \quad \text{subject to } \alpha \geqslant 0 \tag{2.1}$$

where α is a weight vector, G is the training set such that $G \in R^{m \times n}$ with m features and n number of observations, and β is the unknown sample. The weight vector is distributed among the individual learning algorithms. Predicted values Pr from each base learner are multiplied by a respective weight in the regression to predict the actual outcome. The procedure of predicting outcomes using ensemble learning is schematized in Figure A.9 of the Appendix. The final predictions from the ensemble learner are made by multiplying each base learner's prediction by its respective weight vector and summing values,

$$\text{Pr(ensemble)} = \alpha_{\text{RF}}\text{Pr(RF)} + \alpha_{\text{GBM}}\text{Pr(GBM)} + \alpha_{\text{RR}}\text{Pr(RR)} + \alpha_{\text{SVR}}\text{Pr(SVR)}. \tag{2.2}$$

2.4 Video Analysis

Drop motion events and cantilever displacement are filmed with a Photron high-speed camera at 8100-8500 fps fitted with a Nikon Sigma APO Macro 150-mm f/2.8 lens. The scene is illuminated by GS Vitec MultiLED lights. Drop measurements, location, and cantilever motion are gathered with Open Source Physics Tracker and MATLAB. A Savitzky Golay filter [146] with third order polynomial and a span of 11 is used to remove artifacts from displacement and velocity curves.

Suitable filter parameters are chosen which produces minimum deviation from the original experimental data.

CHAPTER 3: THEORETICAL CONSIDERATIONS

In this Chapter we describe the theoretical considerations that utilized during the model development. We report the calculation of specific damping capacity and other dimensionless numbers utilized to examine the damping by drop sloshing event in §3.1. Furthermore, we report the energy balance of the sloshing liquid to determine the energy dissipation due to viscosity in §3.1. We detail the elastica theory developed for calculation the inertial force of the cantilever during the drop ejection event in §3.3. We modify and computationally solve Hamilton's equations to determine the inertial force acting on the droplet for any beam shape. Which we do computationally using an assumed-modes method with von Karman strains to capture the large beam deformation.

3.1 Quantifying damping capacity

Generally, damped systems in free vibration with unchanging mass can be described by a familiar equation of motion,

$$m\ddot{y} + c\dot{y} + ky = 0. \tag{3.1}$$

In our system, y is vertical tip displacement, mass $m = m_c + m_d$ and is nonuniformly distributed along the cantilever, the damping coefficient c is not constant, and the spring constant k is dependent on cantilever material and thickness. The nonlinear behavior of damping, exacerbated by drop deformation across vibration cycles, is dependent on vibration amplitude and necessitates the use of a simple analytical tool. We thus employ the specific damping capacity ψ, defined as

$$\psi = \frac{\Delta T}{T} \tag{3.2}$$

where ΔT is the kinetic energy converted into heat or potential energy during one cycle and

$$T = V^2 \left[\frac{m_c}{6} + \frac{m_d}{2} \left(\frac{x_0}{\ell} \right)^2 \right] \tag{3.3}$$

is the maximum kinetic energy of the cantilever during the cycle and V is the velocity of the cantilever tip. The energy dissipated during the ith cycle can be expressed as,

$$\Delta T_i = T_i - T_{i+1} = (V_i^2 - V_{i+1}^2) \left[\frac{m_c}{6} + \frac{m_d}{2} \left(\frac{x_0}{\ell} \right)^2 \right], \tag{3.4}$$

where specific damping capacity during the ith cycle is expressed as

$$\psi_i = \frac{V_i^2 - V_{i+1}^2}{V_i^2} \tag{3.5}$$

with V measured at $y = 0$. In order to compare the response of cantilevers of varying stiffness we introduce another dimensionless parameter, effective acceleration[40] Γ, as

$$\Gamma = \frac{A\omega^2}{g}, \tag{3.6}$$

where A, ω, and g are the amplitude, vibration frequency of the cantilever motion and gravitational acceleration respectively.

3.2 Energy dissipation due to viscosity

We employ an energy balance [147, 21] on the cantilever at time $t = 0$ and after the end of the first cycle ($'$) to provide an additional method viscous dissipation quantification due to drop sloshing E_μ,

$$E_\mu = \Delta E_p + \Delta E_s - E_d, \tag{3.7}$$

where E_{d} is the energy dissipated via aerodynamic and internal damping measured by using a solid mass which cannot deform. The change in the cantilever's potential bending energy is

$$\Delta E_{\mathrm{p}} = \frac{3EI}{2\ell^3}\left(y^2 - y'^2\right). \tag{3.8}$$

The deflection of the cantilever at release y is greater than the deflection after one cycle, y'. A change in the surface energy of the liquid drop can be measured by considering the change in liquid-gas interface area and liquid-solid contact area,

$$\Delta E_{\mathrm{s}} = \sigma\left(A_{\mathrm{s}} - A'_{\mathrm{s}}\right) + \pi\sigma\left({r_{\mathrm{c}}}^2\cos\theta_{\mathrm{c}} - {r'_{\mathrm{c}}}^2\cos\theta'_{\mathrm{c}}\right), \tag{3.9}$$

where A_{s} and A'_{s}, r_{c} and r'_{c}, θ_{c} and θ'_{c} are the surface areas, contact radii and contact angles of the liquid at $t = 0$ and after one cycle, respectively. Gravitation potential energy $\Delta E_{\mathrm{g}} = m_{\mathrm{c}}g(y_{\mathrm{c}} - y'_{\mathrm{c}}) + m_{\mathrm{d}}g\left(y_{\mathrm{d}} - y'_{\mathrm{d}}\right)$, where y_c and y_{d} are the vertical positions of the cantilever's center of mass and beam surface beneath the drop, respectively, is omitted from Eq.(3.7) because we find ΔE_{g} to be one to three orders of magnitude less than the other energies of Eq.(3.7).

3.3 Determining inertial forces from modal shape

The traditional approach to beam structural dynamics theory involves the Euler-Bernoulli kinematic assumption with small deflections and provides a straightforward path from a statement of equilibrium to the equation of motion. However, the large deflections observed motivate the use of Euler's elastica to model the beam deformation. In addition, the presence of fluid drops atop the beams imposes added forcing/inertial terms. Using representative static solutions of the elastica as a nonlinear basis for the large deflections, a reduced-order energy-based model admits a path to predict the beam structural dynamics through an assumed-modes model. Finally, we can use the elastica kinematics to transform the beam's structural dynamics to the drop's motion and thus associated inertial forces.

3.3.1 Elastica development

A beam's bending moment M is proportional to the change in the curvature produced by the action of the load Figure 3.1. This law may be written mathematically as follows:

$$\frac{1}{r} = -\frac{d\theta}{dz} = -\frac{M}{EI} \tag{3.10}$$

where r is the radius of curvature, θ is the slope at any point x_o, where x_o is measured along the arc length of the member as shown in Figure 3.1, E is the modulus of elasticity, and I is the cross-sectional moment of inertia.

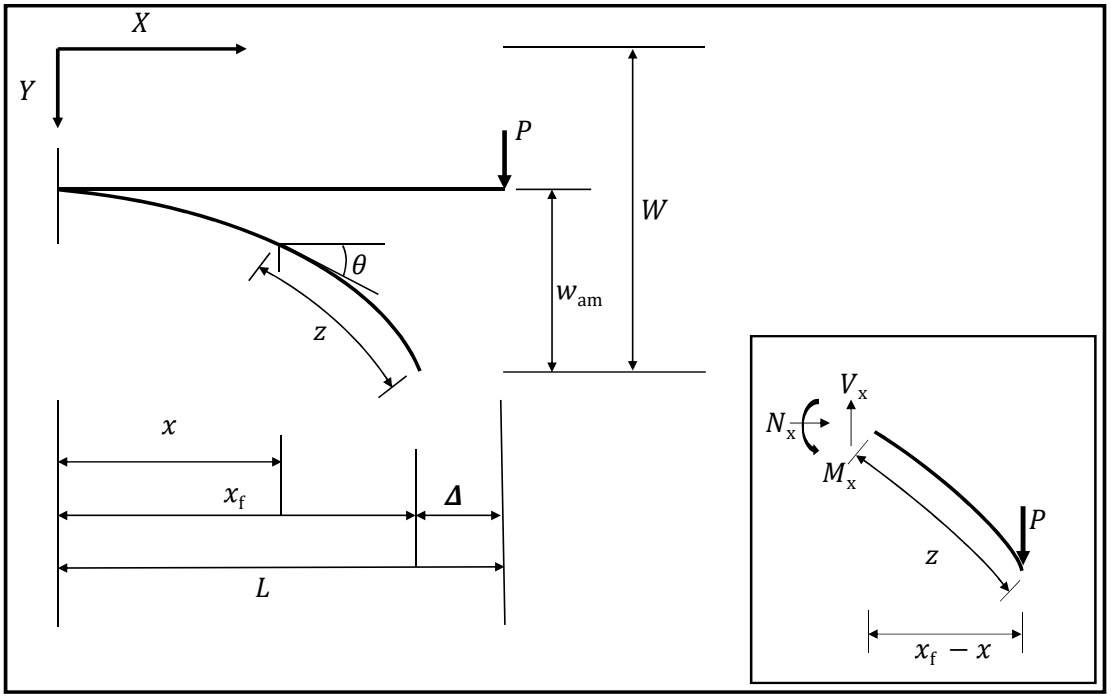

Figure 3.1: Large deformation of a cantilever beam of uniform cross section. Inset: Free-body diagram of a beam element of arbitrary length.

Looking ahead, we represent the beam's transverse deflection as a representative static shape $w_{\text{am}}(x)$. In Cartesian coordinates, Eq.(3.10) may then be written as

$$\frac{1}{r} = \frac{w''_{\text{am}}}{[1+(w'_{\text{am}})^2]^{\frac{3}{2}}} = -\frac{M}{EI} \tag{3.11}$$

where

$$w'_{\text{am}} = \frac{dw_{\text{am}}}{dx} \qquad \text{and} \qquad w''_{\text{am}} = \frac{d^2 w_{\text{am}}}{dx^2}. \tag{3.12}$$

The expression for the bending moment M at any $0 \leq x \leq x_{\text{f}}$, where x_{f} tip-to-base distance for a curved beam of length L, may be obtained by using the free-body diagram in Figure 3.1. Applying statics,

$$M = -P(x_{\text{f}} - x). \tag{3.13}$$

By substituting Eq.(3.13) into Eq.(3.11) and assuming that the flexural rigidity EI is uniform along the beam length, we obtain

$$\frac{w''_{\text{am}}}{[1 + (w'_{\text{am}})^2]^{\frac{3}{2}}} = \frac{P(x_{\text{f}} - x)}{EI} \equiv \lambda(x). \tag{3.14}$$

Integrating Eq.(3.14), we obtain

$$\frac{w'_{\text{am}}}{[1 + (w'_{\text{am}})^2]^{\frac{1}{2}}} = \varphi(x) + C, \tag{3.15}$$

where

$$\varphi(x) = \int \lambda(x) dx = \frac{P}{EI}(x_{\text{f}} x - \frac{1}{2} x^2) \tag{3.16}$$

and C is the constant of integration that can be determined by applying a boundary condition. In this case the beam has zero slope at the root, or $w'_{\text{am}}(0) = 0$. By using this boundary condition in Eq.(3.15), we find

$$\frac{w'_{\text{am}}}{[1 + (w'_{\text{am}})^2]^{\frac{1}{2}}} = \frac{P}{EI}(x_{\text{f}} x - \frac{1}{2} x^2) \equiv G(x). \tag{3.17}$$

Solving Eq.(3.17) for w'_{am}, we obtain

$$w_{\text{am}}{}'(x) = \frac{G(x)}{[1 - G(x)^2]^{\frac{1}{2}}}. \tag{3.18}$$

It should be noted, however, that $G(x)$ in Eq.(3.17) is a function of the unknown horizontal dis-

placement $\Delta = L - x_f$ of the free end of the beam. The value of Δ may be determined from the equation

$$L = \int_0^{x_f} [1 + (w'_{am})^2]^{\frac{1}{2}} dx \tag{3.19}$$

by using a shooting method. That is, we assume a value of Δ (and thus x_f, the upper limit of integration) and carry out the integration in Eq.(3.19). If our guess of Δ is correct, the integral will indeed yield the beam length L. If the integral is too large, our calculated beam length is too long and we need to use a smaller Δ; if the integral is too small, a larger Δ. The procedure may be repeated for various values of Δ until the correct length L is obtained; numerical methods exist to carry out this procedure rapidly and to ensure convergence to the actual beam length.

Building on this method, we then use the results of Eq.(3.19) to find the corresponding assumed horizontal deformation of the beam, which we describe as the deflection in the negative x-direction u_{am}. Moreover, we can apply the method for any given point on the beam, not merely for the full length. In so doing, we establish a numerical assumed shape for the horizontal deformation. With u_{am} found, w_{am} can be found using Eq.(3.14). Eq.(3.14) is a nonlinear second order differential equation and exact solution of this equation is not presently available [148]. Instead we use a Taylor series expansion taking only the first two terms of the series and then converge it with the original equation. Convergence of these two equations shows that the difference is on the order of $O(-15)$.

3.3.2 Reduced-order energy-based model development

Using an assumed-modes construction, we represent the beam displacement in terms of the representative deflection shape $w_{am}(x)$ (i.e., the assumed mode derived above) and a rigid-body displacement mode $w_0(x)$. While this approach admits the inclusion of additional assumed modes, we found a single-mode approximation adequately predicts the beam dynamics. The total beam

transverse displacement is then

$$w(x,t) = a_0(t)w_0(x) + a(t)w_{\text{am}}(x), \tag{3.20}$$

where $a(t)$ represents the amplitude of the assumed mode motion and $a_0(t)$ corresponds to the vertical motion of the shaker (i.e., the beam root). The total beam axial displacement

$$u(x,t) = a_0(t)u_0(x) + a(t)u_{\text{am}}(x). \tag{3.21}$$

The experiments involve base excitation of the beams, so we use $w_0(x) = 1$. Base motion is strictly transverse to the beam, so the horizontal component $u_0(x) = 0$.

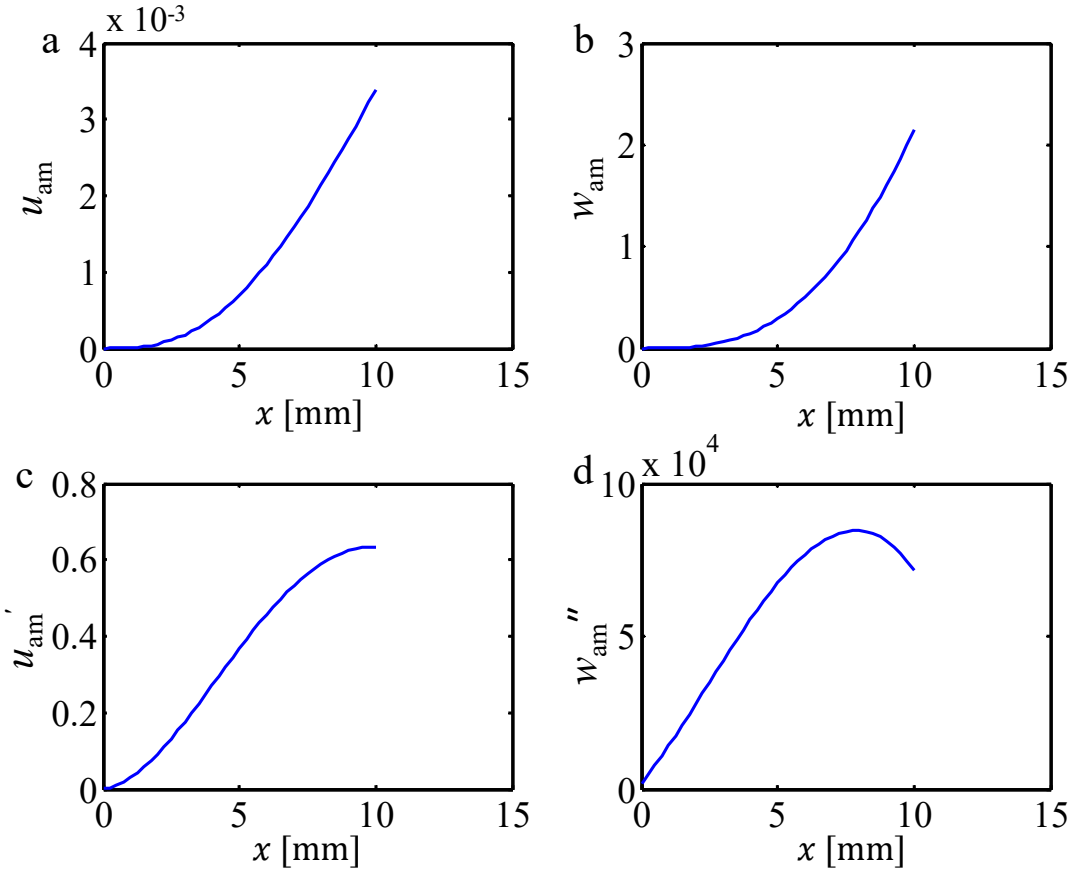

Figure 3.2: Assumed beam deflection shapes in the (a) axial and (b) transverse directions for all points along the beam length, with (c) and (d) spatial derivatives used in strain energy formulation.

Formulating the equations of motion involves application of the extended Hamilton's Principle, which involves computations of the kinetic energy, strain energy, and virtual work associated with a virtual displacement within a particular assumed mode [149]. The kinetic energy of the beam is

$$T = \frac{1}{2}\int_0^L \rho A \left(\dot{u}(x,t)^2 + \dot{w}(x,t)^2\right) dx. \tag{3.22}$$

Substituting the assumed-modes representations of 59w,59u and recognizing that $a(t)$ and $a_0(t)$ can be pulled outside the spatial integrals:

$$T = \frac{1}{2}\left[\dot{a}^2\left(\int_0^L \rho A u_{\text{am}}^2 dx + \int_0^L \rho A w_{\text{am}}^2 dx\right) + \dot{a}_0^2 \int_0^L \rho A w_0^2 dx + 2\dot{a}_0\dot{a}\int_0^L \rho A w_0 w_{\text{am}} dx\right]. \tag{3.23}$$

Note this has a quadratic form

$$T = \frac{1}{2}\begin{Bmatrix} \dot{a}_0 \\ \dot{a} \end{Bmatrix}^t \begin{bmatrix} M_{00} & M_0 \\ M_0^t & M \end{bmatrix} \begin{Bmatrix} \dot{a}_0 \\ \dot{a} \end{Bmatrix}, \tag{3.24}$$

where

$$M = \int_0^L \rho A u_{\text{am}}^2 dx + \int_0^L \rho A w_{\text{am}}^2 dx \qquad \text{and} \qquad M_0 = \int_0^L \rho A w_0 . w_{\text{am}} dx. \tag{3.25}$$

The strain energy of the beam, including non-linear strain-displacement relations to account for the large displacements and rotations, is

$$U = \frac{1}{2}\int_0^L \left[(EIw''(x))^2 + \frac{1}{2}(EIw'(x,t))^2(w''(x))^2 + \frac{1}{320}Ebh^5(w''(x,t))^4\right] dx, \tag{3.26}$$

where b is beam with and h is beam thickness. Since the base motion is a rigid-body motion, the spatial derivatives $w_0' = w_0'' = \cdots = 0$ and we only have derivatives of the assumed modes. As with the kinetic energy, the time component $a(t)$ can be pulled outside the integral and for a single-term

approximation:

$$U = \frac{1}{2}a^2 \int_0^L EI(w''_{\text{am}})^2 dx + \frac{1}{4}a^4 \int_0^L EI(w'_{\text{am}})^2 (w''_{\text{am}})^2 dx + \frac{1}{640}a^4 \int_0^L Ebh^5 (w''_{\text{am}})^4 dx. \quad (3.27)$$

In computing these derivatives, we use a finite-difference method; the derivatives of u'_{am} and w''_{am} are shown in Figure 3.2 to confirm smoothness. One term of this expression has a quadratic form, which leads to

$$U = \frac{1}{2}\begin{Bmatrix} a_0 \\ a \end{Bmatrix}^t \begin{bmatrix} 0 & 0 \\ 0 & k_{\text{L}} \end{bmatrix} \begin{Bmatrix} a_0 \\ a \end{Bmatrix} + \frac{1}{4}\begin{Bmatrix} a_0 \\ a \end{Bmatrix}^t \begin{bmatrix} 0 & 0 \\ 0 & k_{\text{NL}} \end{bmatrix} \begin{Bmatrix} a_0^3 \\ a^3 \end{Bmatrix}. \quad (3.28)$$

Eq.(3.27) can be divided into two parts: the usual linear stiffness from Euler-Bernoulli beam theory (quadratic energy term) and the nonlinear stiffness terms:

$$k_{\text{L}} = \int_0^L EI {w''_{\text{am}}}^2 dx, \quad (3.29)$$

and from Von Karman strain the non-linear term is:

$$k_{\text{NL}} = \int_0^L \left[EI {w'_{\text{am}}}^2 {w''_{\text{am}}}^2 + \frac{1}{160} Ebh^5 {w''_{\text{am}}}^4 \right] dx. \quad (3.30)$$

Finally, the beam is driven via harmonic base motion, $f_{\text{base}}(t)$. Since it is applied only at the root of the beam, the virtual work associated with this forcing is

$$\delta W = f_{\text{base}}(t)\delta w(0,t) = f_{\text{base}}(t)\delta a_0(t) w_0(0) + f_{\text{base}}(t)\delta a(t) w(0) = \delta a_0(t) f_{\text{base}}(t). \quad (3.31)$$

Application of extended Hamilton's Principle then leads to a set of equations of motion:

$$\begin{bmatrix} M_{00} & M_0 \\ M_0^t & M \end{bmatrix} \begin{Bmatrix} \ddot{a}_0 \\ \ddot{a} \end{Bmatrix} + \begin{bmatrix} 0 & 0 \\ 0 & k_{\text{L}} \end{bmatrix} \begin{Bmatrix} a_0 \\ a \end{Bmatrix} + \begin{Bmatrix} 0 \\ k_{\text{NL}} a^3 \end{Bmatrix} = \begin{Bmatrix} f_{\text{base}} \\ 0 \end{Bmatrix} \quad (3.32)$$

The experiments involve base motion that consists of a fixed-frequency oscillation with linearly increasing amplitude; that is,

$$a_0(t) = (A_\mathrm{i} + A_\mathrm{rate} t) \sin \Omega t, \tag{3.33}$$

where A_i is the initial base amplitude and A_rate is the rate at which the base amplitude increases. With the addition of a viscous damping term for the beam, the second equation of Eq.(3.32) becomes

$$M\ddot{a} + c\dot{a} + k_\mathrm{L} a + k_\mathrm{NL} a^3 = -M_0 \ddot{a}_0(t) \tag{3.34}$$

Solving Eq.(3.34) yields $a(t)$ and substituting back in Eq.(3.20), Eq.(3.21), Eq.(3.33) provides the beam axial and transverse displacement:

$$u(x,t) = a(t) u_\mathrm{am}(x) \tag{3.35}$$

and

$$w(x,t) = a(t) w_\mathrm{am}(x) + (A_\mathrm{i} + A_\mathrm{rate} t) \sin(\Omega t). \tag{3.36}$$

3.3.3 Kinematics and drop motion

With the beam motion determined, we can compute the drop motion and its associated inertial forces. Here, x_0 is the position of the drop when the beam is stationary, which is labeled in **Fig.4** of the main text. Using Eq.(3.35) the horizontal displacement of the point where the drop contacts the beam becomes:

$$x_\mathrm{d}(t) = x_0 - a(t) u_\mathrm{am}(x_0) \tag{3.37}$$

The vertical displacement of the point where the drop contacts the beam is simply the displacement at that point, $y_\mathrm{d}(t) = w(x_0, t)$. From Eq.(3.36), and Eq.(3.37), the position vector $\mathbf{r}(t)$ of the point

mass is:

$$\mathbf{r}(t) = \left[x_{\mathrm{d}} - \delta \sin w'(x_0, t)\right] \hat{\imath} + \left[y_{\mathrm{d}} + \delta \cos w'(x_0, t)\right] \hat{\jmath} \tag{3.38}$$

$$= \left[x_0 - a u_{\mathrm{am}} - \delta \sin w'(x_0, t)\right] \hat{\imath} + \left[a w_{\mathrm{am}} + (A_{\mathrm{i}} + A_{\mathrm{rate}} t) \sin(\Omega t) + \delta \cos w'(x_0, t)\right] \hat{\jmath}. \tag{3.39}$$

Finally, the inertial force acting on a rigid drop's center of mass (COM) is

$$F_i = m_{\mathrm{d}} \ddot{\mathbf{r}}. \tag{3.40}$$

Using Eq.(3.40), we calculate the inertial force produced by the cantilever at any position of the drop at any time. Inertial forces are compared the adhesion force to find the force balance and determine the ejection modes.

CHAPTER 4: SESSILE LIQUID DROPS DAMP FREELY VIBRATING SUBSTRATES

In this chapter, we consider the damping of a fixed, 10-mm $\times$ 3.6-mm cantilever by a sessile drop placed at a fixed location on the dorsal surface of the cantilever. Initial tip deflection is applied so the ensuing inertial force does not overcome liquid-solid adhesion to eject the drop. Newtonian test drops vary in composition to obtain contrasting viscosity and a range of surface tension. We present the effect of surface tension on damping in §4.1 and the effect of viscosity on damping in §4.2. We present the relation of damping with the vibration frequency in §4.3 A discussion of results follows in §4.4.

4.1 Effect of surface tension on damping

We first examine the influence of sloshing liquid surface tension σ on the specific damping capacity ψ by fixing drop viscosity and using G3W1 modified with surfactant. The severity of surface tension on changes ψ is highly dependent on cantilever flexibility. For our stiffest cantilever, with thickness 10-mil, there is no discernible influence on ψ to changes in surface tension across the cantilever's range of effective acceleration Γ as shown in Figure 4.1a. As expected, lower surface tension values promote greater drop deformation as seen by the image sequences in Figure 4.1c-d. We quantify the degree to which a drop deforms from its static state by measuring the flatness factor [71]

$$\delta^* = \frac{h}{d}\frac{d_0}{h_0}, \tag{4.1}$$

where h is the distance from the drop peak to substrate and d is the diameter of the drop contact patch. The static system expresses h_0 and d_0 dimensions, which are labeled graphically in Fig-

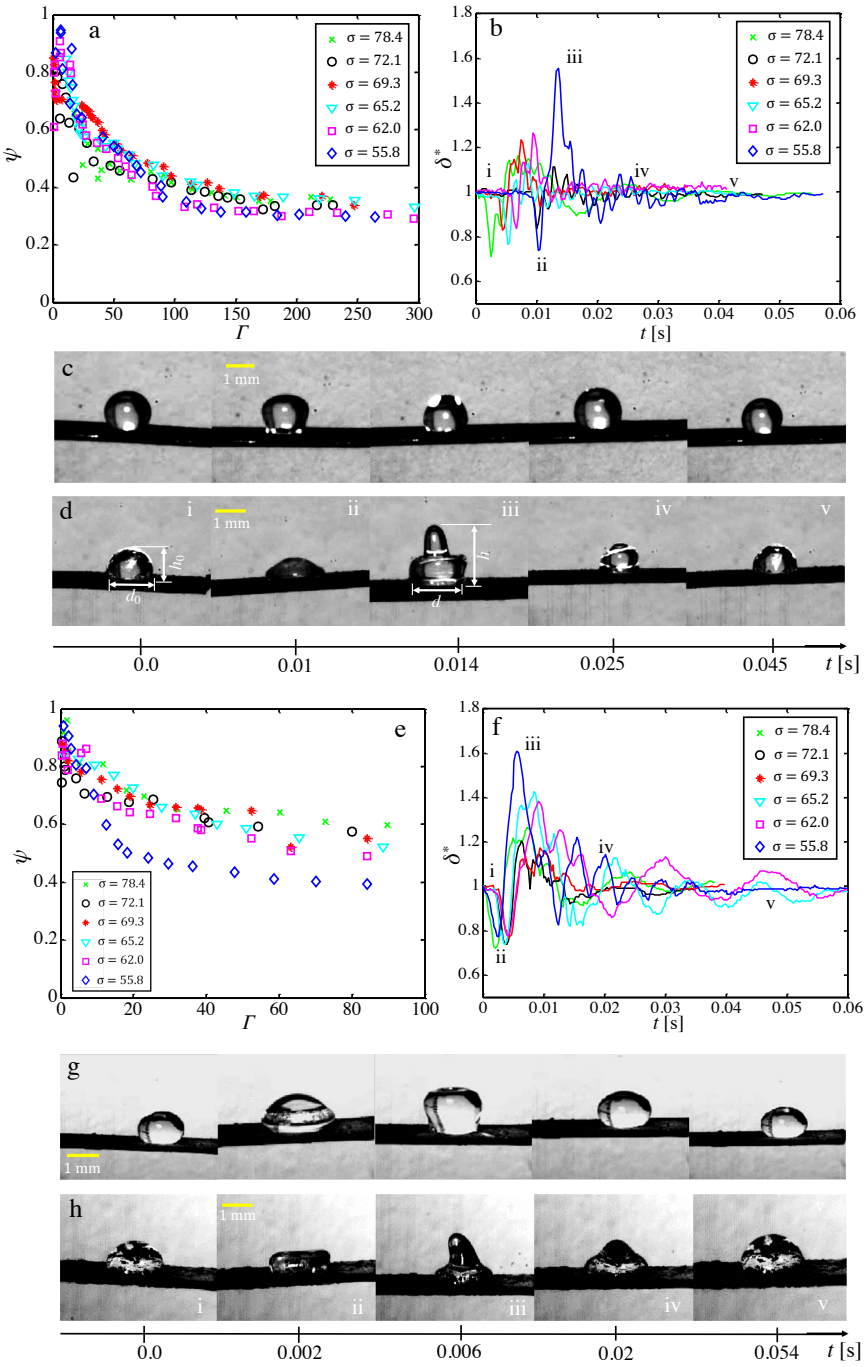

Figure 4.1: The effect of surface tension on damping. **(a & e)** Specific damping capacity ψ versus effective acceleration Γ. **(b & f)** Temporal variation of flatness factor. **(c, d, g, & h)** Photo sequences of drop sloshing for a G3W1 drop with surface tension value $\sigma = 78.4$ mN/m and $\sigma = 55.8$ mN/m respectively. Panels (a-d) correspond to a 10-mil thick cantilever and panels (e-f) to a 5-mil cantilever. Values in the plots legends have units mN/m.

ure 4.1d. Moving contact lines ensure the drop contact patch oscillates in time. We plot δ^* versus time t in Figure 4.1b for all tested G3W1 drops, with a value measured every video frame. The curves of Figure 4.1b stand testament to the chaotic nature of drop deformation whilst sloshing on an elastic substrate. A fast Fourier transform (FFT) for flatness factor is provided in Figure A.1 of the Appendix A.1.2. The repeatability of ψ values across multiple trials is shown by plotting ψ versus γ for multiple replicates in Figure A.2. We find replicate curves indistinguishable from one another for three representative surface tension values.

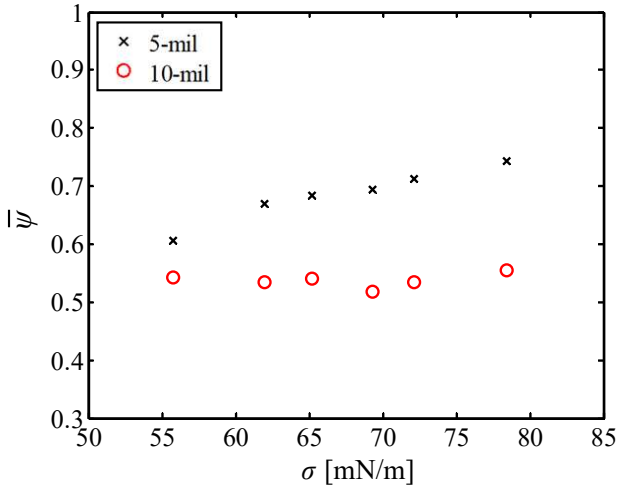

Figure 4.2: Average damping capacity $\bar{\psi}$ versus G3W1 drop surface tension σ.

In contrast to a 10-mil cantilever, damping of the 5-mil cantilever by the liquid drop is generally enhanced by increasing surface tension in our range of experimental values as shown in Figure 4.1e. We visualize how σ affects damping by averaging the ψ values in Figure 4.1a to produce $\bar{\psi}$. We plot $\bar{\psi}$ versus σ in Figure 4.2 for both 10-mil and 5-mil cantilevers. One might expect that greater drop deformation (Figure 4.1f) ensures greater damping, but it should be noted that while lower surface tension drops are more easily deformed, they require less energy to do so; surface energy scales with surface tension [21, 150]. Furthermore, greater surface tension values dictate that a greater volume of the static drop participates in deformation. In other words, greater surface tension allows the center of liquid mass to move further from the substrate as contact lines recede. The result is that internal energy dissipation by viscosity occurs within a larger fluid volume. A visual

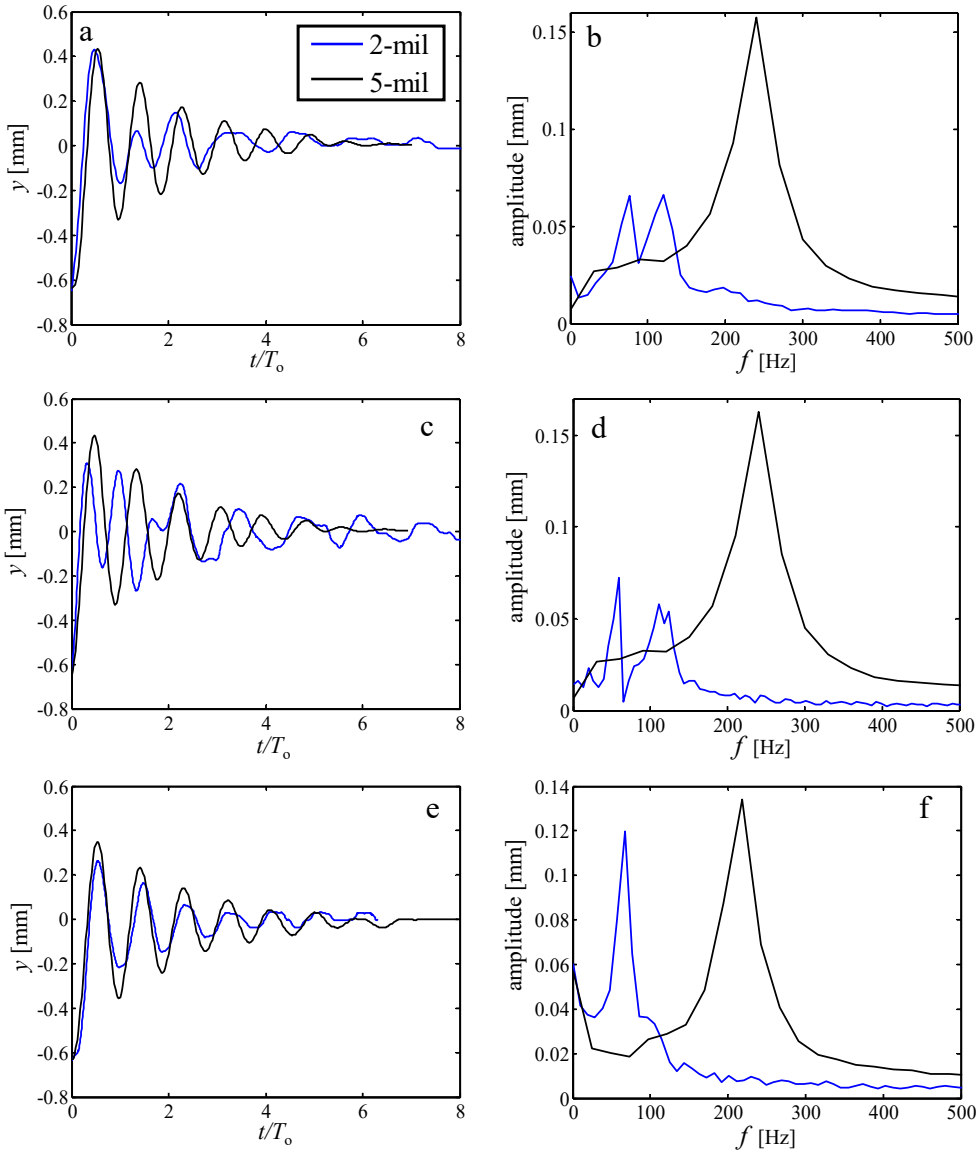

Figure 4.3: Time response **(a,c,e)** and frequency response **(b,d,f)** with G3W1 drop ($\mu = 32.8$ cP) with surface tension $\sigma = 78.4$ mN/m (a,b), $\sigma = 69.3$ mN/m (c,d) and $\sigma = 55.8$ mN/m (e,f).

accompaniment of this argument is provided images comparing the centroid of two G3W1 drops of different surface tension at their maximum δ^* in Figure A.3. The portion of the liquid drop pulled away from the substrate is greater for the higher surface tension liquid. Surface tension thus affects the mechanical impedance matching and force transmitted between the drop and cantilever. A quantitative description of internal dissipation for contrasting drop deformations is likely only feasible through simulation, and outside the scope of this study. We discuss damping effects by

drops of different viscosity in §4.2.

The flexibility and diminutive inertia of the 2-mil cantilever permit the expression of higher-order behavior, which is surface tension dependent. We illustrate such behavior by the vibration curve in Figure 4.3a. Using a drop with $\sigma = 0.0784$ N/m, we witness the sloshing drop can both amplify and suppress cantilever tip amplitude. When sloshing drops achieve a high δ^* value when the tip is at a local minima, the drop suppresses the magnitude of the minima, as seen in the first trough of Figure 4.3a. A drop achieving a low δ^* value near a local tip minima enhances the downward tip motion, as seen by the second trough of Figure 4.3a. We also find that the liquid drop is able to store elastic energy in its surface out-of-phase with cantilever motion, reducing the cantilever displacement to nearly zero for half a period (Figure 4.3a). A FFT of the vibration curve shown in Figure 4.3a reveals two dominant vibration frequencies Figure 4.3b. Such higher-order behavior prevents the quantification of damping with Eq.(3.5) across the time of vibration. Reducing the surface tension of the drop reduces higher-order behavior but still reveals wave clipping at lower amplitudes. The cause for the shift in behavior with surface tension is unknown.

4.2 Effect of viscosity on damping

In the previous section, we posit that surface tension modulates the volume of the drop participating in viscous damping. Viscosity, detached from surface tension, also governs deformation and energy dissipation. In this section, we compare the damping capacity of drops with a range of viscosity in order to identify an approximate optimum value. Neither an inviscid fluid or a fluid of infinite viscosity, a solid, can damp vibration by viscosity and thus some system-dependent intermediate value provides the greatest damping. The salient properties of test fluids is tabulated in Table 2.1. Video compilations of each cantilever topped with each test liquid are available in Appendix A.1.1. We choose test fluids in which we see a maximum damping capacity appear for neither the lowest or highest viscosity, and covering $0.89 - 10^3$ cP.

We plot specific damping capacity ψ versus effective acceleration Γ in Figure 4.4a-c. As with surface tension, ψ is cantilever dependent. The stiffest 10-mil cantilever is damped most effectively by H1G3 (975 cP), as shown in Figure 4.4a (Movie S1). The intermediate 5-mil cantilever is damped best by the less viscous G3W1 (33 cP), as shown in Figure 4.4b (Movie S2). The thinnest 2-mil cantilever is damped best by the H1G3, as shown in Figure 4.4c (Movie S3), but we were unable to measure ψ across the entire vibration curve for G3W1, G1W1, G1W3, and W1 due to the higher-order behavior discussed above (§4.1, Figure 4.3). Temporal displacement curves for G1W3 and W1 are given in Figure A.4 of the Appendix. For all three cantilevers, the most viscous liquid, H, has a similar specific damping curve to the solid mass as shown in Figure 4.4a-c.

We acknowledge we cannot completely decouple changes in surface tension amongst the test fluids in Table 2.1 from variation in viscosity. Unification of viscosity and surface tension into a single dimensionless group can be done with the Ohnesorge number, $\mathrm{Oh} = \mu(\rho\sigma R)^{-1/2}$, where R is the static drop radius and μ is viscosity. It is noteworthy an increase in viscosity of 1000× is accompanied by an increase in surface tension of 1.37×, so Oh values in our tests are driven primarily by changing viscosity. For the first vibration cycle, corresponding to the rightmost points in Figure 4.4a-c, we plot ψ versus Oh in Figure 4.5. For all cantilevers, we witness a rise in ψ from the lowest values of Oh, and a fall in ψ after $\mathrm{Oh} \approx 2.5$. While Figure 4.5 does not reveal the critical Oh value that maximizes damping, we infer it lies in the range of $1-5$ for all cantilevers. The temporal plots of δ^* in Figure 4.4d-e reveal the nature of drop deformation across viscosity, namely that the two least viscous fluids undergo significant deformation compared to the rest. Thus, a trade-off between deformation and the ability of viscosity to dissipate emerges from Figure 4.5, with the composition of this trade-off driven by cantilever dynamics. The relation between drop deformation, quantified with flatness factor δ^*, and viscosity is shown in Figure 4.6. The heatmap of Figure 4.6 reveals that intermediate levels of δ^* correspond to the greatest damping.

By calculating the energy lost to viscosity and contact line friction during the first vibration cycle we can generate an alternative means to find the 'sweet spot' in Oh with our cantilevers. Solving

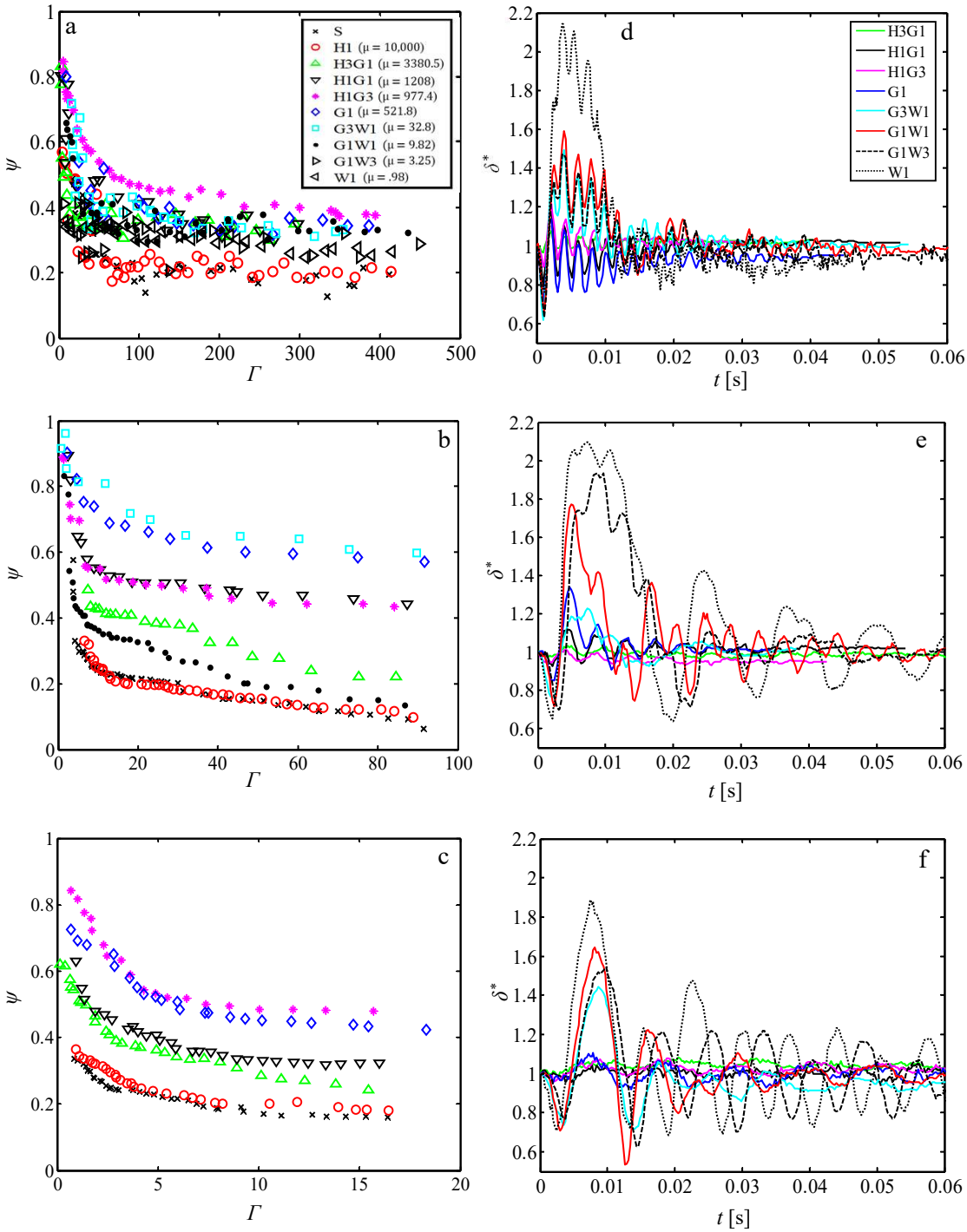

Figure 4.4: Damping changes with viscosity. **(a-c)** Specific damping capacity ψ versus effective acceleration Γ. **(d-f)** Temporal variation of flatness factor. Each row represents a different cantilever: 10-mil (a & d), 5-mil (b & e) and 2-mil (c & f). The legend in panel (a) applies to panels (a-c); viscosity values have units of cP. The legend in panel (d) applies to panels (d-f).

balance with PE,SE accounts for changes in cantilever potential bending energy (ΔE_p), the energy stored in the drop surface (ΔE_s), and a lumped energy dissipation present without drops (E_d). We plot E_μ normalized by the initial potential bending energy of a static cantilever $E_0 = 3EIy^2/2\ell^3$ in Figure 4.6d-f. Peak viscous dissipation occurs at Oh $\approx 1-2.5$ for all cantilevers, also aligning with the greatest ψ values as expected.

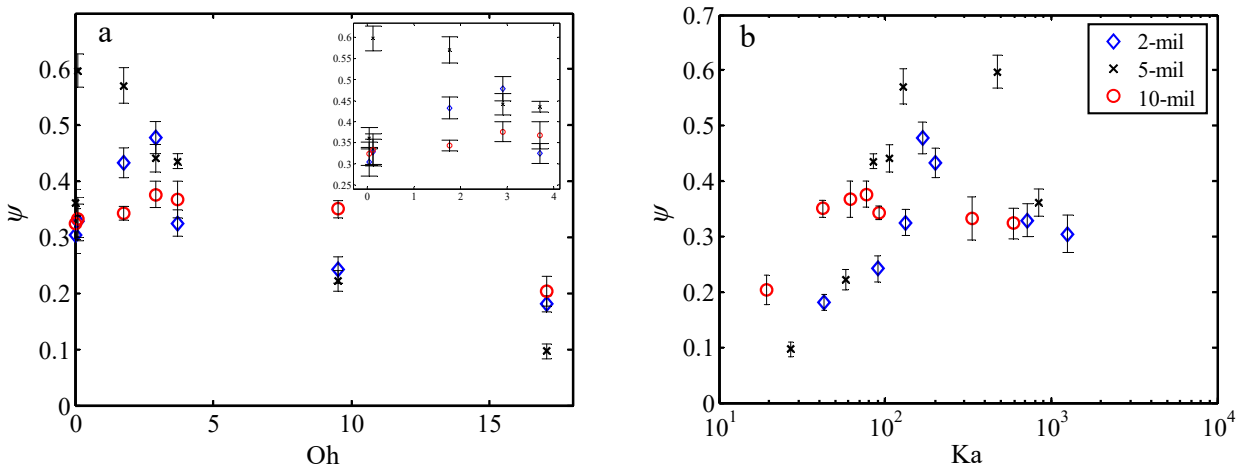

Figure 4.5: Combined influence of viscosity and surface tension on damping. Specific damping capacity ψ versus Ohnesorge number **(a)** and Kauffman number **(b)**. Error bars represent standard deviation in damping capacity.

4.3 Evaluating the frequency domain

A presentation of vibratory behavior modulation by drops would be incomplete without examining how drop properties influence frequency. As expected, stiffer cantilevers naturally vibrate at a higher frequency. We examine the effect of fluid viscosity on frequency modulation by nondimensionalizing damped natural frequency f by that measured for cantilevers with solid masses. This metric $f^*>1$ for all experimental liquids is shown in Figure 4.7b. As viscosity rises and liquids behave more solid-like, $f^* \to 1$. We rationalize that decreasing viscosity allows for a virtual disconnection between the cantilever and drop's center of mass, much like relaxing a spring. Thus, from the viewpoint of frequency, low viscosity effectively reduces a drop's inertia. While viscosity

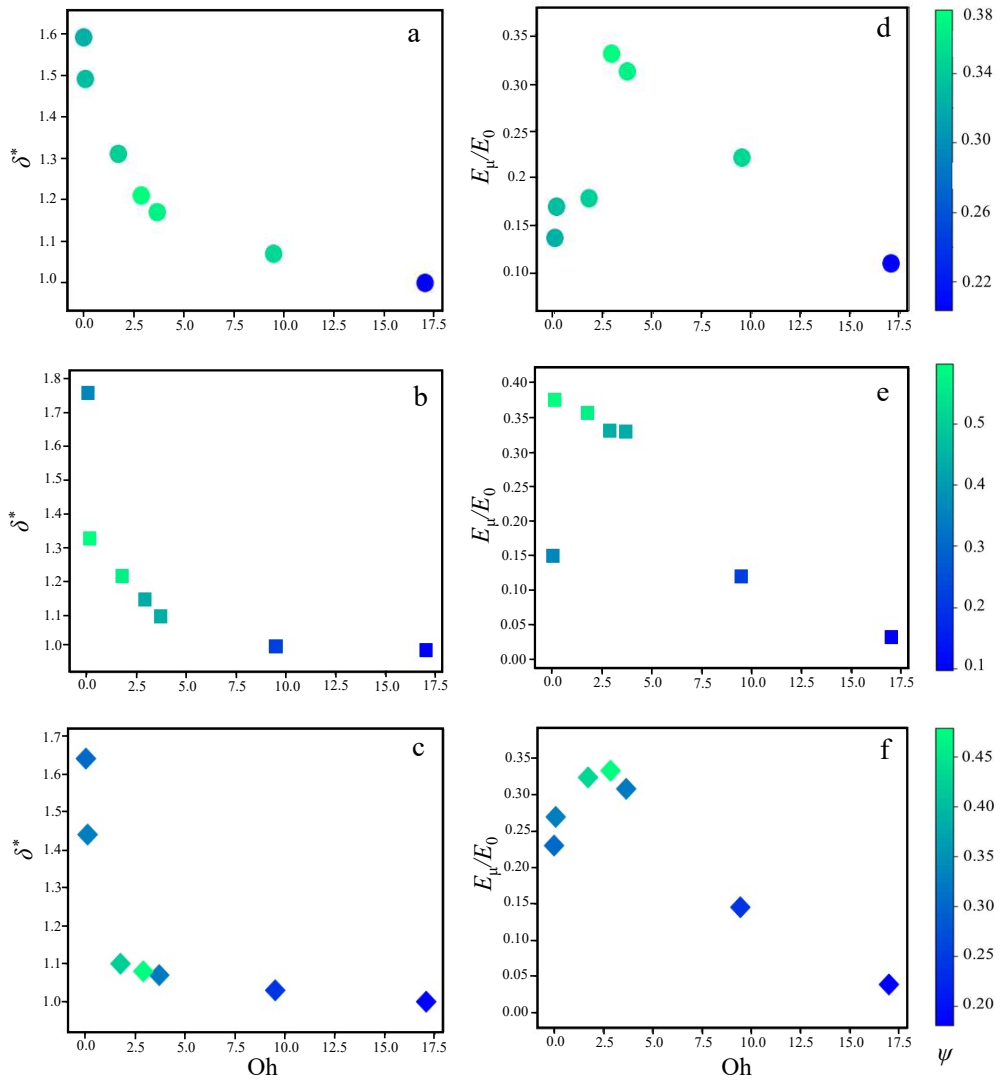

Figure 4.6: Flatness factor δ^* **(a-c)** and nondimensionalized viscous energy dissipation E_μ/E_0 **(d-f)** versus Ohnesorge number. Each row represents a different cantilever: 10-mil (a & d), 5-mil (b & e) and 2-mil (c & f). The color bar in each row applies to both panels in the row.

inherently enhances energy dissipation, we again see that viscosity reduces the number of oscillations a drop can undergo in a given time. We are again reminded there exists an intermediate viscosity which optimizes damping.

Like many other problems in fluid mechanics, we seek a dimensionless group that permits the incorporation of salient system properties. The most appropriate, previously used dimensionless group and includes fluid properties and frequency (to the author's knowledge) is the Womersley

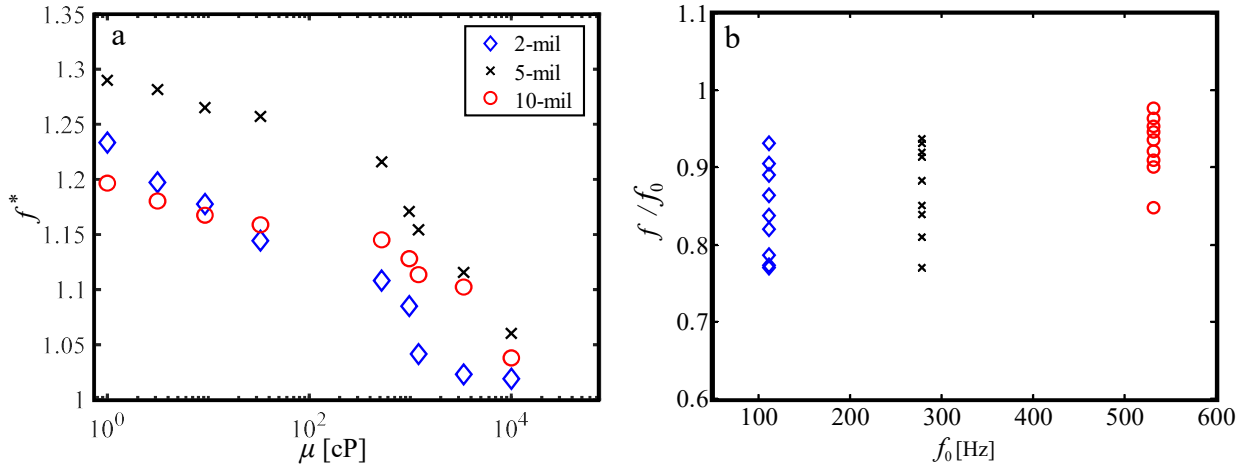

Figure 4.7: **(a)** Normalized vibration frequency versus drop viscosity. **(b)** Vibration frequency normalized by vibration frequency without added mass (f_0) versus f_0. The legend in (a) corresponds to both panels.

number [151] Wo $= L(2\pi f\rho/\mu)^{\frac{1}{2}}$, traditionally used to describe unsteady internal flow with a length scale L representing that of a solid boundary such as diameter. The Womersley number is limiting in our case because it does not permit the incorporation of both cantilever and drop length scales. We thus pose a new group, which we dub the Kauffman number, after a previous collaborator instrumental in our first cantilever studies, Jeffrey L. Kauffman [67],

$$\mathrm{Ka} = R\frac{\ell}{t_\mathrm{h}}\left(\frac{2\pi f\rho}{\mu}\right)^{\frac{1}{2}}. \tag{4.2}$$

The Kauffman number permits the incorporation of drop and cantilever length scales, and liquid properties. We have arranged Ka such that increasing terms in the numerator promotes drop deformation by increasing drop volume and inertia, and cantilever motion. Increasing the denominator magnitude reduces deformation by stiffening both solid and liquid. Drop placement distance from the tip $\ell - x_0$ is not included as a parameter, as it is fixed in our experiments, but is implicitly manifested in f, as is material stiffness. Cantilever width w, another fixed variable, is likewise excluded in Ka. Modification of Ka by a factor of $(\ell - x_0/w)$ could be included should drop location and w become variablized. Damping capacity ψ is plotted against Ka in Figure 4.5b. For each cantilever, Ka of $O(10^2)$ values permit the greatest damping, corresponding to moderately viscous

fluids. In practice, to maximize damping of a given cantilever, one could select a liquid (ρ, μ) and drop size (R) to achieve a Ka of the desired value. During fluid selection, the damped natural frequency imposed by a given liquid is unknown, but for $m_d/m_c \approx 1-6$, the ratio $f/f_0 \approx 0.8-1$ where $f_0 = 0.56(EI/m_c\ell^3)^{1/2}$ is the cantilever's damped natural frequency in first mode vibration without added mass. Thus, either a calculated or observed f_0 provides a convenient substitute for f when calculating an approximate Ka. We plot (f/f_0) in Figure 4.7b.

4.4 Discussion

In this study, we have experimentally determined the damping capacity of liquid drops resting on the free end of a vibrating cantilever. Our work may be compared to that of PIDs on cantilevers, which like drops, show decreased damping capacity at high levels of effective acceleration [40], typically in the range of $\psi \approx 0.1-0.2$. At the effective accelerations in which PIDs work best, $\psi \approx 0.8-1$ However, at effective accelerations $\Gamma < 2$, the damping capacity of particle dampers falls dramatically, presumably due to the cessation of movement of particles within the damper. No such decline in damping capacity is witnessed with liquid drops, which can experience internal flow with the slightest of external excitation. Thus a functional comparison can be drawn between the two types of dampers. Liquid drop dampers may be suitable for applications where damping is needed at small perturbation amplitudes or small surface accelerations, whereas PIDs, not prone to break apart or eject, are more robust to failure at larger surface accelerations. A direct comparison between drops and PIDs is difficult because the measure of ψ is tied to cantilever inertia, air damping, and internal damping in addition to damper properties. For example, our 2.2-mg, 2-mil cantilever topped with a solid mass has a greater damping capacity than some of the 38-g cantilevers topped with PIDs simulated by Mao *et al*(2004) [40].

The initial pluck amplitude of our system was chosen to ensure that drops never eject from our cantilevers. If ejection were no concern, we expect that specific damping would change very little

up to the point where drops fail in cohesion and break apart. The curves of Figure 4.4a-c indicate all test fluids approach a limit of ψ. The values of ψ for the 10-mil cantilever at $\Gamma = 400$ gravities are comparable to those at $\Gamma = 100$ gravities. The same behavior is seen with the other cantilevers, though at smaller effective acceleration ranges.

While wetting properties of the cantilever were held constant in our system, wettability is another means to tune drop damping. Hydrophobicity produces static drops which are more spherical, promotes contact line motion, and makes drops susceptible to ejection from the surface [67, 72]. Drop motion across the substrate is likely unfavorable because it is difficult to control. Hydrophilic surfaces, in contrast, will produce flattened static drops, encourage contact line pinning, and permit higher accelerations before drops leave the surface. We posit, based on our results in §4.1, the limited ability of flattened drops to undergo large deformation limits their ability to damp. Furthermore, pinned drops are not able to dissipate energy through contact line motion. Though we implicitly include dissipation by contact line friction, we are not able to separate it from viscous dissipation. Previous work [152, 153] has discovered a closed form expression of a contact line friction coefficient,

$$\zeta = \frac{\mu V_{\mathrm{m}}}{\lambda^3} \exp \frac{\sigma \lambda^2 (1 + \cos\theta_{\mathrm{c}})}{k_{\mathrm{b}} T} \tag{4.3}$$

where V_{m} is the molecular volume of the unit of flow, k_{B} is the Boltzmann constant, and T is the absolute temperature. There "no way of definitively predicting" the molecular jump distance λ from one potential well to another for a given solid-liquid combination [152]. However, Eq.(4.3) is illuminating in terms of how dissipation via friction scales with viscosity and surface tension. The identification of λ and V_{m} for a given system is a step toward optimizing liquid properties, μ and σ, to maximize damping.

The damping of the cantilever by a drop will be strongly correlated with the ratio of the cantilever to drop mass. Cantilevers of different density or thickness to the ones tested innately have different natural frequencies, which in turn modulates drop deformation, i.e. flatness factor, as shown in Figure 4.4d-f. Our most massive 10-mil cantilever has a cantilever-drop mass ratio of approximately

six, and experiences less damping than the 5-mil specimen with a mass ratio of three. For 2-mil thick cantilevers, the drop mass is roughly equivalent to the cantilever mass, sloshing drop can alter the cantilever phase, revealing two dominant frequencies as reported in Figure 4.3a,b. The emergence of two frequencies is perhaps the cause for less damping in the 2-mil cantilever than one might expect, but our physical understanding of this observation is limited.

The introduction of non-Newtonian fluids is another avenue for tuning the damping characteristics of drops but will dramatically increase the difficulty of predicting system behavior. The shear-stress dependency of non-Newtonian fluid properties dictates that damping capacity will be highly reliant on cantilever accelerations. At large accelerations, shear-thickening fluids will behave more solid, and perhaps see a dramatic reduction in damping capacity. Shear-thinning fluids could be prone to erratic breakup. The emergence of such behaviors is of course be governed by the matching of the solid and liquid composition.

We hope our results form a foundation for engineered systems to both use liquid damping, in the case of novel sensors, and thwart it, in the case of robotic flyers. The success of micro and nano aerial vehicles in all environments is critically dependent on their ability to cope with environmental hazards such as rainfall dewfall. The removal of moisture from flight critical surfaces may not be trivial for the smallest flyers [1, 73]. Vibration strategies specifically employed to dry wings much be chosen to maximize efficacy by minimizing input. A critical piece to effective self-drying is an understanding of vibration damping by the very mass a flyer seeks to remove.

CHAPTER 5: DROP EJECTION FROM VIBRATION DAMPED, DAMPENED WINGS

In this combined theoretical and experimental study we use cantilever vibration to induce drop motion, and consider the physics of drop motion across a range of cantilever wetting properties, drop position, fluid properties, vibration amplitude, and vibration frequency. We begin with the experimental determination of drop ejection modes in §5.1. In §5.2, we provide the tuning system properties to elicit modal behavior. We provide the damping produced by the sloshing of drop in §5.3 and finally We discuss our theoretical simplifications and implications of our research in §5.4

5.1 Experimental determination of drop ejection modes

We perform a series of drop release experiments from forced, millimetric cantilevers, filmed using a high-speed camera. Drops of water and a 1:1 water-glycerin solution by volume are released from a polymeric cantilever within milliseconds, and we observe drop ejection can be a complicated, multi-stage event in which fluid removal occurs through multiple mechanisms in sequence, which is particularly true for drops larger than the capillary length. However, we observe three principal modes of drop release that can be singly witnessed under the appropriate set of cantilever and drop conditions. We categorize these three release modes as sliding, normal-to-cantilever ejection, and pinch-off, which we discuss in turn, and summarize in Table 5.1. Normal-to-substrate ejection (Movie S5) occurs when beam accelerations from small deflections produce receding contact lines. Inertial force must overcome the drop adhesion without drops failing cohesively. Sliding (Movie S4) occurs for relatively larger deflections allowing tangential inertial force to overcome contact angle hysteresis. In pinch-off (Movie S6), inertial force generates contact line motion but the drop ultimately fails in cohesion, leaving a small child droplet attached to the substrate. Three ejection modes are highly correlated with the selection of cantilever wetting properties, vibration characteristics, and drop location and size. Photo sequences of drop deformation and time to com-

plete release are shown in Figure 5.3a-c. The expression of these modes is determined by cohesion forces F_{coh}, adhesion forces F_{ad}, and inertial forces F_i, in normal (N) and tangential (T) directions. Following the presentation of release modes, we show how drop and cantilever properties may be adjusted to elicit a particular mode.

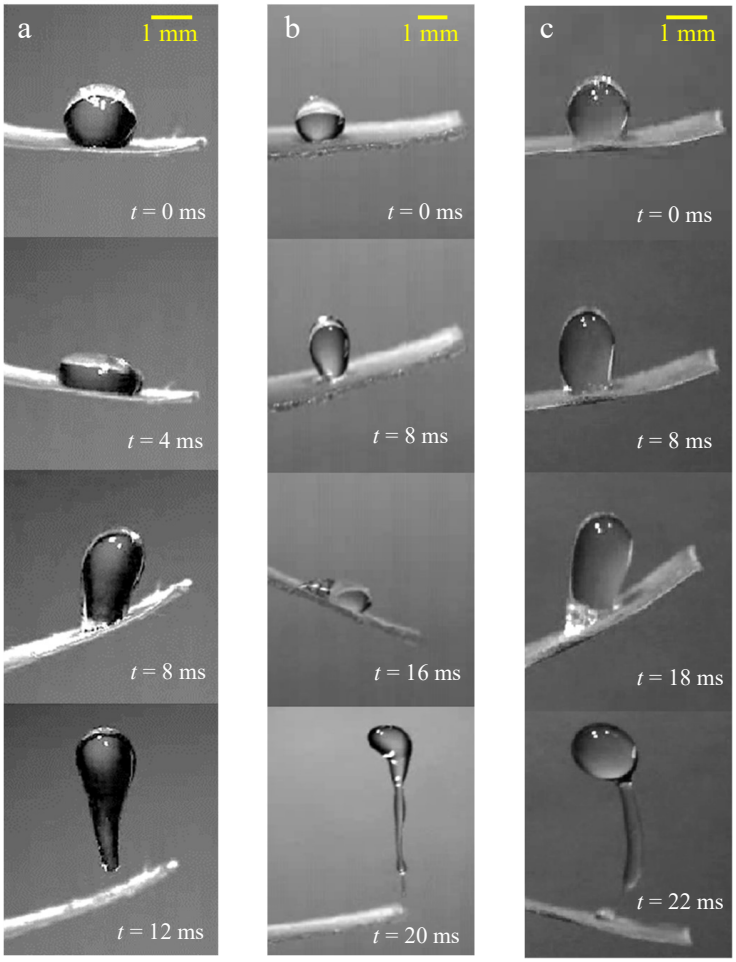

Figure 5.1: Photo sequences of drop ejection via **(a)** normal **(b)** sliding and **(c)** pinch-off.

5.1.1 Sliding

Sliding of a mobile drop from the end of a cantilever is depicted in **Fig.5.3**a. This type of ejection occurs for cantilevers undergoing relatively large deflections angle $\alpha = 18° - 25°$ (Figure 5.4), and requires tangential accelerations sufficient for continuous unpinning of contact lines [79]. There-

Table 5.1: Combined ejection mode summary for water and a 1:1 water-glycerin mixture by volume, atop cantilevers with an impulsively-started base.

Mode	**Ejected mass** [%]	**Contact angle** [°]	**Inertial ejection force** [mN]	**Acceleration** (impulsively started base) [g]
Sliding	100	$\gtrsim 135$	$F_{\mathrm{i,T}} = 0.18 - 0.3$	7 - 18
Normal	100	$\gtrsim 135$	$F_{\mathrm{i,N}} = 0.18 - 0.25$	14 - 24
Pinch-off	92-95	$\lesssim 135$	$F_{\mathrm{i}} = 0.15 - 0.52$	15 - 37

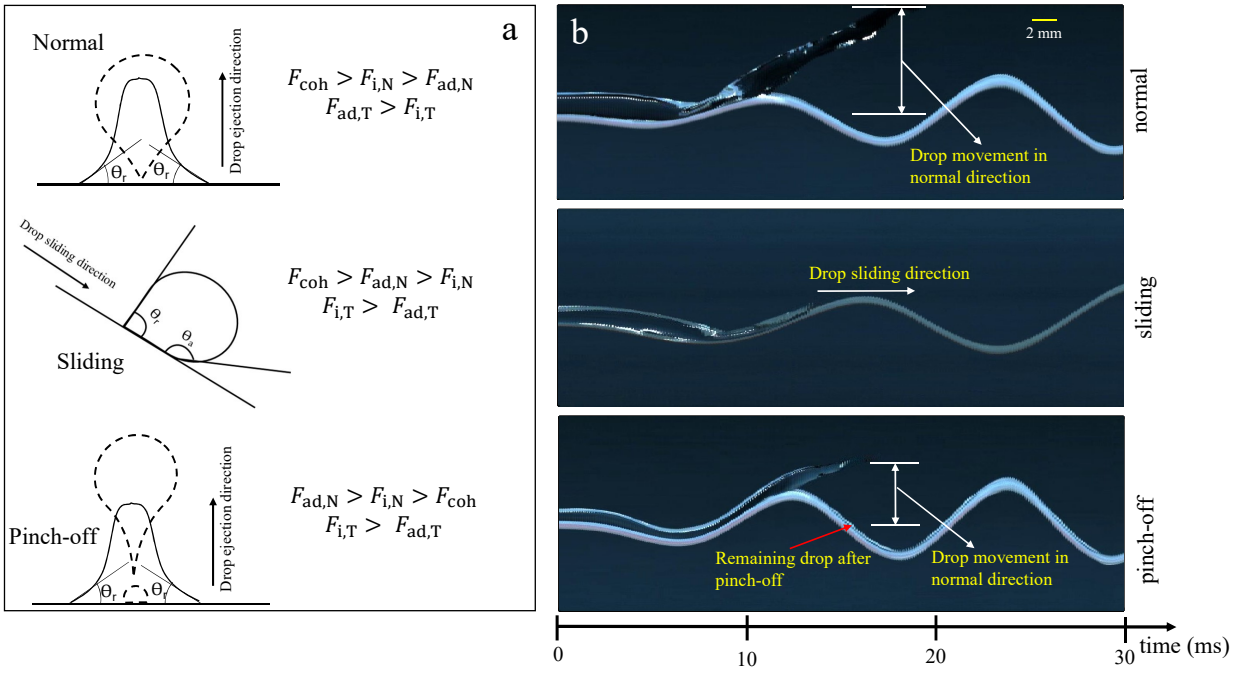

Figure 5.2: **(a)** Schematics and **(b)** kymographs of drop release modes.

fore, this type of release cannot be ascertained with an infinitely rigid cantilever with a translating base. The photo sequence in Figure 5.3d (Movie S4) was garnered using a hydrophobic ($\theta_{\mathrm{e}} = 141°$), 10mm cantilever. A track of the cantilever directly beneath the drop at x_0 and water drop crest is shown in Figure 5.3g, for the system pictured in Figure 5.3d. The drop begins to slide 11 ms after motion inception and severs contact with the cantilever tip at 19 ms.

To slide the drop tangentially along the cantilever, system forces in Figure 5.4 must satisfy the

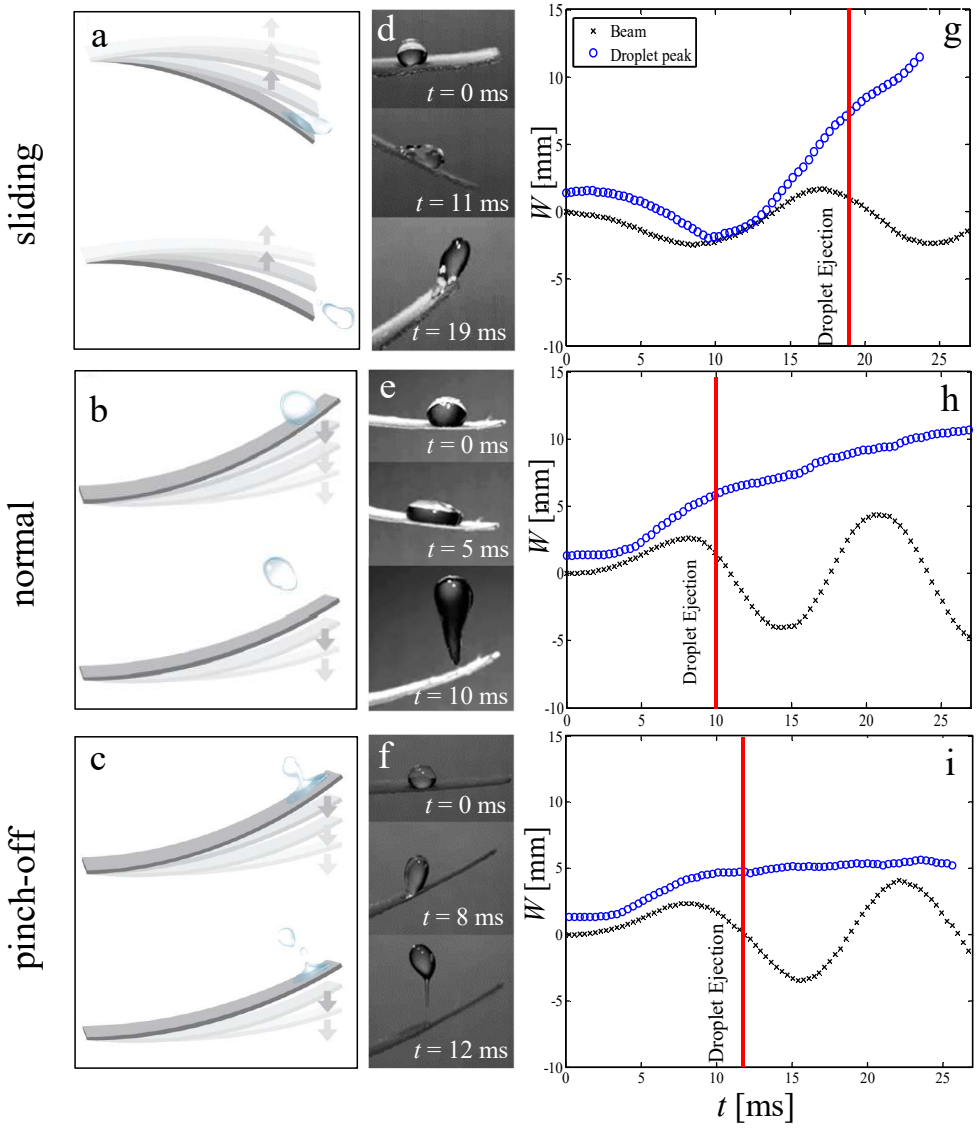

Figure 5.3: Drop ejection modes. **(a)-(c)** Schematics of modes. **(d)-(f)** Photo sequences of ejections at 85 Hz. **(g)-(i)** Temporal deflection W of cantilever tip and drop crest.

following:

$$\underbrace{F_{\mathrm{ad,N}} > F_{\mathrm{i,N}}}_{\text{no normal ejection}} \quad \varsigma \quad \underbrace{F_{\mathrm{coh}} > F_{\mathrm{ad}}}_{\text{no drop pinch-off}} \quad \varsigma \quad \underbrace{F_{\mathrm{i,T}} > F_{\mathrm{ad,T}}}_{\text{inertia overcomes hysteresis}} \tag{5.1}$$

Inertial force must overcome liquid-solid adhesion and produce mobile contact lines. Such adhesion force depends on the drop's advancing and receding contact angles, θ_{a} and θ_{r} respectively [154, 79,

155, 156, 157, 158, 159, 160], such that

$$F_{\mathrm{ad,T}} = k_{\mathrm{s}} R\sigma(\cos\theta_{\mathrm{r}} - \cos\theta_{\mathrm{a}}), \tag{5.2}$$

where R is the spherical drop radius. The factor k_{s} may be determined experimentally or analytically, but there exists no consistent value in literature, even for simple geometries and one-dimensional substrate motion [154]. If contact angle hysteresis, and thus adhesion, is high for cantilevers experiencing high tangential forces, drops may remain pinned and experience tangential pinch-off, covered below in §5.1.3. The critical tangential force to produce sliding $F_{\mathrm{i,T}} = 0.18 - 0.3$ mN is found from video analysis by tracking the motion of the cantilever at the drops' points of contact. The drop mass is calculated by assuming the drop has a spherical curvature above the cantilever [161],

$$m_{\mathrm{d}} = \rho\pi\left[\frac{4}{3}R^3 - R^2h' + \frac{(h')^2}{3} - (h')^2\cos\theta_{\mathrm{e}} + R^2h'\cos^2\theta_{\mathrm{e}}\right], \tag{5.3}$$

where h' is the distance the sphere would protrude below the cantilever. Further discussion of Eq.(5.3) is provided in the Online Supplement. We find that sliding is more frequently observed with the glycerin solution. These drops have $\theta_{\mathrm{r}} = 92 \pm 3°$ (N= 7), $\theta_{\mathrm{a}} = 142 \pm 2$ (N= 7), $\sigma = 67.5 \pm 0.5$ dyn/cm (N= 3), $R = 0.6 - 0.9$ mm and $\rho = 1.12$ g/cm^3. By setting $F_{\mathrm{i,T}} = F_{\mathrm{ad,T}}$, we find $k_{\mathrm{s}} = 3.06$, $\mathrm{R}^2 = 0.982$ from Eq.(5.2) and as shown in Figure 5.5a, which agrees with the value reported in a previous study [162], $k_{\mathrm{s}} = \pi$.

5.1.2 Normal-to-substrate ejection

Normal-to-substrate ejection, as depicted in Figure 5.3b, occurs when a drop is released from the surface along to the outward-facing normal and no portion of the drop remains adhered to the surface. This type of ejection is most probable for stiff, high hysteresis cantilevers where cantilever angle deflection is relatively small ($\alpha = 6° - 13°$), imbuing tangential acceleration less than normal

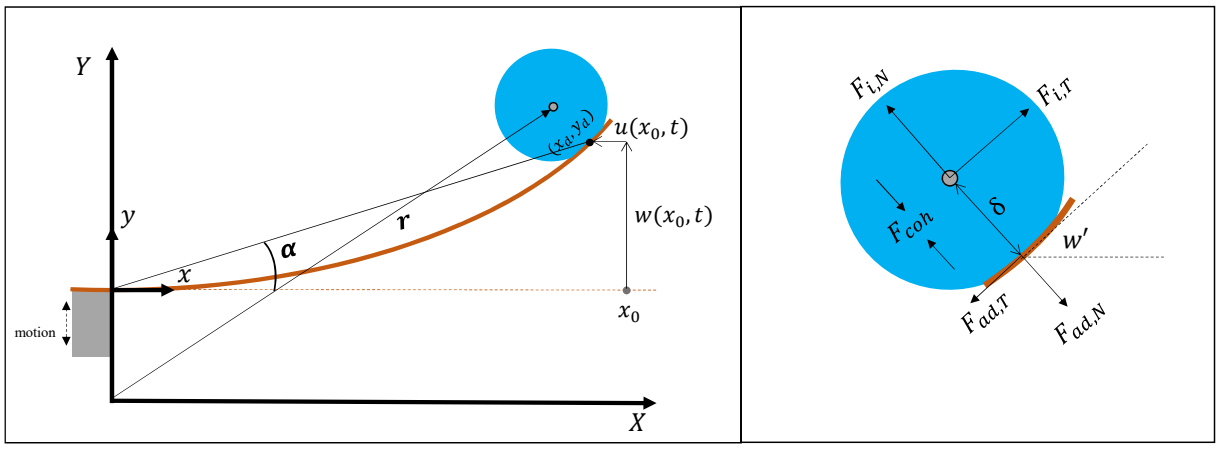

Figure 5.4: Free body diagram of liquid drop on a cantilever under deflection.

acceleration. Figure 5.3h shows a vertical track of the cantilever directly beneath the drop at x_0 and the water drop's crest for the system pictured in Figure 5.3e (Movie S5) experiencing normal ejection at 85 Hz. Prior to ejection the drop flattens, storing surface energy before leaving the substrate as the solid cantilever changes direction. This particular drop is released from the cantilever at 10 ms from motion inception, and cantilever amplitude grows 300% within one cycle following drop departure.

For normal-to-substrate ejection, the forces depicted in Figure 5.4 must satisfy the following:

$$\underbrace{F_{\mathrm{i,N}} > F_{\mathrm{ad,N}}}_{\text{inertia overcomes adhesion}} \quad \varsigma \quad \underbrace{F_{\mathrm{coh}} > F_{\mathrm{ad}}}_{\text{no drop pinch-off}} \quad \varsigma \quad \underbrace{F_{\mathrm{ad,T}} > F_{\mathrm{i,T}}}_{\text{no drop sliding}}, \tag{5.4}$$

Cantilever accelerations produce nearly axissymmetric contact line motion in this release mode such that the entire circular contact line assumes the receding contact angle, $\theta_{\mathrm{r}} = 124 \pm 3°$ (N= 9). Thus the critical adhesion force that must be overcome by inertia can be expressed

$$F_{\mathrm{ad,N}} = k_{\mathrm{n}} R\sigma(\cos\theta_{\mathrm{r}} + 1), \tag{5.5}$$

where the factor k_{n} is determined experimentally. The critical normal force to eject drops via this

mode $F_{i,N} = 0.18 - 0.25$ mN. By setting $F_{i,N} = F_{ad,N}$, we find the value of $k_n = 6.42$ ($R^2 = 0.60$) for a 50% glycerin solution, whereas for water $k_n = 6.33$ ($R^2 = 0.77$), as shown in Figure 5.5b. Both k_n values are approximately 2π, an experimental confirmation that adhesion is directly proportional to the contact line perimeter in normal-to-substrate movement. There is no k_n value for comparison given in literature to the authors' knowledge.

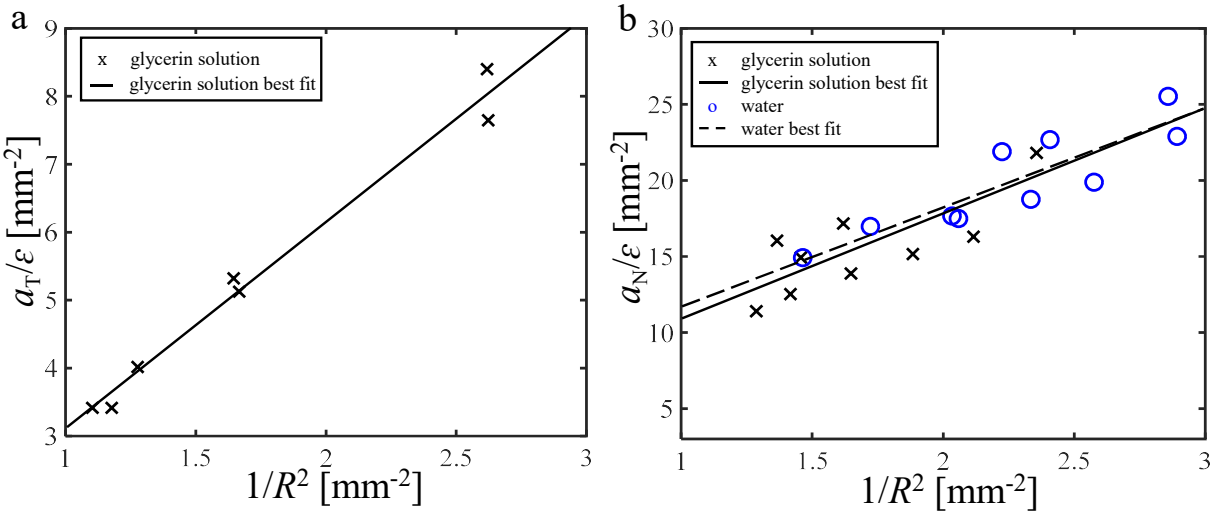

Figure 5.5: **(a)** Kinematic data of sliding drops for a 1:1 water-glycerin solution by volume for the determination of k_s. **(b)** Kinematic data of normal movement for water drops and drops of a 1:1 water-glycerin solution by volume for the determination of k_n. a_T in (a) is the tangential component and a_N is the normal component of acceleration of the beam at the time of ejection. The constant $\varepsilon = 3\sigma\left(\cos\theta_r - \cos\theta_a\right)/2\pi\rho$ for (a) and $\varepsilon = 3\sigma\left(1 + \cos\theta_r\right)/2\pi\rho$ for (b).

5.1.3 Pinch-off

During pinch-off, a portion of the adhered drop is flung from the cantilever while another portion is left attached, as depicted in Figure 5.3c. Pinch-off ejections typically exhibit contact line motion prior to mass release, leaving the portion remaining on the substrate with a considerably smaller radius than the parent drop. A characteristic of pinch-off not observed in the previous two modes is the liquid bridge, or neck, connecting the mobile and stationary portions of the drop at ejection. Pinch-off separation occurs via three modes: neck closure at the pinned liquid body (Figure 5.3f), neck closure at the releasing drop, and simultaneous closure of the neck at two locations (Movie

S6). In the latter case, the neck itself becomes a satellite drop, or two. We do not differentiate pinch-off releases by neck closure scenarios in the ensuing discussion. A track of the cantilever directly beneath the drop at x_0 and drop crest for a pinch-off ejection is shown in Figure 5.3i, for the system pictured in Figure 5.3f. The bulk, $\sim 95\%$, of the drop separates from the substrate at 12 ms following the onset of base motion.

To eject liquid via pinch-off, system forces must satisfy the following:

$$\underbrace{F_{\mathrm{ad}} > F_{\mathrm{coh}}}_{\text{adhesion exceeds drop cohesion}} \quad \varsigma \quad \underbrace{F_{\mathrm{i}} > F_{\mathrm{coh}}}_{\text{inertia exceeds drop cohesion}} \tag{5.6}$$

Previous numerical studies have considered drop ejection and pinch-off from a vertically moving substrate [163, 164, 104], but the unpredictable and ephemeral nature of a deforming drop's curvature ensures no analytical expression for F_{coh}. However, we find the occurrence of pinch-off depends strongly on surface wettability, as discussed in §5.2, while time to pinch-off highly depends on the history of system motion, discussed in §5.3. Pinch-off release from static capillary tubes has been well-characterized [165, 166] and provides a tool to describe the pinch-off in our system. Our experiments with water reveal that drop release from cantilevers via pinch-off satisfies a modification of Tate's Law [2],

$$m_{\mathrm{e}} = \frac{2\pi\sigma R_{\mathrm{p}}}{a_c} G(R_{\mathrm{c}}, x_o, \theta_{\mathrm{e}}) \tag{5.7}$$

where $m_{\mathrm{e}} = 0.7 - 5.66$ mg is the ejected drop mass, $R_{\mathrm{p}} = 0.56 - 1.14$ mm is the radius of the parcel of fluid remaining attached to the substrate and $a_{\mathrm{c}} = 149 - 365$ m/s^2 is the magnitude of substrate acceleration at the moment of pinch-off. We estimate the correction factor G as a constant function, as done previously [2, 167]. We plot m_{e} against dimensionless drop size R_{c}/ℓ_c in Figure 5.6a, and provide experimental data from dripping capillary tubes [2] for comparison. We do not expect G to match that for glass capillaries, which have a contact line perimeter fixed to the tube lip. We further justify the treatment of F as constant by observing the relation between m_{e} and $R_{\mathrm{p}}/a_{\mathrm{c}}$, plotted in

Figure 5.6b, and find $G = 0.34$ ($R^2 = 0.94$) for water and $G = 0.39$ ($R^2 = 0.95$) for the glycerin solution vibrated at 85 Hz. The correction factor G in our system is independent of frequency. For water, $G = 0.29$ ($R^2 = 0.94$) and $G = 0.30$ ($R^2 = 0.90$) for 100 Hz and 115 Hz, respectively, and the associated data is plotted in Figure A.7. Surprisingly, the above values of G are very similar to that found in a previous study on drop release from clumps of mammalian fur [167], suggesting universality in inertia-driven drop ejection systems. Like the fur, extrapolated values of m_e will reach zero for non-zero R_p, indicating the smallest drops cannot be removed via pinch-off.

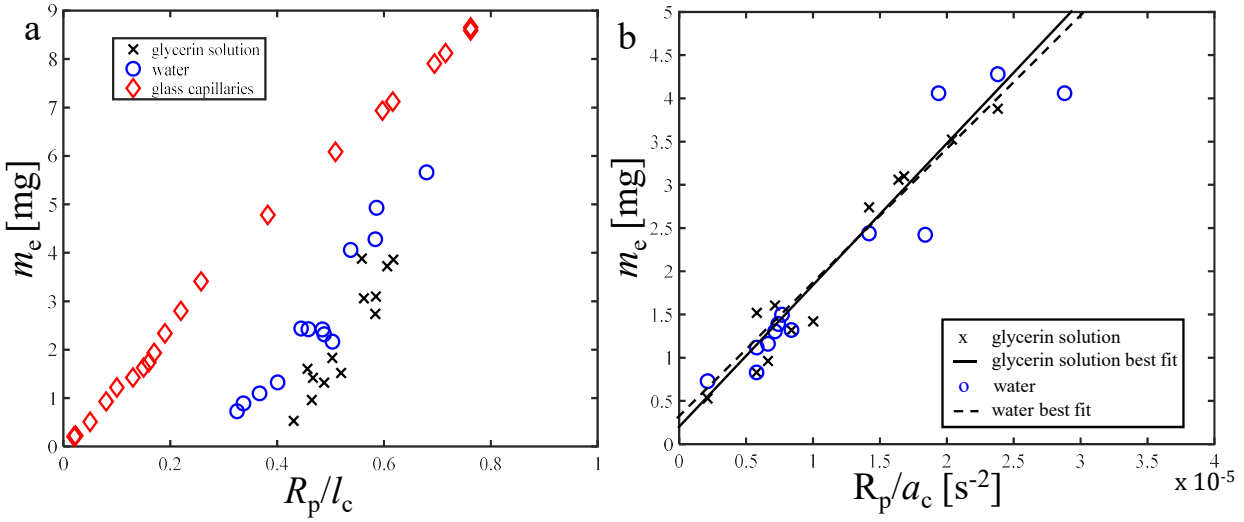

Figure 5.6: Drop release via pinch-off. **(a)** The dependence of released mass on the size of the initally deposited drop. The mass of drops dripping from glass capillaries is shown for comparison [2]. **(b)** The relation between released drop mass and cantilever acceleration of drop release. Best fits in (b) are given by Eq.(5.7) using $G(R_c, x_o, \theta_e) = 0.34$ for water and 0.39 for 1:1 glycerin solution by volume at 85 Hz.

5.2 Tuning system properties to elicit modal behavior

The selection of system variables such as cantilever length L (a proxy for stiffness), drop location x_0, R, and θ_e allows for the solicitation of a particular ejection mode. By fixing some system parameters and varying others using a singular 10-mm long PTFE cantilever, we find ejection modes appear as groups in the parameter space, as shown in the plots for water (Figure 5.7a,c) and glycerin solution (Figure 5.7b,d). In Figure 5.7a,b, we fix x_o, and vary R and θ_e. The most hydrophobic cantilevers

display primarily normal ejection modes, with the most wetting cantilevers tending toward pinch-off.

To define the equilibrium contact angle $\theta_{\mathrm{e,t}}$ at the transition of normal and pinch-off ejections in Figure 5.7a,b, we equate $F_{\mathrm{ad,N}} = m_{\mathrm{e}} a_{\mathrm{c}}$ from Fn,tate, to find the receding contact angle at this threshold,

$$\theta_{\mathrm{r,t}} = \arccos\left(\frac{2\pi G}{k_{\mathrm{n}}} - 1\right), \tag{5.8}$$

as the contact line of a drop at the transition of normal and pinch-off ejection draws inward to occupy an area smaller than the unperturbed drop (Figure 5.3). If the contact line motion ceases, the drop will pinch off in cohesion failure. At this critical juncture, we assume the radii of interest in Fn,tate are equivalent because both refer to the adhesion at the contact line. Thus, $\theta_{\mathrm{r,t}}$ is independent of drop size, which is supported by Figure 5.7a,b. For water $\theta_{\mathrm{r,t}} = 132°$ and for the glycerin solution $\theta_{\mathrm{r,t}} = 128°$. The values of $\theta_{\mathrm{e,t}}$ corresponding to $\theta_{\mathrm{r,t}}$ are found theoretically by [168]

$$\theta_{\mathrm{e,t}} = \arccos\left(\frac{A\cos\theta_{\mathrm{a}} + B\cos\theta_{\mathrm{r,t}}}{A+B}\right), \tag{5.9}$$

$$\text{where } A = \left(\frac{\sin^3\theta_a}{2-3\cos\theta_{\mathrm{a}}+\cos^3\theta_a}\right)^{\frac{1}{3}};\ B = \left(\frac{\sin^3\theta_{r,c}}{2-3\cos\theta_{\mathrm{r,t}}+\cos^3\theta_{r,c}}\right)^{\frac{1}{3}}.$$

We set the value of $\theta_{\mathrm{a}} = 150°$ (N=8) by measuring those from normal ejections. The resulting values for water and the glycerin solution are $\theta_{\mathrm{e,t}} = 138°$ $\theta_{\mathrm{e,t}} = 136°$, respectively, and delineate the regions in Figure 5.7a,b. The relative values of this pinch-off threshold for the two fluids can be explained by the slightly lower surface tension of the glycerin solution, 92.5% that of water.

In Figure 5.7c,d, we fix $\theta_{\mathrm{e}} = 136.3 \pm 2.1°$ (N= 34) whilst varying R and x_{o}. We find the occurrence of release modes is more strongly depends on drop location x_{o} than R. Drops located nearer the cantilever tip experience ejection forces more rapidly following base motion startup because a number of cycles are required for maximal cantilever deflection. Rapid release thus favors sliding and normal ejections, before the drop is allowed to significantly deform. A comparison of drop

deformation and time to contact line motion is given in Figure 5.8. We explore the role of drop sloshing in §5.3.

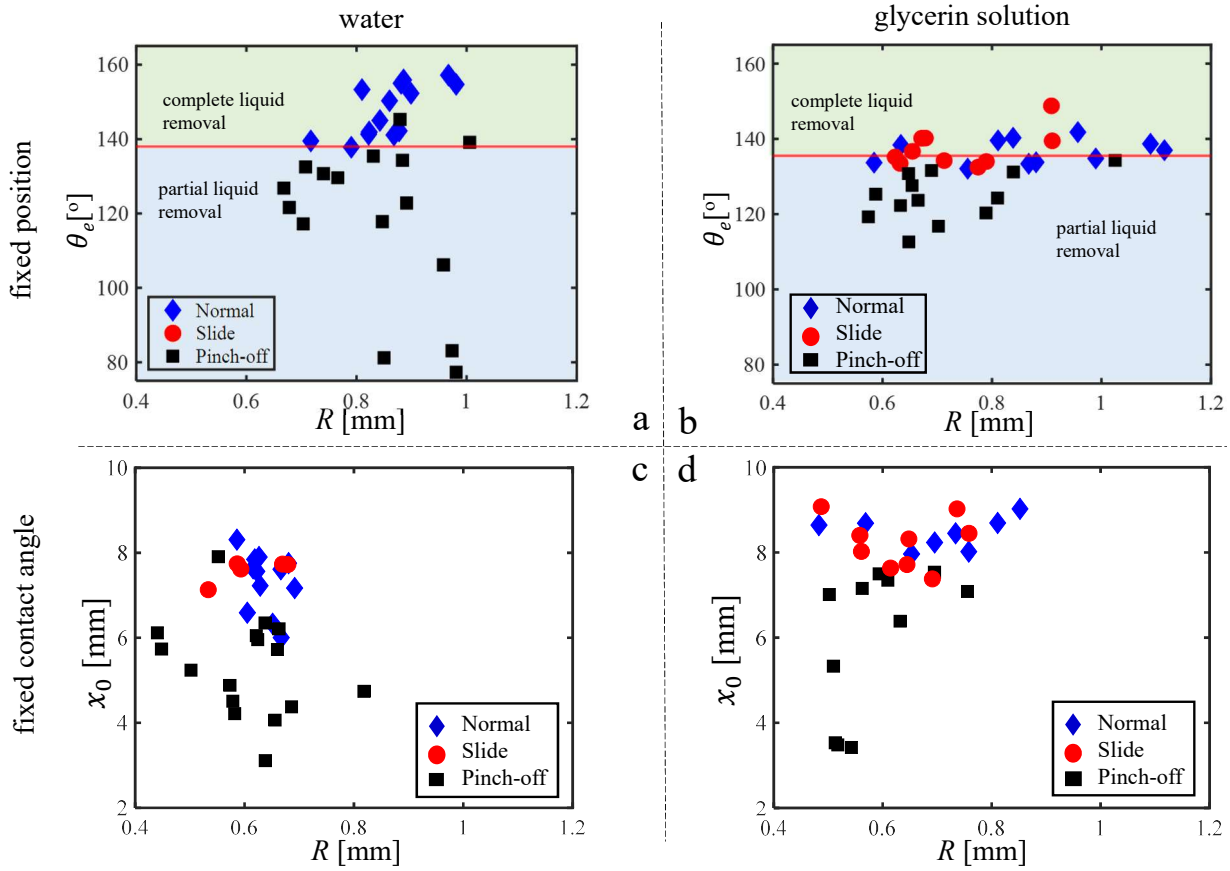

Figure 5.7: Ejection mode plots for water (a,c) and 1:1 water-glycerin solution (b,d), for fixed drop position x_0 (a,b) and fixed equilibrium contact angle θ_e (c,d).

5.3 Drop sloshing damps vibration

In §5.1, we present ejection results for which base motion amplitude is fixed, producing ejections within two vibration cycles. We now allow base amplitude to linearly increase with time to establish a greater history of drop deformation by extending time to ejection. To quantify the damping induced by drop sloshing we match idealized deflection, with rigid masses, to experimental deflection curves with deforming drops. In the following subsection we present our deflection model that determines temporal cantilever shape and provides damping coefficients and inertial force.

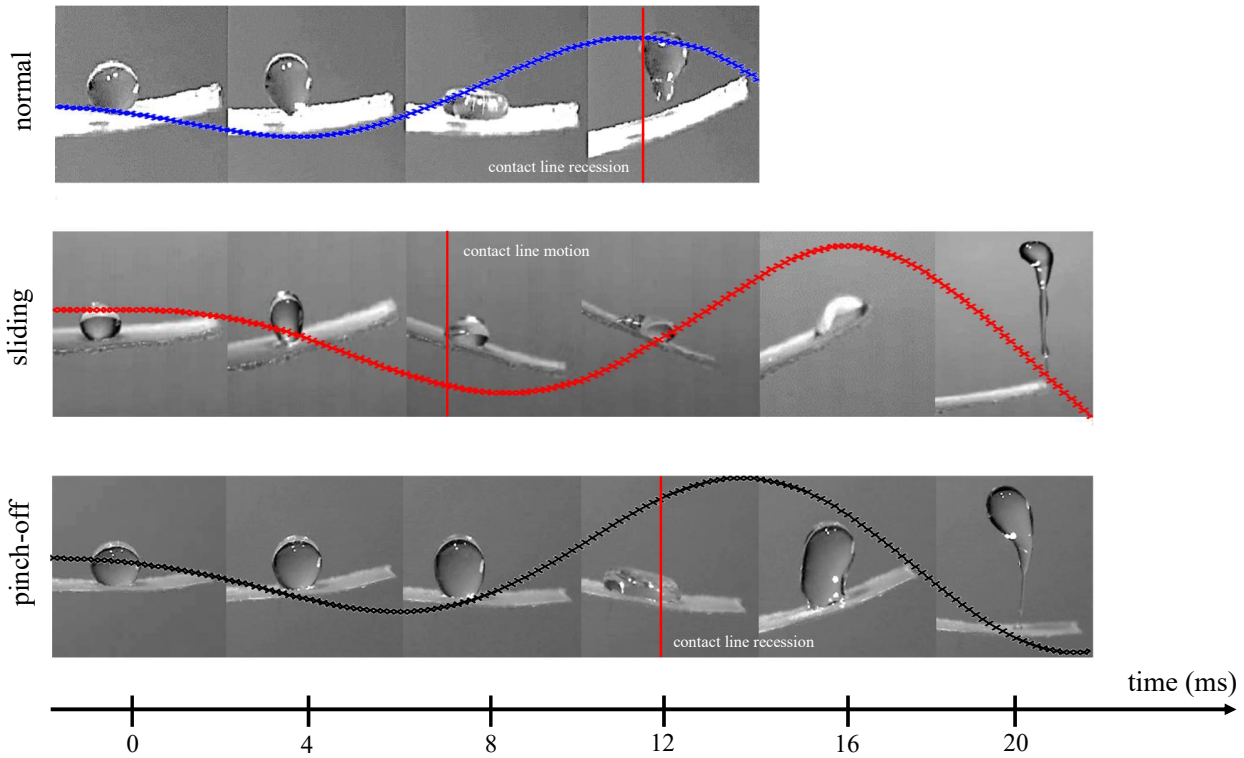

Figure 5.8: Photo sequences of ejection modes with cantilever tip deflection tracks overlaid to highlight the onset of contact line motion. Time stamps on the timeline correspond to photos, with $t = 0$ corresponding to the onset of base motion.

We compare an experimental cantilever track to one produced from theory in Figure 5.9 (Movie S7). The shaker base begins at rest and linearly increases to a $\pm$1-mm maximum amplitude. The theoretical and experimental amplitudes deviate in the earliest cycles due to transient effects inside the shaker at startup. After ejection, the experimental cantilever increases amplitude due to lower mass, a reduction the theoretical curve does not contain. Ejection time from the experiment is passed to the model, and various values of the damping coefficient c are input into Eq.(3.34) such that the amplitude of the two tracks at the time of ejection is within 10%. By varying $\theta_e = 119 - 149°$ for a fixed x_0, we find $c \approx 0.1 - 0.52$ kg/s for pinch-off and $c \approx 0.02 - 0.19$ for normal, as shown in Figure 5.10a. No sliding ejections were witnessed using this method of cantilever excitation. The greater value of damping for pinch-off drops is supported by the observation of increased sloshing prior to ejection via this mode. As in Figure 5.7a, the equilibrium contact angle at the transition between the two modes is approximately 138°.

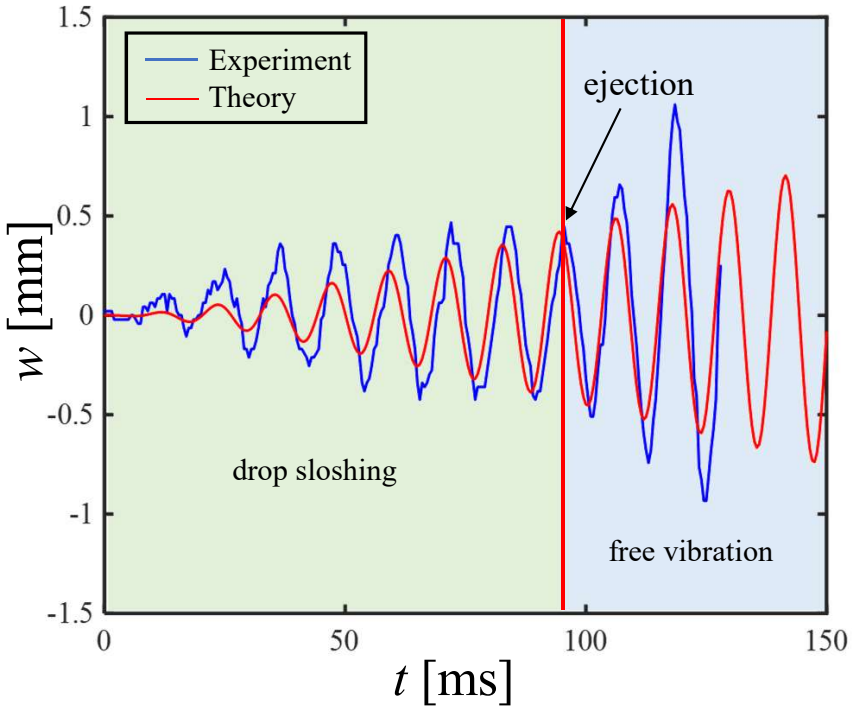

Figure 5.9: Comparison of experimental and theoretical of cantilever deflection with a 1.8 mg drop of water vibrated at 85 Hz.

The force of ejection garnered by matching theoretical and experimental tracks is shown in Figure 5.10b. Not surprisingly, pinch-off ejections occurring at lower contact angles require, on average, greater inertial force. In this experiment, the majority of normal ejections occur at accelerations below 10 g, while pinch-off ejections occur between $10-45$ g. From this experiment we may conclude that lowering contact angle will require greater base input for drying due to both higher damping from drop sloshing and increased adhesion.

5.4 Discussion

From our experiments, we find the value of the fitting constant $k_n \approx 2\pi$ is greater than $k_s \approx \pi$, suggesting that inertial forces to cause sliding are less than those required for normal-to-substrate motion. The values of acceleration at ejection in Table 5.1 likewise support this notion. It is thus surprising that sliding ejections are seen relatively infrequently. We posit the lack of sliding ejec-

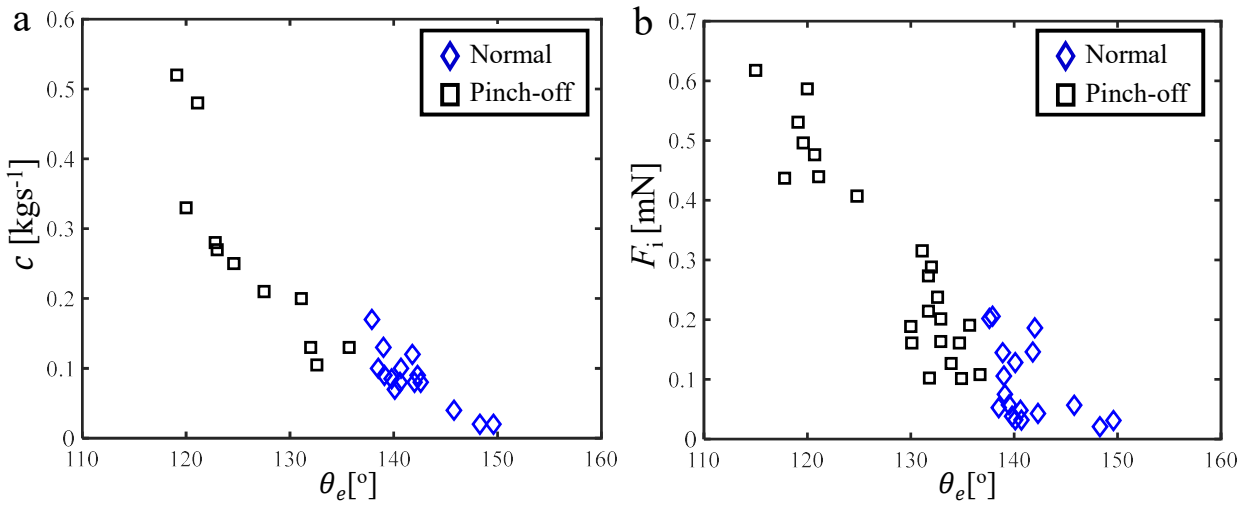

Figure 5.10: Plots of **(a)** damping coefficient and **(b)** inertial force versus equilibrium contact angle, determined by a combination of experiments with water and theory.

tions can be explained by relative magnitudes of normal and tangential forces generated by our cantilevers. Sliding, for a fixed contact angle, occurs only at $x_0 > 7$ mm for a 10 mm cantilever, as seen in Figure 5.7c,d. At locations closest to the tip, the cantilever experiences the greatest deflections w and thus the greatest $F_{\mathrm{i,T}}$. We expect longer cantilevers to exhibit a greater number of sliding ejections. Shorter, and thicker cantilevers will favor normal ejections. The influence of a greater range of base frequency and amplitude on ejection behavior remains an area for future work, as is the selection of base kinematics to minimize the energetic costs of drying. Shorter, softer cantilevers more closely mimicking mosquito wings, for example, will likely dry most efficaciously at higher frequencies.

The factor $k_{\mathrm{s}} \approx \pi$ in Eq.(5.2) matches that of an ultrasonically vibrated surface [79], demonstrating the universality in drop sliding. Though not reported, we expect $k_{\mathrm{s}} \approx \pi$ for sliding drops in shear flow[84]. Shear flow may also produce pinch-off drops when the capillary number $\mathrm{Ca} = \mu_{\mathrm{s}} \dot{\gamma} R/\sigma \gtrsim 0.1$, where the shearing gas has a viscosity μ_{s}, and shears the drops at a rate of $\dot{\gamma}$. We occasionally witness a very similar scenario in our system, where the drop begins a slide when $F_{\mathrm{ad,T}}$ is dominant, but halts contact line movement and finishes as a pinch-off ejection. In our system, $\mathrm{Ca} \leq 0.0002$, which is determined by using a maximum cantilever ejection velocity of 0.9 m/s returned from the

model of §3.3.1. Such a low value of Ca indicates the effects of the surrounding gas on ejection are negligible.

The magnitude of drop sloshing and its associated damping is a function of drop viscosity. Viscous effects dissipate energy, so one might expect more viscous drops to impose greater damping on cantilever motion. This is perhaps true to a point where increasing viscosity lessens damping by limiting the drops' ability to deform. Such an inflection in damping behavior will depend on cantilever kinematics such as amplitude, frequency, and modal shape. Damping across a range of viscosity is an area for future work.

In this study we identify three ejection modes that have analogous behaviors in a nearly reversed scenario, drops impacting freely supported objects [169]. When a freely supported object is struck by a falling drop of the same order in size, the drop may (1) *push* the object, remaining intact, (2) *coat* the object, or (3) *splash*. The occurrence of these 'impact modes' for water is determined by the ratio of drop-to-target mass, and drop-to-target radius. A push is analogous to normal-to-substrate ejection. The drop can deform but experiences little contact line motion. A coat is most analogous to sliding, as both drops remain intact but experience extensive advancing and receding contact line motion. Finally, splashing and pinch-off both experience inertial forces overcoming surface forces to inflict drop fragmentation.

Our model in §3.3.1 is an example of a transient response of forced spring mass damper systems with base excitation. Traditional studies of cantilever motion fix the base, and employ finite difference [170, 171] and finite element [172, 173, 174] methods. Using an assumed mode construction we are able to replicate the cantilever displacement in terms of an assumed static deflection shape and a rigid body displacement mode. This approach is mandated by the complexity of predicting cantilever shape with a translating base, producing highly nonlinear behavior. Although our model does not incorporate two-phase behavior, it sets a foundation by which future researchers can investigate substrate motion with time-dependent inertial loading by fluids.

CHAPTER 6: PREDICTING MODELING OF DROP EJECTION FROM DAMMED, DAMPENED WING BY MACHINE LEARNING

In this chapter, we employ ensemble learning to tackle the classification problem of predicting drop ejection modes from a forced cantilever beam across a range of surface wettability, drop position, and drop size. Another set of base learners is used to perform a regression analysis to predict the related inertial forces. We thus characterize drop ejection across a greater range of system variable values than we have explored experimentally. The predictive results from our algorithm for the classification of ejection mode are presented in §6.1. We present the prediction results of minimum inertial force required to eject a drop in §6.2 and provide concluding remarks in §6.3.

6.1 Ensemble prediction of drop ejection modes

Drop release experiments are performed using a horizontal 10-mm cantilever and a singular drop of water or a 1:1 water-glycerin solution by volume resting on the upward-facing surface. To produce a particular ejection mode, we vary drop location x_0, drop size R, liquid viscosity μ, and contact angle θ_e while noting ejection type and measuring ejection time t. We plot the distribution of the three principal ejection modes by pairwise system variables in Figure 6.1. Ejection modes appear as clusters in the physical variable space. The diagonal in **Fig.6.1** shows the univariate distribution of the data for the variable in the respective column. The surface tension σ of water (72.9 dyne/cm) and 1:1 water-glycerin solution by volume (67.5 dyne/cm) are within 7% and density within 2% of one another. Thus, we do not include surface tension or density as variables. The viscosity of the glycerin solution, however, is $\mu = 6.13 \pm 0.05$ cP (N = 3), or approximately 7 times that of water. Data corresponding to μ in Figure 6.1 appears in rows and stacks because only two discrete viscosity values are put on the test. These plots, particularly the rightmost histogram, likewise demonstrate sliding is more rarely witnessed for pure water.

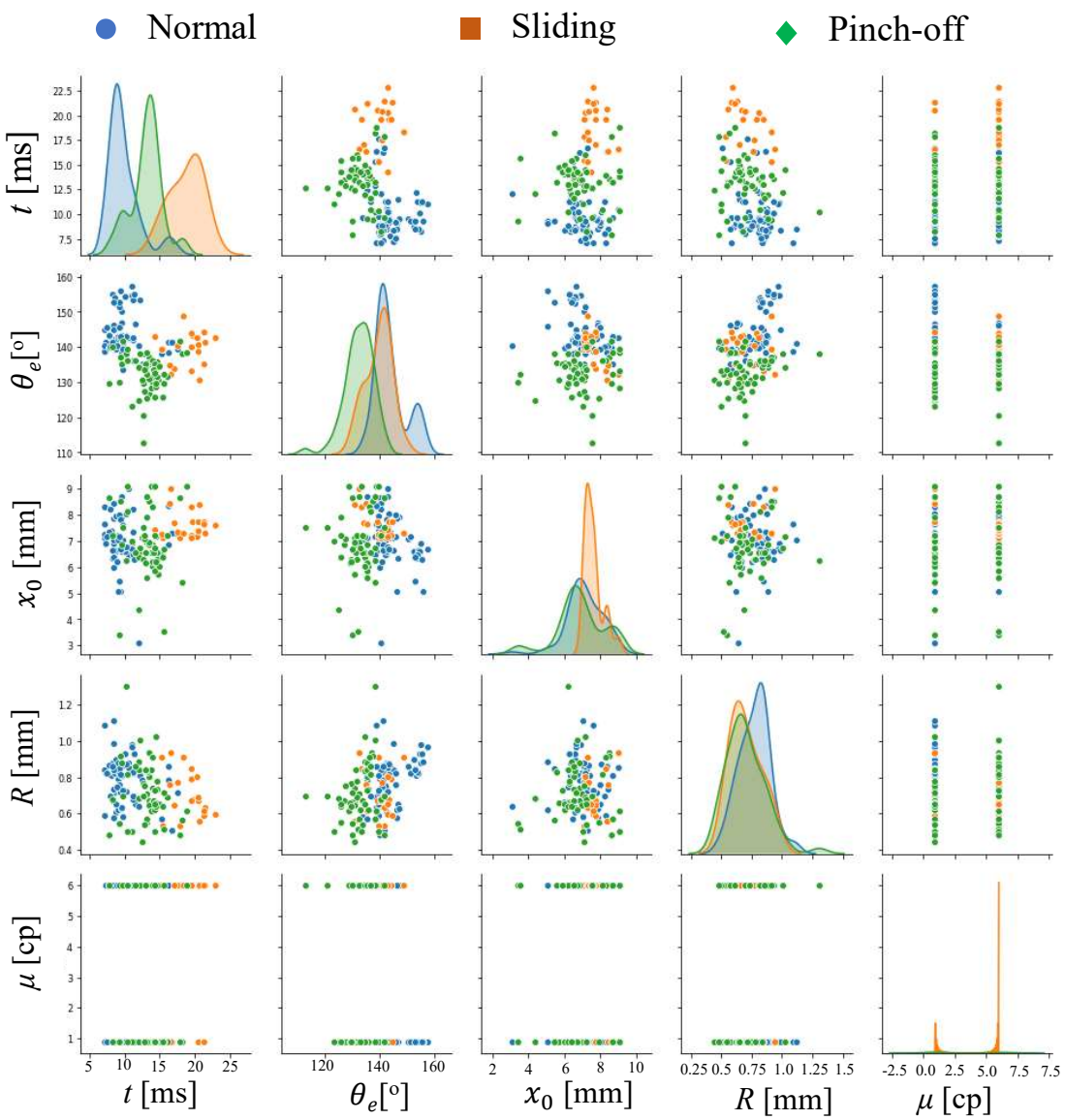

Figure 6.1: Pair plot of ejection modes. Plots along the diagonal are histograms.

The goal of the classification problem is to predict by which mode a drop will eject from the cantilever for a fixed set of system variables. Using 10-fold cross validation, we begin by splitting the data into 10 random and equal-sized subsamples. To predict drop ejection mode, four base learners are developed and include RFs, GBM, KNN, and SVM. Before forming an ensemble, we determine the optimum parameter settings for each classification algorithm using the grid search method to maximize accuracy [175, 176]. Optimum parameters for RF, GBM, KNN, and SVM classification

are presented in Figure 6.2a-d, respectively. We employ a bagging classifier to the dataset and see that it provides slightly better accuracy than the individual learners. Using 10-fold cross-validation, we evaluate the accuracy of the learning algorithms and obtain an accuracy of 85% which is only slightly higher than any of the individual classifiers (**Table 6.1**).

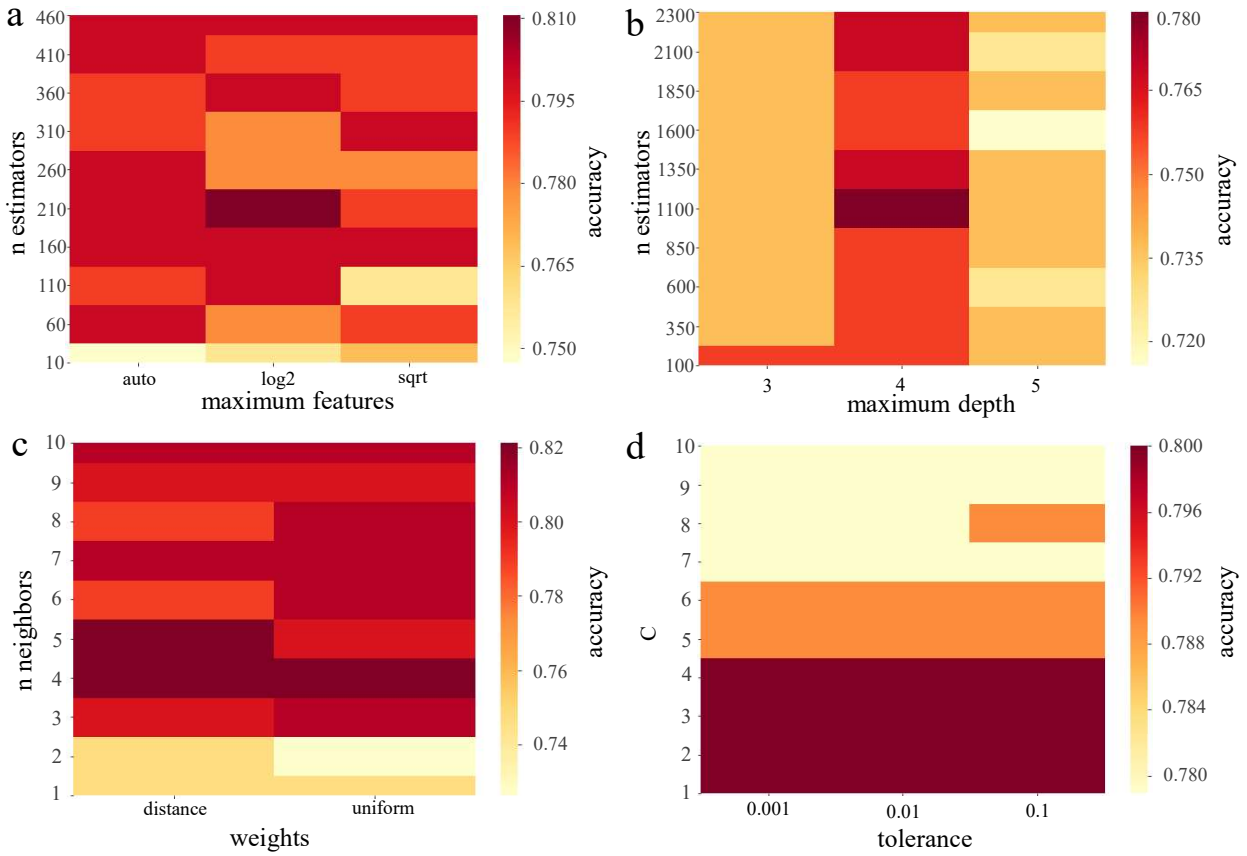

Figure 6.2: Optimum parameter settings for **(a)** RF, **(b)** GBM **(c)** KNN and **(d)** SVC algorithm.

We extend our analysis on ensemble learning for classification by analyzing the area under the curve (AUC) and the receiver operating characteristics (ROC) curve. To estimate the performance of a classification model, ROC-AUC is an effective classification matrix. ROC is a simple way to summarize the classification accuracy where a large number of confusion matrices are required to summarize the classification accuracy. The ROC curve summarizes all confusion matrices and the AUC represents separability, determining how the algorithm effectively differentiates between the classes. AUC-ROC curves of the ejection modes using bagging classification for our study are shown in Figure 6.3. Higher values of the AUC represent higher model performance for differen-

tiating ejection modes. A model ensures separability if the AUC has a value close to unity. If the ROC passes close to the random guess line, the algorithm is unable to separate different classes. Accuracy, precision, recall, and F-scores for all classification learners are given in Table 6.1.

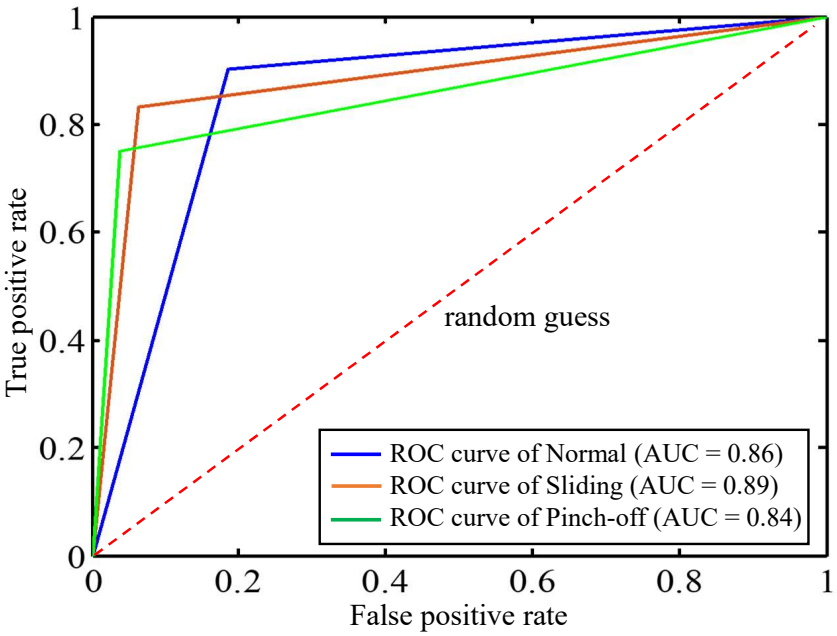

Figure 6.3: AUC-ROC curve of the bagging classifier.

Table 6.1: Performance of models in prediction of drop ejection modes.

Algorithm	**Accuracy**	**Precision**	**Recall**	**F-score**
RFs	0.83	0.84	0.80	0.82
GBM	0.78	0.78	0.75	0.76
KNN	0.83	0.82	0.79	0.80
SVC	0.80	0.79	0.79	0.79
Ensemble	0.85	0.84	0.82	0.83

The significance of system variables on ejection mode occurrence is computed using permutation feature importance [177], a method of measuring relative importance scores, independent of base learners. Feature importance is measured by the decrease of model accuracy obtained by shuffling a feature's value. Feature importance scores are plotted in Figure 6.4. For both classification of ejection modes (Figure 6.4a) and predicting ejection force through regression (Figure 6.4b), t and θ_e have higher importance scores than μ, x_0 and R. From the experiments we witness that if

$\theta_e \leqslant 136°$, drops are more likely to eject via the pinch-off mode [67]. Contact line motion begins rapidly, ≈ 6 ms from base motion inception, when drops are close to the cantilever tip as the inertial force at the tip rises quickly. Drops closer to the base require more time to eject. Feature importance scores likewise reveal the role of viscosity, which is a larger factor in determining the type of ejection than in the inertial force at ejection. F_{ad} is independent of μ (Eq.(5.2)), but does indirectly influence cohesive failure. Greater viscosity inhibits the drop elongation that creates favorable conditions for pinch-off, and thus greater viscosity promotes sliding from cantilevers undergoing large displacement.

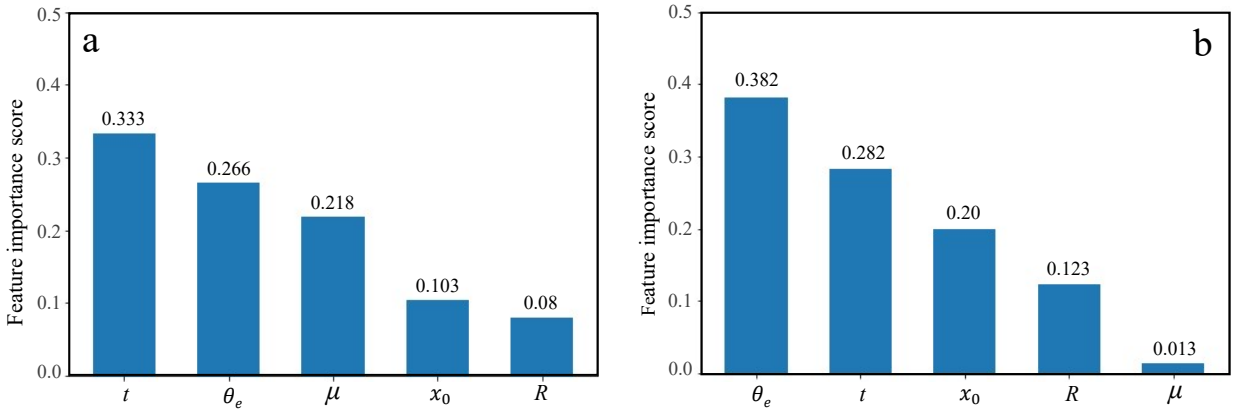

Figure 6.4: Variable importance scores for the predictive model of **(a)** drop ejection modes and **(b)** minimum inertial force required to eject a drop

6.2 Ensemble prediction of minimum inertial force required for drop ejection

Similar to the classification problem, before combining base learners into an ensemble, we determine the optimum parameters for each base learner using the grid search method shown in Figure 6.5a-d. To predict the minimum inertial force required to eject a drop, four regression models are trained with the of the total data set. Individual algorithms are RFs, GBM, RR, and SVR. Unlike classification, we use a grid search method to find the optimum parameter set that gives the minimum RMSE value. The application programming interface (API) always maximizes the score, so scores that need to be minimized are negative. Therefore, the optimization is done using negative

mean square error instead of mean squared error.

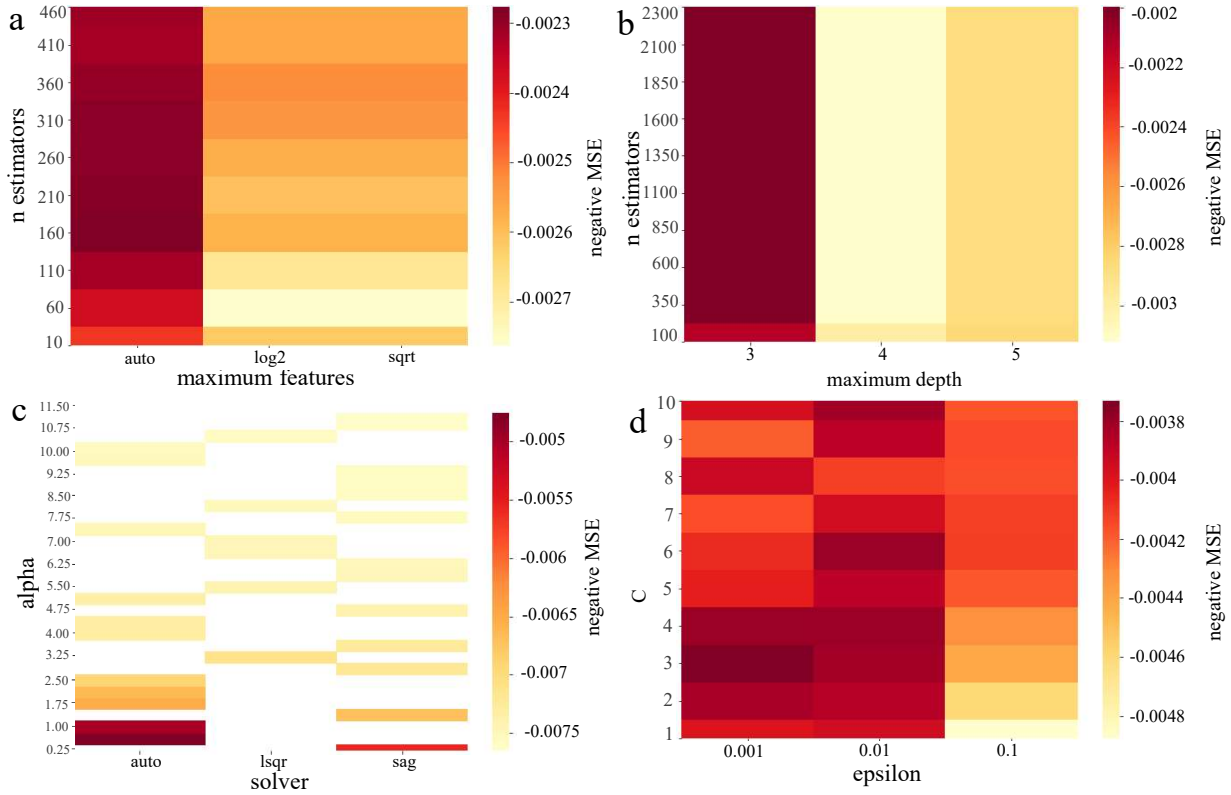

Figure 6.5: Optimum parameter for **(a)** RF, **(b)** GBM **(c)** RR and **(d)** SVR algorithm.

We train the predictive models to predict the minimum inertial force required to eject a drop and use 10-fold cross-validation to validate the performance of the models. The predicted versus actual inertial force for each base learner is plotted in Figure 6.6. RF and GBM outperform the others with low RMSE values, as shown in Table 6.2. The ensemble improves RMSE by 11.9% compared to the best base learner, GBM.

Table 6.2: Performance of the predictive model of minimum inertial force required to eject a drop

Algorithm	α	**RMSE**
RFs	0.3707	0.045
GBM	0.4051	0.042
RR	0.2059	0.070
SVR	0.0183	0.058
Ensemble	-	0.037

The weight assigned to each individual base learner is calculated by solving the NNLS problem

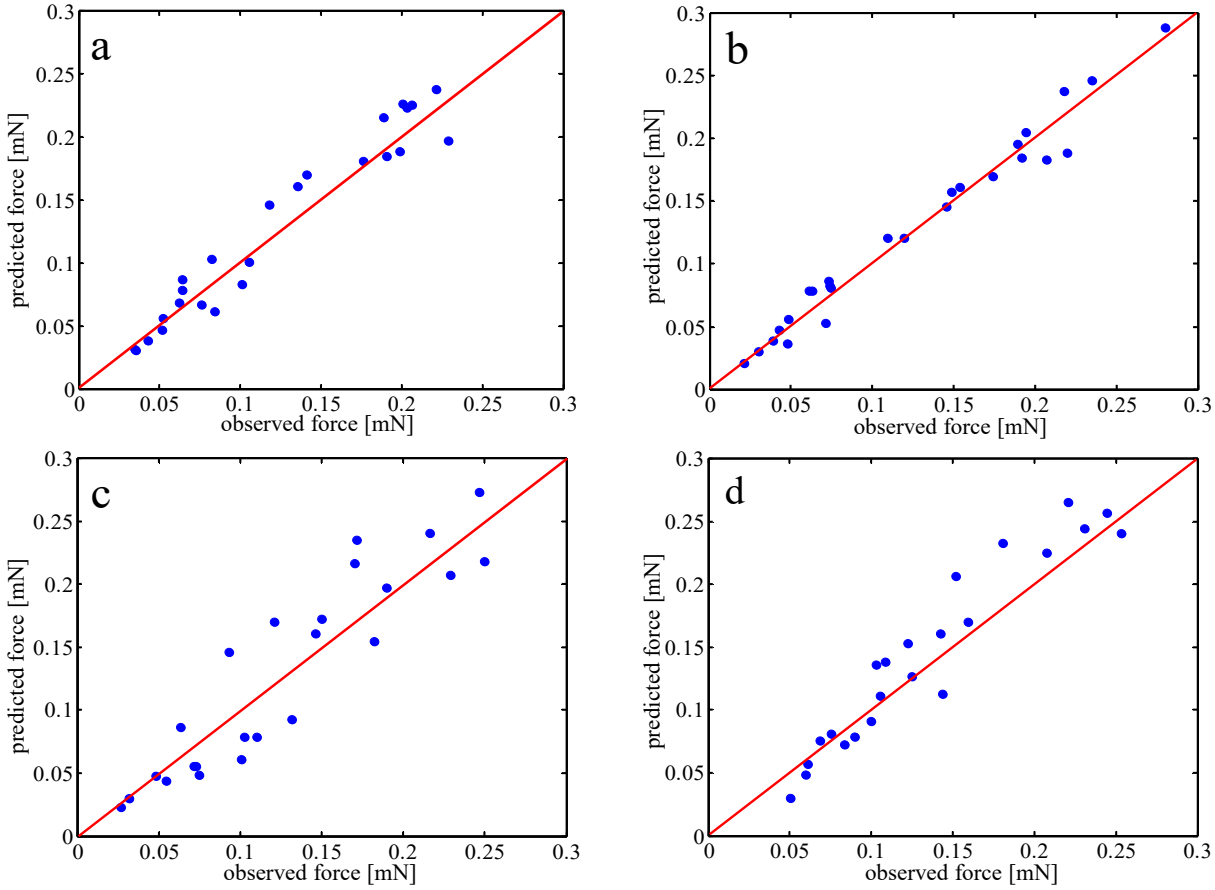

Figure 6.6: Observed versus predicted inertial force for **(a)** RF, **(b)** GBM **(c)** RR and **(d)** SVR algorithm.

described in §2.3 and given in Table 6.2. To visualize the performance of ensemble-based learning, we use Regression Error Characteristic (REC) curves with the individual learning algorithm simultaneously shown in Figure 6.7a. RECs plot the accuracy of the regression model with respect to the absolute deviation. The relative position of the REC curve reveals which model is superior compared to others. Models that reach 100% accuracy with a smaller value of error tolerance provide better predictions. In other words, models with the higher area under the curve have less error. Predicted inertial force versus the actual force generated from the ensemble learning model is shown in Figure 6.7b.

We plot the predicted inertial force F_{i} required to eject a drop from the cantilever surface versus equilibrium contact angle θ_{e} in Figure 6.8. Globally, larger drops require greater F_{i} to eject. In the complete liquid removal zone, the inertial force developed by the cantilever must overcome F_{ad}

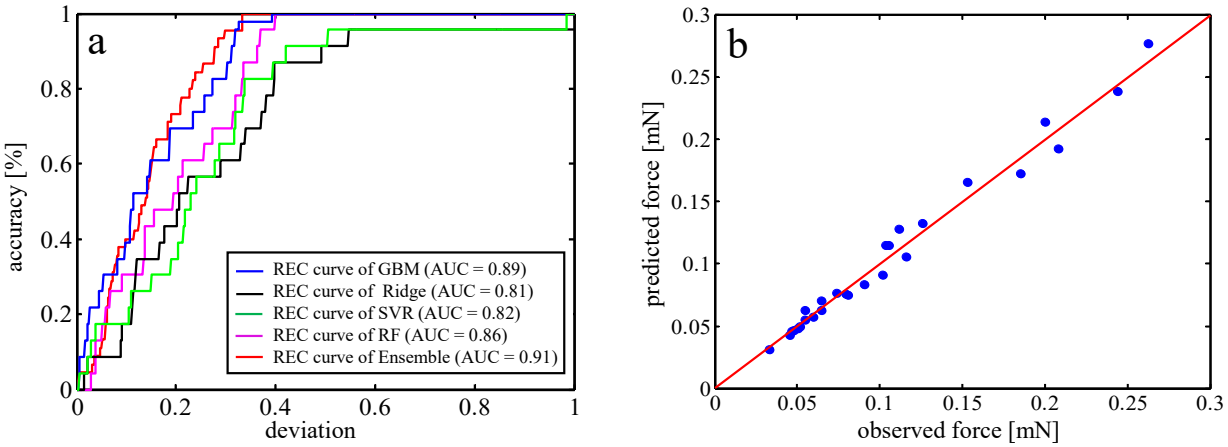

Figure 6.7: **(a)** REC curve to visualize the performance of regression models and **(b)** observed versus predicted inertial force for ensemble learning.

(Eq.(5.2)). However, in the partial liquid removal zone, drops need to overcome both F_{ad}, to get the contact line moving, and an as yet unquantified cohesive force F_{coh} to perform a pinch-off ejection. Partial liquid removal or pinch-off, is associated with lower θ_e and higher F_i. In the ensemble model, we fix drop position to the mean value of $\bar{x_0} = 7.2$ mm and vary drop size R to produce the inertial force predictions of Figure 6.8a,b. We rationalize the relation between F_i and θ_e in the partial liquid removal zone by noting that lower θ_e values promote flatter drops with centers of mass closer to the substrate, increasing the inertial force required to deform the drop into a shape that can pinch off. Such deformation necessitates a relatively long time history to slosh to an elongated shape which can eject, a notion supported by Figure 6.4b. The relative values of F_i in the partial removal zone for different drop radii likewise provide insight to the value of F_{coh}, for which there is no theoretical measure. Indeed, $F_{coh} \not\propto R$, but this prediction verifies larger drops carry higher cohesive forces.

Next, we fix drop radius $\bar{R} = 0.75$ mm to predict F_i for various drop locations. For a fixed drop radius, inertial force in the partial liquid removal zone is greater for drops closer to the cantilever tip. At the tip, inertia forces temporally increase most rapidly at the onset of base vibration. Toward the base, the ejection inertial forces are unrealized for a relatively long period of time, over which the cantilever imparts a time-history of deformation to the drop. We thus surmise that drops ejected

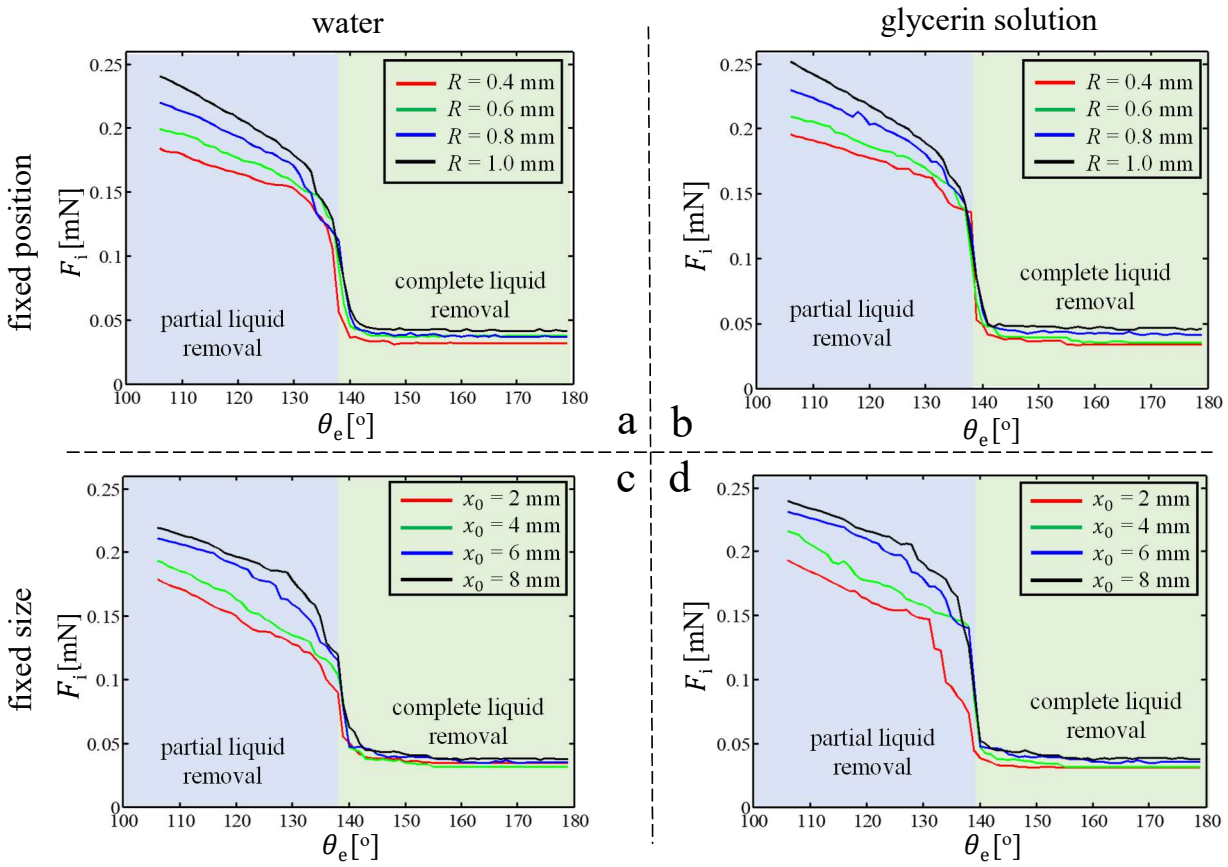

Figure 6.8: Prediction of inertial force for water (a,c) and 1:1 water-glycerin solution (b,d), for fixed drop location (a,b) and fixed drop size, (c,d).

closer to the base have reached a state of enhanced deformation by being allowed to slosh for more vibration cycles; drop elongation decreases F_{coh}. Predictions of F_i in all panels of Figure 6.8 show a rapid change from the zone of partial to complete liquid removal where inertial force is independent of drop location, as expected by observation of Eq.(5.2). Above $\theta_e = 138°$ we witness no pinch-off ejections, which agrees with our previous prediction of the transition contact angle [67]. Curves in Figure 6.8 extrapolate to contact angles beyond our highest measured value of 155°. Physically, we expect $F_i \to 0$ as $\theta_e \to 180°$, but note our cantilever is not capable of producing F_i lower than 0.03 mN when drops finally leave the surface.

By changing R and x_0 in our model, we predict changes to F_i but are unable to move from one removal zone to another, a characteristic of Figure 6.8 that supports our analysis of feature impor-

tance scores (Figure 6.4b). Though not captured in our plots, we posit complete liquid removal closer to the base requires longer ejection times at a fixed θ_e. Though θ_e is not fixed in Figure 6.1, the plot of t versus x_0 shows complete removal is more rapid than partial removal. Sliding, though complete removal, takes the longest ejection duration because the drop must travel $x_0 + R$ to leave the substrate.

6.3 Discussion

This work investigates the fundamental fluid-structure interactions of a system that exhibits highly-coupled fluid and solid mechanics. The complex behavior of such exceedingly nonlinear systems of soft materials warrants foundational studies that employ simple experimental systems. We therefore choose drops deforming freely vibrating cantilevers, which provide easily observed fluid deformation and planar solid motion. The temporal kinematics of drop-cum-substrate motion are complex because drops can deform, often out-of-phase with beams. We show drops damp beam vibration by comparing displacement curves to that of solid masses. The damping imparted to the beam is dependent upon drop properties such as size, viscosity, and surface tension. Drops in our system are analogous to particle impact dampers studied previously but exhibit more complex behavior and damp at much lower vibration amplitude. We develop an ensemble learning algorithm to classify drop ejection modes and predict the minimum inertial force required to remove water drops and drops of glycerin solution from a dampened, damped cantilever. The ensemble model predicts the ejection modes with an accuracy of 85%. In the prediction of inertial force at ejection, a regression problem, tree-based learning algorithms show better performance over kernel- and regularization-based algorithms. The ensemble improves RMSE by 11.9% over the best individual base learner, gradient boosting. Algorithmic predictions reveal inertial force variation model that shows clear indication of two

CHAPTER 7: CONCLUSION

We explore the vibration damping characteristics of singular liquid drops of varying viscosity and surface tension resting on a millimetric cantilever. Cantilevers are displaced 0.6 mm and their free end and allows to vibrate freely. Cantilever vibration causes drops to deform, or slosh, which dissipates kinetic energy via viscous dissipation within the drop. Damping by drop sloshing is dependent on viscosity, surface tension, drop size, and drop location. A solid weight with the same mass as experimental drops is used to compare the damping imposed by liquids, thereby accounting for other damping sources. Neither the most viscous nor least viscous drops studied imposed the greatest damping on cantilever motion. Instead, drops of intermediate viscosity strike the most effective balance of sloshing and internal dissipative capacity. Very thin cantilevers with sloshing drops express more than one dominant frequency and vibrate erratically, often shifting phase, and presenting a challenge for quantification of damping. Finally, we introduce a new dimensionless group aimed at incorporating all salient variables of our cantilever-drop system.

We identify three ejection modes for singular drops from elastic, millimetric scale cantilevers with an excited base, and classify these ejections as sliding, normal-to-substrate, and pinch-off. The occurrence of a particular ejection depends on drop properties, cantilever motion, and cantilever wetting properties. Drops slide from the cantilever tip for equilibrium contact angles above approximately 135° and when the tangential component of the inertial force exceeds adhesion forces which resist sliding, requiring cantilever deflection angles greater than 18°. Normal-to-substrate ejection also occurs for equilibrium contact angles above approximately 135°, but favors smaller cantilever deflection. During pinch-off, a portion of the adhered drop is flung from the cantilever while another portion is left attached. The magnitude of ejected mass from pinch-off ejections is well-predicted by a modification to Tate's Law. Below an equilibrium contact angle of approximately 135°, pinch-off is the only possible ejection mode in our system. A dynamic model of beam motion derived from elastica theory permits the quantification of drop damping on system mo-

tion. Lower equilibrium contact angles producing pinch-off ejection experience greater damping by drops than those in the normal-to-substrate ejection regime.

We develop an ensemble learning algorithm to classify drop ejection modes and predict the minimum inertial force required to remove water drops and drops of glycerin solution from a dampened, damped cantilever. The ensemble model predicts the ejection modes with an accuracy of 85%, which is not a vast improvement over the individual base learners. With the data-driven predictive modeling approach, we identify the importance of system variables–ejection time, contact angle, drop size, and drop location–on ejection mode occurrence the associated inertial force at ejection. Ejection time and contact angle are the dominant features for predicting both ejection modes and inertial force. In the prediction of inertial force at ejection, a regression problem, tree-based learning algorithms show better performance over kernel and regularization-based algorithms. The ensemble improves RMSE by 11.9% over the best individual base learner, gradient boosting. Algorithmic predictions reveal that in the zone of partial liquid removal or pinch-off, drop size and location governs ejection inertial force, whereas inertial force in the zone of complete liquid removal is independent of drop size and location.

APPENDIX A: ADDITIONAL VIDEOS AND FIGURES

A.1 Damping by Drop Sloshing

A.1.1 Supplementary movie captions

Movie S1: Experimental compilation of 10-mil thick cantilever topped by the gamut of experimental liquid drops. Slowed 270×.

Movie S2: Experimental compilation of 5-mil thick cantilever topped by the gamut of experimental liquid drops. Slowed 270×.

Movie S3: Experimental compilation of 2-mil thick cantilever topped by the gamut of experimental liquid drops. Slowed 270×.

A.1.2 Supplementary Figures

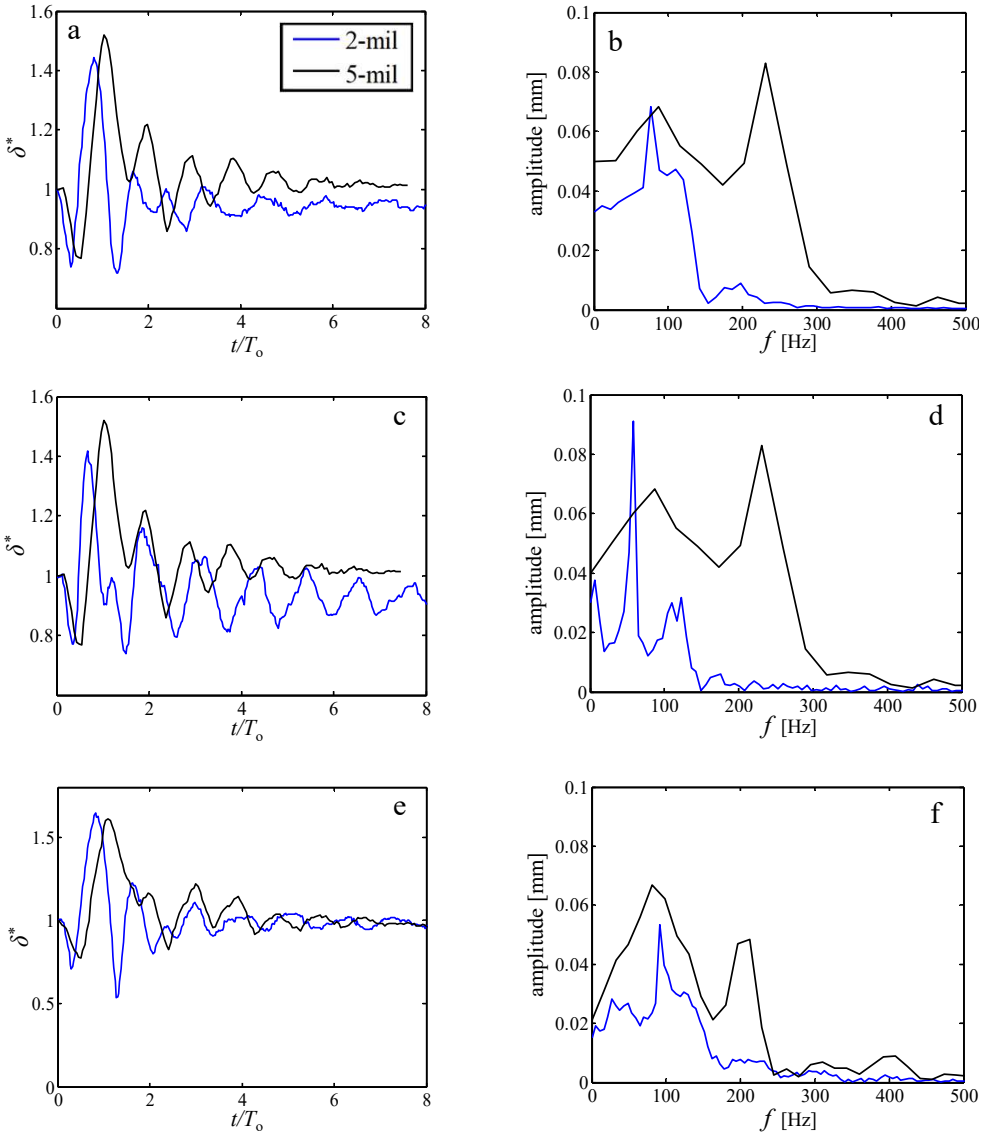

Figure A.1: Time response **(a-c)** and frequency response **(b-f)** of flatness factor with G3W1 drop with surface tension $\sigma = 78.4$ mN/m (a,b), $\sigma = 69.3$ mN/m (c,d) and $\sigma = 55.8$ mN/m (e,f).

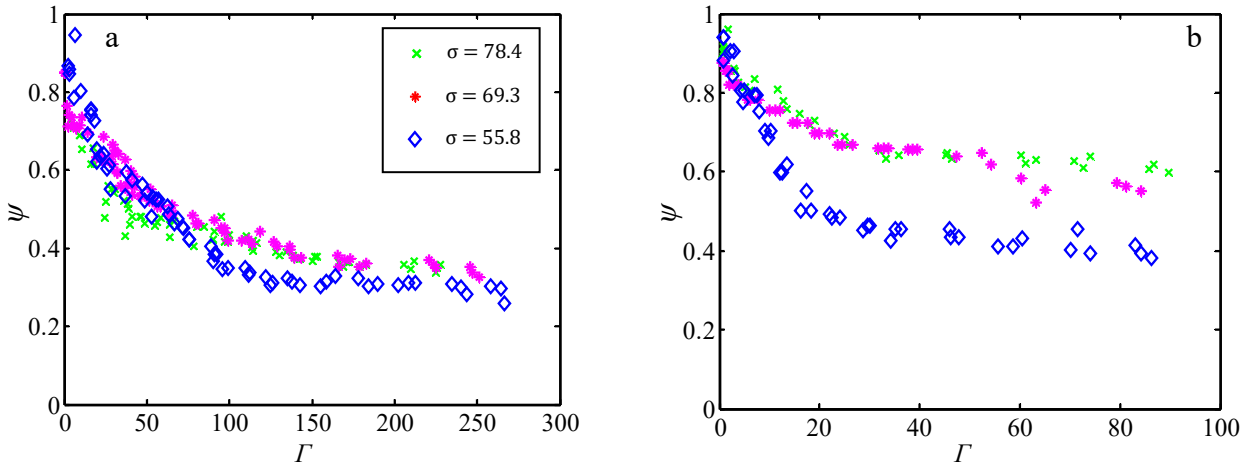

Figure A.2: Specific damping capacity ψ versus effective acceleration Γ for a G3W1 drop atop a **(a)** 10-mil and **(b)** 5-mil cantilever.

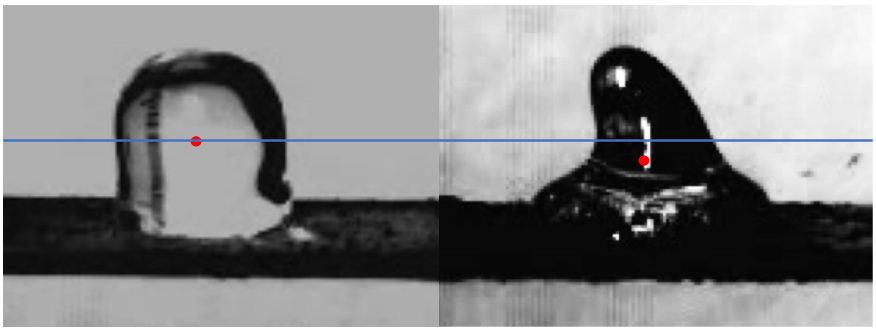

Figure A.3: Center of mass (red dot) for G3W1 drops and maximum δ^* with surface tension tension 78.4 mN/m (left) and 55.8 mN/m (right).The drop centroid was determined with ImageJ.

A.2 Drop Ejection

A.2.1 Droplet volume calculation

The droplet radius, $R(h)$ shown in Figure A.5, which is dependent on the height, h, can be described at an arbitrary height by [161]:

$$R(h) = \sqrt{R^2 - (h - R\cos\theta_e)^2}. \tag{A.1}$$

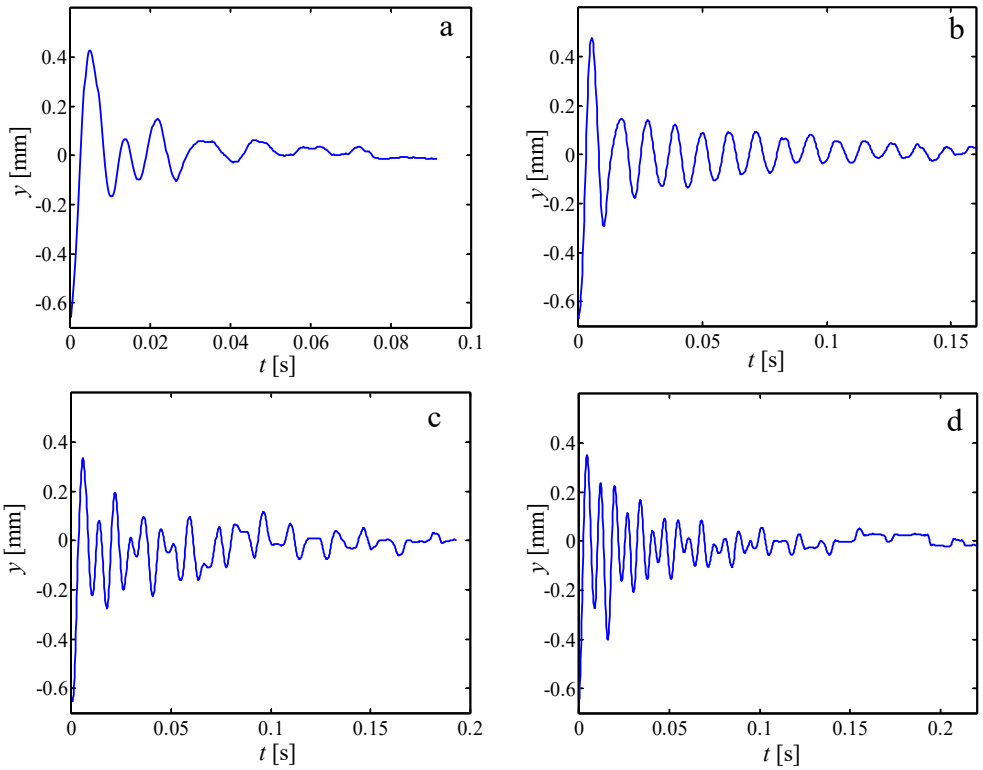

Figure A.4: Temporal displacement curves of 2-mil cantilever topped by **(a)** G3W1, **(b)** G1W1, **(c)** G1W3 and **(d)** W1 drops.

The volume of a droplet with equilibrium contact angle θ_e can be calculated as follows:

$$V = \frac{4}{3}\pi R^3 - \int_0^{2R-H} \pi R(h)^2 dh. \tag{A.2}$$

Representing the upper limit of the integration, $h' = 2R - H$,

$$V = \pi \left[\frac{4}{3}R^3 - R^2 h' + \frac{(h')^2}{3} - (h')^2 \cos\theta_e + R^2 h' \cos^2\theta_e \right]. \tag{A.3}$$

A.2.2 Supplementary Movie Captions

Movie S4: Sliding ejection mode. A mobile drop slides from its initial position to the end of the cantilever, and leaves no portion of itself on the substrate.

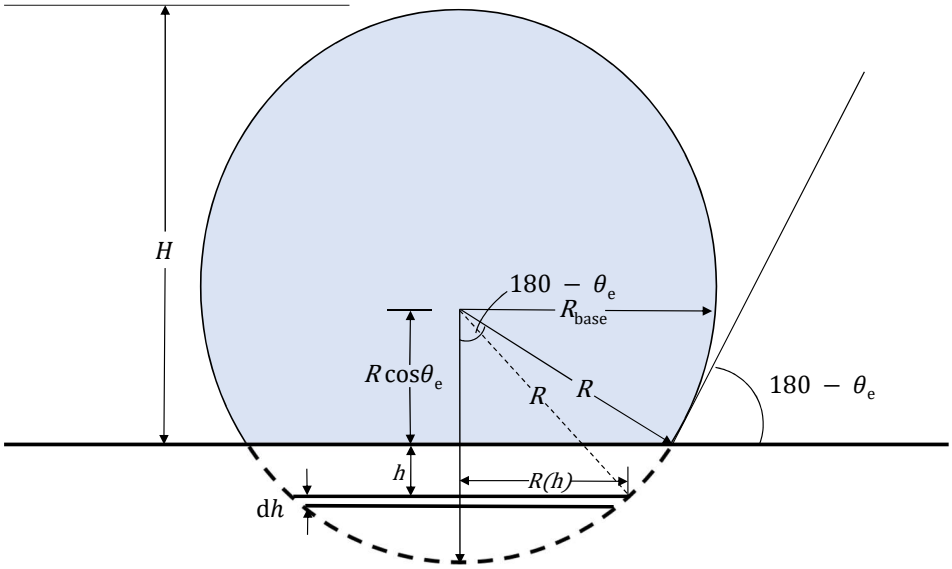

Figure A.5: Geometric description for calculating the volume of a drop resting on a flat surface.

Movie S5: Normal-to-substrate ejection. A drop ejects without sliding from its original position, with nearly symmetrical contact line motion, and leaves no portion of itself on the substrate.

Movie S6: Pinch-off ejections. A portion of the drop ejects in cohesive failure while a portion of the drop remains attached to the substrate. The drop deforms to form a neck which closes in one of three ways: neck closure at the portion attached to the substrate, neck closure at the ejecting mass, and simultaneous closure at both liquid bodies.

Movie S7: Comparison of actual cantilever deflection to theoretical deflection simulated and animated with MATLAB. Axes in the simulated motion have units of meters (m).

A.2.3 Supplementary Figures

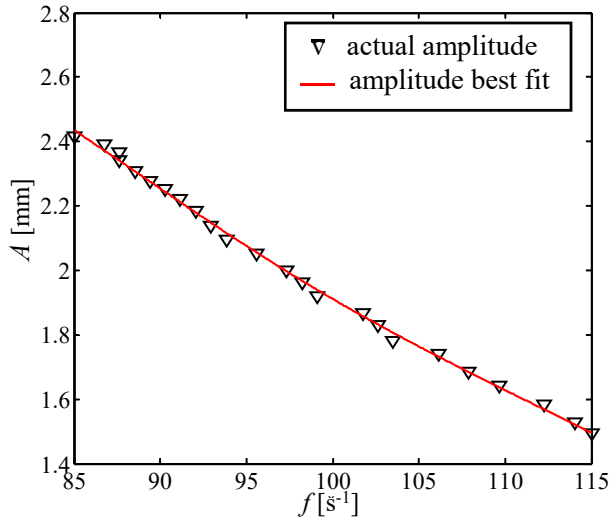

Figure A.6: Shaker base amplitude across the range of experimental vibration frequency.

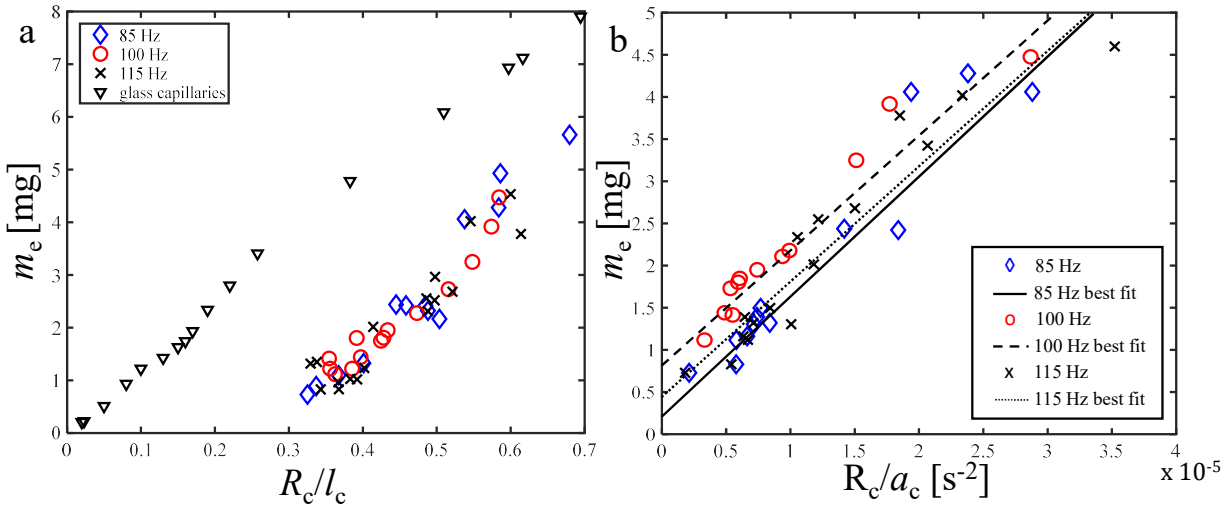

Figure A.7: Drop release via pinch-off. (a) The dependence of released mass and the size of the drop. The mass of drops dripping from glass capillaries is shown for comparison [2]. (b) The relation between drop mass and cantilever acceleration of drop release. Best fits in (b) are given by **Eq.7** (main text) using $F(R_c, x_o, \theta_e)$ 0.34, 0.29, and 0.30 for 85 Hz, 100 Hz, and 115 Hz respectively.

A.3 Predictive modeling of drop ejection from damped, dampened wings by machine learning

A.3.1 Supplementary description of chosen base learners

RFs is a decision tree-based algorithm with many ($O(10^2)$ in our study) independent decision trees working in concert and promoting randomness [178, 179]. While splitting into a new tree, RFs focus on finding the best features between a random subset of features.

GBM, similar to RFs, is a decision tree-based algorithm that trains each tree in a gradual, adaptive and sequential manner [37, 180]. GBM uses a loss function to determine model performance against training data and performs internal, iterative updates [181, 182].

KNN is a simple, supervised machine learning algorithm, which assumes similar outcomes (ejection modes in our case) stay close to one another and makes boundaries for each outcome [183, 184].

SVM, similar to KNN, creates boundaries between outcomes known as hyperplanes [185, 135]. SVM is a kernel based learning technique that maps the training data (ejection mode) to system variables[186]. **RR** uses L2 regularization where system variable inputs are shrunk by an estimator [187] while ensuring there is no elimination of a variable.

To boost the performance of predictive modeling, we employ an ensemble learning technique that combines four base learners. The benefit of using ensemble learning is that it usually outperforms its constituent base learners, adds robustness, and determines the most suitable base learner for a particular problem[188, 189, 190, 3].

A.3.2 Supplementary Figures

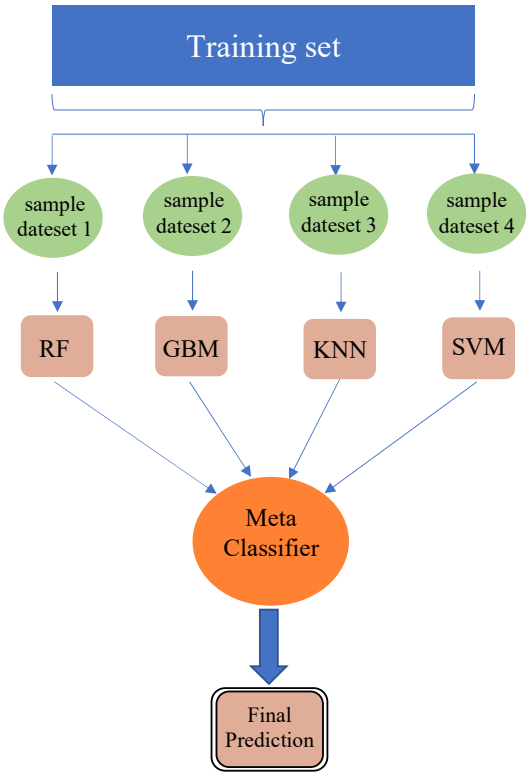

Figure A.8: Computational framework of bagging classifier.

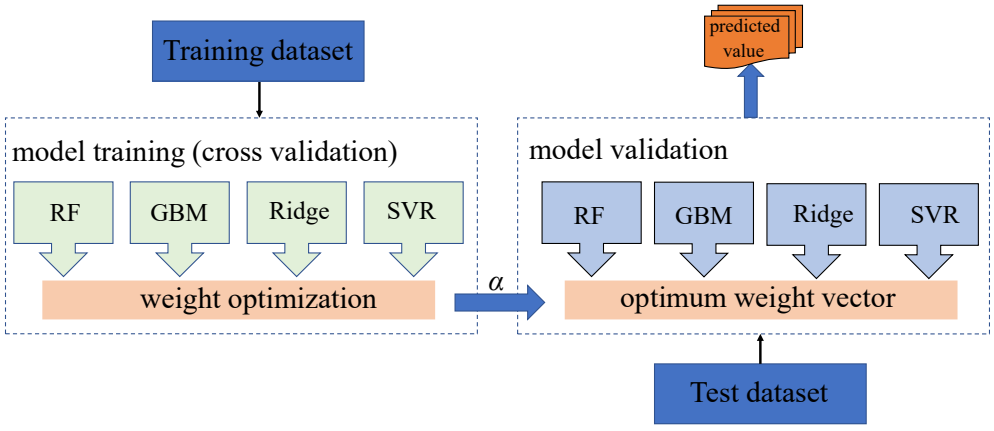

Figure A.9: Computational framework of ensemble learning for inertial force prediction[3].

APPENDIX B: PUBLICATIONS AND PRESENTATIONS

Journal papers

Alam, Md Erfanul, and Andrew Dickerson. "Sessile liquid drops damp vibrating structures" Physics of Fluids (2021).

Alam, Md Erfanul, Dazhong Wu, and Andrew Dickerson. "Predictive modelling of drop ejection from damped, dampened wings by machine learning" Proceeding of Royal Society A (2020).

Alam, Md Erfanul, Jeffrey L. Kauffman, and Andrew Dickerson. "Drop ejection from vibrating damped, dampened wings." Soft Matter (2020).

Presentations

Georgia Institute of Technology. Department of Mechanical Engineering. The coupled mechanics of drop release from elastic substrates, ME 8863. Fluid Mechanics.

American Physical Society's Division of Fluid Dynamics (DFD) 2018, To eject a droplet from a dampened, damped beam

University of Central Florida.Student Scholar Symposium. Sessile liquid drops damp vibrating structures.

APPENDIX C: VITA

Md Erfanul Alam was born on June 1, 1991, and spent his first 10 years of life in B. N. School and 2 years of college in Hazi Muhammad Mohsin College. He enrolled at Bangladesh University of Engineering and Technology where he completed his B.S in Mechanical Engineering. Having great research interest in mechatronics and control system he enrolled in Georgia Southern University where he completed his Master's degree with summa cum laude award. Md Erfanul Alam enrolled at the University of Central Florida, Orlando, Florida after being awarded the prestigious ORC Fellowship, in 2017. On June 4, 2021, he successfully defended his Ph.D. in Mechanical Engineering from the Fluids and Structures (FaST) Laboratory at the University of Central Florida.

LIST OF REFERENCES

[1] Dickerson, A. K. & Hu, D. L., 2014 Mosquitoes actively remove drops deposited by fog and dew. *Integrative and Comparative Biology* pp. 1–6.

[2] Harkins, W. & Brown, F., 1919 The determination of surface tension (free surface energy), and the weight of falling drops: the surface tension of water and benzene by the capillary height method. *Journal of the American Chemical Society* **41**, 499–524. ISSN 0002-7863.

[3] Wu, D. & Xu, C., 2018 Predictive modeling of droplet formation processes in inkjet-based bioprinting. *Journal of Manufacturing Science and Engineering* **140**.

[4] Saska, M., Vonásek, V., Chudoba, J., Thomas, J., Loianno, G. & Kumar, V., 2016 Swarm distribution and deployment for cooperative surveillance by micro-aerial vehicles. *Journal of Intelligent & Robotic Systems* **84**, 469–492.

[5] Schenato, L., Campolo, D. & Sastry, S., 2003 Controllability issues in flapping flight for biomimetic micro aerial vehicles (mavs). In *42nd IEEE International Conference on Decision and Control (IEEE Cat. No. 03CH37475)*, volume 6, pp. 6441–6447. IEEE.

[6] Brambilla, M., Ferrante, E., Birattari, M. & Dorigo, M., 2013 Swarm robotics: a review from the swarm engineering perspective. *Swarm Intelligence* **7**, 1–41.

[7] Şahin, E., 2004 Swarm robotics: From sources of inspiration to domains of application. In *International workshop on swarm robotics*, pp. 10–20. Springer.

[8] Wang, Z. J., 2005 Dissecting insect flight. *Annual Reviews in Fluid Mechanics* **37**, 183–210.

[9] Dudley, R. & Ellington, C., 1990 Mechanics of forward flight in bumblebees: I. Kinematics and morphology. *Journal of Experimental Biology* **148**, 19–52.

[10] Bomphrey, R. J., Nakata, T., Phillips, N. & Walker, S. M., 2017 Smart wing rotation and trailing-edge vortices enable high frequency mosquito flight. *Nature* **544**, 92–95. ISSN 0028-0836.

[11] Bomphrey, R. J., Nakata, T., Henningsson, P. & Lin, H.-T., 2016 Flight of the dragonflies and damselflies. *Phil. Trans. R. Soc. B* **371**, 20150389. ISSN 0962-8436.

[12] Dickinson, M. H., Lehmann, F.-O. & Sane, S. P., 1999 Wing rotation and the aerodynamic basis of insect flight. *Science* **284**, 1954–1960.

[13] Bleischwitz, R., de Kat, R. & Ganapathisubramani, B., 2016 Aeromechanics of membrane and rigid wings in and out of ground-effect at moderate reynolds numbers. *Journal of Fluids and Structures* **62**, 318 – 331. ISSN 0889-9746. (doi:https://doi.org/10.1016/j.jfluidstructs.2016.02.005).

[14] Nakata, T. & Liu, H., 2011 Aerodynamic performance of a hovering hawkmoth with flexible wings: a computational approach. *Proceedings of the Royal Society of London B: Biological Sciences* .

[15] Zhao, L., Huang, Q., Deng, X. & Sane, S., 2010 Aerodynamic effects of flexibility in flapping wings. *Journal of The Royal Society Interface* **7**, 485.

[16] Masoud, H. & Alexeev, A., 2010 Resonance of flexible flapping wings at low reynolds number. *Physical Review E* **81**, 056304.

[17] Shang, J., Combes, S., Finio, B. & Wood, R., 2009 Artificial insect wings of diverse morphology for flapping-wing micro air vehicles. *Bioinspiration & Biomimetics* **4**, 1–6.

[18] Combes, S. & Daniel, T., 2003 Flexural stiffness in insect wings ii. spatial distribution and dynamic wing bending. *Journal of Experimental Biology* **206**, 2989–2997.

[19] Wootton, R. J., 1992 Functional morphology of insect wings. *Annual Review of Entomology* **37**, 113–140.

[20] Richter, C. & Lipson, H., 2011 Untethered hovering flapping flight of a 3D-printed mechanical insect. *Artificial Life* **17**, 73–86.

[21] Dickerson, A. K., Shankles, P. G. & Hu, D. L., 2014 Raindrops push and splash flying insects. *Physics of Fluids* **26**, 027104.

[22] Dickerson, A. K., Shankles, P. G., Berry, B. E. & Hu, D. L., 2015 Fog and dense gas disrupt mosquito flight due to increased aerodynamic drag on halteres. *Journal of Fluids and Structures* **55**, 451–462.

[23] Byun, D., Hong, J., Ko, J. H., Lee, Y. J., Park, H. C., Byun, B.-K., Lukes, J. R. *et al.*, 2009 Wetting characteristics of insect wing surfaces. *Journal of Bionic Engineering* **6**, 63–70.

[24] White, B., Sarkar, A. & Kietzig, A.-M., 2013 Fog-harvesting inspired by the stenocara beetle—an analysis of drop collection and removal from biomimetic samples with wetting contrast. *Applied Surface Science* **284**, 826–836.

[25] Taylor, G. K. & Krapp, H. G., 2007 Sensory systems and flight stability: what do insects measure and why? *Advances in insect physiology* **34**, 231–316.

[26] Ma, Z. S. & Krings, A. W., 2009 Insect sensory systems inspired computing and communications. *Ad Hoc Networks* **7**, 742–755.

[27] Liu, C., Ju, J., Zheng, Y. & Jiang, L., 2014 Asymmetric ratchet effect for directional transport of fog drops on static and dynamic butterfly wings. *ACS nano* **8**, 1321–1329.

[28] Kimber, M., Lonergan, R. & Garimella, S., 2009 Experimental study of aerodynamic damping in arrays of vibrating cantilevers. *Journal of Fluids and Structures* **25**, 1334–1347.

[29] Bidkar, R. A., Kimber, M., Raman, A., Bajaj, A. K. & Garimella, S. V., 2009 Nonlinear aerodynamic damping of sharp-edged flexible beams oscillating at low keulegan–carpenter numbers. *Journal of Fluid Mechanics* **634**, 269–289.

[30] Valamanesh, V. & Myers, A., 2014 Aerodynamic damping and seismic response of horizontal axis wind turbine towers. *Journal of Structural Engineering* **140**, 04014090.

[31] Yang, J., Ono, T. & Esashi, M., 2002 Energy dissipation in submicrometer thick single-crystal silicon cantilevers. *Journal of Microelectromechanical Systems* **11**, 775–783.

[32] Hosaka, H., Itao, K. & Kuroda, S., 1994 Evaluation of energy dissipation mechanisms in vibrational microactuators. In *Proceedings IEEE Micro Electro Mechanical Systems An Investigation of Micro Structures, Sensors, Actuators, Machines and Robotic Systems*, pp. 193–198. IEEE.

[33] Yasumura, K. Y., Stowe, T. D., Chow, E. M., Pfafman, T., Kenny, T. W., Stipe, B. C. & Rugar, D., 2000 Quality factors in micron-and submicron-thick cantilevers. *Journal of Microelectromechanical Systems* **9**, 117–125.

[34] Baker, W. E., Woolam, W. E. & Young, D., 1967 Air and internal damping of thin cantilever beams. *International Journal of Mechanical Sciences* **9**, 743–766.

[35] Papalou, A. & Masri, S., 1996 Response of impact dampers with granular materials under random excitation. *Earthquake Engineering & Structural Dynamics* **25**, 253–267. (doi: 10.1002/(SICI)1096-9845(199603)25:3<253::AID-EQE553>3.0.CO;2-4).

[36] Xu, Z., Wang, M. Y. & Chen, T., 2005 Particle damping for passive vibration suppression: numerical modelling and experimental investigation. *Journal of Sound and Vibration* **279**, 1097–1120. (doi:10.1016/j.jsv.2003.11.023).

[37] Friend, R. D. & Kinra, V. K., 2000 Particle impact damping. *Journal of Sound and Vibration* **233**, 93–118. (doi:10.1006/jsvi.1999.2795).

[38] Duncan, M., Wassgren, C. & Krousgrill, C., 2005 The damping performance of a single particle impact damper. *Journal of Sound and Vibration* **286**, 123–144.

[39] Friend, R. D. & Kinra, V., 2000 Particle impact damping. *Journal of Sound and Vibration* **233**, 93–118.

[40] Mao, K., Wang, M. Y., Xu, Z. & Chen, T., 2004 Simulation and characterization of particle damping in transient vibrations. *Journal of Vibration and Acoustics* **126**, 202–211.

[41] Xu, Z., Wang, M. Y. & Chen, T., 2005 Particle damping for passive vibration suppression: numerical modelling and experimental investigation. *Journal of Sound and Vibration* **279**, 1097–1120.

[42] Olson, S. E., 2003 An analytical particle damping model. *Journal of Sound and Vibration* **264**, 1155–1166.

[43] Lu, Z., Wang, Z., Masri, S. F. & Lu, X., 2018 Particle impact dampers: Past, present, and future. *Structural Control and Health Monitoring* **25**, e2058.

[44] Saeki, M., 2002 Impact damping with granular materials in a horizontally vibrating system. *Journal of Sound and Vibration* **251**, 153–161.

[45] Wong, C., Daniel, M. & Rongong, J., 2009 Energy dissipation prediction of particle dampers. *Journal of Sound and Vibration* **319**, 91–118.

[46] Michon, G., Almajid, A. & Aridon, G., 2013 Soft hollow particle damping identification in honeycomb structures. *Journal of Sound and Vibration* **332**, 536–544.

[47] Kempton, L., Pinson, D., Chew, S., Zulli, P. & Yu, A., 2012 Simulation of macroscopic deformation using a sub-particle dem approach. *Powder technology* **223**, 19–26.

[48] Ashley, S., 1995 A new racket shakes up tennis. *Mechanical Engineering-CIME* **117**, 80–82.

[49] Panossian, H., 1992 Structural damping enhancement via non-obstructive particle damping technique. *Journal of Vibration and Acoustics* **114**, 101–105.

[50] Ehrgott, R., Panossian, H. & Davis, G., 2009 Modeling techniques for evaluating the effectiveness of particle damping in turbomachinery. In *50th AIAA/ASME/ASCE/AHS/ASC Structures, Structural Dynamics, and Materials Conference 17th AIAA/ASME/AHS Adaptive Structures Conference 11th AIAA No*, p. 2690.

[51] Simonian, S. S., 1995 Particle beam damper. In *Smart Structures and Materials 1995: Passive Damping*, volume 2445, pp. 149–160. International Society for Optics and Photonics.

[52] Akyildiz, H. & Ünal, E., 2005 Experimental investigation of pressure distribution on a rectangular tank due to the liquid sloshing. *Ocean Engineering* **32**, 1503–1516.

[53] Eswaran, M. & Saha, U. K., 2011 Sloshing of liquids in partially filled tanks–a review of experimental investigations. *Ocean Systems Engineering* **1**, 131–155.

[54] Grotle, E. L. & Æsøy, V., 2017 Numerical simulations of sloshing and the thermodynamic response due to mixing. *Energies* **10**, 1338.

[55] Luskin, H. & Lapin, E., 1952 An analytical approach to the fuel sloshing and buffeting problems of aircraft. *Journal of the Aeronautical Sciences* **19**, 217–228.

[56] Caron, P., Cruchaga, M. & Larreteguy, A., 2018 Study of 3d sloshing in a vertical cylindrical tank. *Physics of Fluids* **30**, 082112.

[57] aus der Wiesche, S., 2005 Noise due to sloshing within automotive fuel tanks. *Forschung im Ingenieurwesen* **70**, 13–24.

[58] Frosina, E., Senatore, A., Andreozzi, A., Fortunato, F. & Giliberti, P., 2018 Experimental and numerical analyses of the sloshing in a fuel tank. *Energies* **11**, 682.

[59] He, R., Zhang, E. & Fan, B., 2019 Numerical analysis on the sloshing of free oil liquid surface under the variable conditions of vehicle. *Advances in Mechanical Engineering* **11**, 1687814019829967.

[60] Faltinsen, O., Firoozkoohi, R. & Timokha, A., 2011 Analytical modeling of liquid sloshing in a two-dimensional rectangular tank with a slat screen. *Journal of Engineering Mathematics* **70**, 93–109.

[61] Behruzi, P., Konopka, M., de Rose, F., Schwartz, G. *et al.*, 2014 Cryogenic slosh modeling in lng ship tanks and spacecrafts. In *The twenty-fourth international ocean and polar engineering conference*. International Society of Offshore and Polar Engineers.

[62] Ibrahim, R. A., 2005 *Liquid sloshing dynamics: theory and applications*. Cambridge University Press.

[63] Welt, F. & Modi, V., 1992 Vibration damping through liquid sloshing, part 2: Experimental results .

[64] Sauret, A., Boulogne, F., Cappello, J., Dressaire, E. & Stone, H. A., 2015 Damping of liquid sloshing by foams. *Physics of Fluids* **27**, 022103.

[65] Kannangara, D., Zhang, H. & Shen, W., 2006 Liquid–paper interactions during liquid drop impact and recoil on paper surfaces. *Colloids and Surfaces A: Physicochemical and Engineering Aspects* **280**, 203–215.

[66] Yang, X., Chhasatia, V. H. & Sun, Y., 2013 Oscillation and recoil of single and consecutively printed droplets. *Langmuir* **29**, 2185–2192.

[67] Alam, M. E., Kauffman, J. L. & Dickerson, A. K., 2020 Drop ejection from vibrating damped, dampened wings. *Soft Matter* **16**, 1931–1940.

[68] Tang, X., Saha, A., Sun, C. & Law, C. K., 2019 Spreading and oscillation dynamics of drop impacting liquid film. *Journal of Fluid Mechanics* **881**, 859–871.

[69] Zheng, J., Cheng, Y., Huang, Y., Wang, S., Liu, L. & Chen, G., 2020 Drop impacting on a surface with adjustable wettability based on the dielectrowetting effect. *Physics of Fluids* **32**, 097108.

[70] James, A., Vukasinovic, B., Smith, M. K. & Glezer, A., 2003 Vibration-induced drop atomization and bursting. *Journal of Fluid Mechanics* **476**, 1–28.

[71] Manglik, R. M., Jog, M. A., Gande, S. K. & Ravi, V., 2013 Damped harmonic system modeling of post-impact drop-spread dynamics on a hydrophobic surface. *Physics of Fluids* **25**, 082112.

[72] Alam, M. E., Wu, D. & Dickerson, A. K., 2020 Predictive modelling of drop ejection from damped, dampened wings by machine learning. *Proceedings of the Royal Society A* **476**, 20200467.

[73] Dickerson, A. K., Liu, X., Zhu, T. & Hu, D. L., 2015 Fog spontaneously folds mosquito wings. *Physics of Fluids* **27**, 021901.

[74] Dickerson, A. K., Shankles, P. G., Madhavan, N. M. & Hu, D. L., 2012 Mosquitoes survive raindrop collisions by virtue of their low mass. *Proceedings of the National Academy of Sciences* **109**, 9822–9827.

[75] Dickerson, A. K., Shankles, P. G., Berry, B. E. & Hu, D. L., 2015 Fog and dense gas disrupt mosquito flight due to increased aerodynamic drag on halteres. *Journal of Fluids and Structures* **55**, 451–462.

[76] Zanker, J. & Götz, K., 1990 The wing beat of drosophila melanogaster. ii. dynamics. *Philosophical Transactions of the Royal Society of London. B, Biological Sciences* **327**, 19–44.

[77] Lissaman, P. & Brown, G., 1993 Apparent mass effects on parafoil dynamics. In *Aerospace Design Conference*, p. 1236.

[78] Turner, C., 1982 Effect of store aerodynamics on wing/store flutter. *Journal of Aircraft* **19**, 574–580.

[79] Brunet, P., Baudoin, M., Matar, O. B. & Zoueshtiagh, F., 2010 Droplet displacements and oscillations induced by ultrasonic surface acoustic waves: a quantitative study. *Physical Review E* **81**, 036315.

[80] Snoeijer, J. H. & Andreotti, B., 2013 Moving contact lines: scales, regimes, and dynamical transitions. *Annual Review of Fluid Mechanics* **45**, 269–292.

[81] Dong, L., Chaudhury, A. & Chaudhury, M., 2006 Lateral vibration of a water drop and its motion on a vibrating surface. *The European Physical Journal E: Soft Matter and Biological Physics* **21**, 231–242.

[82] Brunet, P., Eggers, J. & Deegan, R., 2007 Vibration-induced climbing of drops. *Physical review letters* **99**, 144501.

[83] Noblin, X., Buguin, A. & Brochard-Wyart, F., 2004 Vibrated sessile drops: Transition between pinned and mobile contact line oscillations. *The European Physical Journal E: Soft Matter and Biological Physics* **14**, 395–404.

[84] Ding, H., Gilani, M. & Spelt, P., 2010 Sliding, pinch-off and detachment of a droplet on a wall in shear flow. *Journal of Fluid Mechanics* **644**, 217–244.

[85] Sharp, J. S., 2012 Resonant properties of sessile droplets; contact angle dependence of the resonant frequency and width in glycerol/water mixtures. *Soft Matter* **8**, 399–407.

[86] Semprebon, C. & Brinkmann, M., 2014 On the onset of motion of sliding drops. *Soft Matter* **10**, 3325–3334.

[87] Uijttewaal, W. & Nijhof, E., 1995 The motion of a droplet subjected to linear shear flow including the presence of a plane wall. *Journal of Fluid Mechanics* **302**, 45–63.

[88] Paulsen, J. D., Burton, J. C., Nagel, S. R., Appathurai, S., Harris, M. T. & Basaran, O. A., 2012 The inexorable resistance of inertia determines the initial regime of drop coalescence. *Proceedings of the National Academy of Sciences* **109**, 6857–6861.

[89] Roisman, I., Rioboo, R. & Tropea, C., 2002 Normal impact of a liquid drop on a dry surface: model for spreading and receding. *Proceedings of the Royal Society of London. Series A: Mathematical, Physical and Engineering Sciences* **458**, 1411. ISSN 1364-5021.

[90] Kinoshita, H., Kaneda, S., Fujii, T. & Oshima, M., 2007 Three-dimensional measurement and visualization of internal flow of a moving droplet using confocal micro-piv. *Lab on a Chip* **7**, 338–346.

[91] Yang, S.-A. & Chwang, A. T., 1992 About moving contact lines. *Journal of Engineering Mechanics* **118**, 735–745.

[92] Renardy, M., Renardy, Y. & Li, J., 2001 Numerical simulation of moving contact line problems using a volume-of-fluid method. *Journal of Computational Physics* **171**, 243–263.

[93] Shikhmurzaev, Y. D., 1993 The moving contact line on a smooth solid surface. *International Journal of Multiphase Flow* **19**, 589–610.

[94] Qian, T., Wang, X.-P. & Sheng, P., 2006 A variational approach to moving contact line hydrodynamics. *Journal of Fluid Mechanics* **564**, 333–360.

[95] Ramé, E. & Garoff, S., 1991 On identifying the appropriate boundary conditions at a moving contact line: an experimental investigation. *Journal of Fluid Mechanics* **230**, 97–116.

[96] Marsh, J. A. & Garoff, S., 1993 Dynamic contact angles and hydrodynamics near a moving contact line. *Physical Review Letters* **70**, 2778.

[97] Ren, W. & E, W., 2007 Boundary conditions for the moving contact line problem. *Physics of Fluids* **19**, 022101.

[98] Thiele, U., Neuffer, K., Bestehorn, M., Pomeau, Y. & Velarde, M. G., 2002 Sliding drops on an inclined plane. *Colloids and Surfaces A: Physicochemical and Engineering Aspects* **206**, 87–104.

[99] Chen, A. U., Notz, P. K. & Basaran, O. A., 2002 Computational and experimental analysis of pinch-off and scaling. *Physical review letters* **88**, 174501.

[100] Zhu, P., Tang, X., Tian, Y. & Wang, L., 2016 Pinch-off of microfluidic droplets with oscillatory velocity of inner phase flow. *Scientific reports* **6**, 31436.

[101] Egry, I., Giffard, H. & Schneider, S., 2005 The oscillating drop technique revisited. *Measurement Science and Technology* **16**, 426.

[102] Daniel, S., Sircar, S., Gliem, J. & Chaudhury, M. K., 2004 Ratcheting motion of liquid drops on gradient surfaces. *Langmuir* **20**, 4085–4092.

[103] Brunet, P., Eggers, J. & Deegan, R., 2009 Motion of a drop driven by substrate vibrations. *The European Physical Journal Special Topics* **166**, 11–14.

[104] Vukasinovic, B., Smith, M. & Glezer, A., 2007 Mechanisms of free-surface breakup in vibration-induced liquid atomization. *Physics of Fluids* **19**, 012104.

[105] Gart, S., Mates, J. E., Megaridis, C. M. & Jung, S., 2015 Droplet impacting a cantilever: A leaf-raindrop system. *Physical Review Applied* **3**, 044019.

[106] Whitaker, D., Kim, C., Vicente, C., Weilert, M., Maris, H. & Seidel, G., 1998 Shape oscillations in levitated he ii drops. *Journal of low temperature physics* **113**, 491–499.

[107] Thoroddsen, S., Etoh, T. & Takehara, K., 2007 Experiments on bubble pinch-off. *Physics of Fluids* **19**, 042101.

[108] Zhang, K., Liu, F., Williams, A. J., Qu, X., Feng, J. J. & Chen, C.-H., 2015 Self-propelled droplet removal from hydrophobic fiber-based coalescers. *Physical review letters* **115**, 074502.

[109] Pollard, A., Castillo, L., Danaila, L. & Glauser, M., 2016 *Whither turbulence and big data in the 21st century?* Springer.

[110] Brunton, S. L., Noack, B. R. & Koumoutsakos, P., 2020 Machine learning for fluid mechanics. *Annual Review of Fluid Mechanics* **52**, 477–508.

[111] Kutz, J. N., 2017 Deep learning in fluid dynamics. *Journal of Fluid Mechanics* **814**, 1–4.

[112] Cheng, J., Yuan, G., Zhou, M., Gao, S., Liu, C. & Duan, H., 2019 A fluid mechanics-based data flow model to estimate vanet capacity. *IEEE Transactions on Intelligent Transportation Systems* **21**, 2603–2614.

[113] Mäkinen, R. A., Périaux, J. & Toivanen, J., 1999 Multidisciplinary shape optimization in aerodynamics and electromagnetics using genetic algorithms. *International Journal for Numerical Methods in Fluids* **30**, 149–159.

[114] Obayashi, S., Sasaki, D., Takeguchi, Y. & Hirose, N., 2000 Multiobjective evolutionary computation for supersonic wing-shape optimization. *IEEE transactions on evolutionary computation* **4**, 182–187.

[115] Teo, C., Lim, K., Hong, G. & Yeo, M., 1991 A neural net approach in analyzing photograph in piv. In *Conference Proceedings 1991 IEEE International Conference on Systems, Man, and Cybernetics*, pp. 1535–1538. IEEE.

[116] Grant, I. & Pan, X., 1995 An investigation of the performance of multi layer, neural networks applied to the analysis of piv images. *Experiments in Fluids* **19**, 159–166.

[117] Raissi, M., Yazdani, A. & Karniadakis, G. E., 2020 Hidden fluid mechanics: Learning velocity and pressure fields from flow visualizations. *Science* **367**, 1026–1030.

[118] Yarlanki, S., Rajendran, B. & Hamann, H., 2012 Estimation of turbulence closure coefficients for data centers using machine learning algorithms. In *13th InterSociety Conference on Thermal and Thermomechanical Phenomena in Electronic Systems*, pp. 38–42. IEEE.

[119] Tracey, B. D., Duraisamy, K. & Alonso, J. J., 2015 A machine learning strategy to assist turbulence model development. In *53rd AIAA aerospace sciences meeting*, p. 1287.

[120] Zhang, Z. J. & Duraisamy, K., 2015 Machine learning methods for data-driven turbulence modeling. In *22nd AIAA Computational Fluid Dynamics Conference*, p. 2460.

[121] Wu, J.-L., Xiao, H. & Paterson, E., 2018 Physics-informed machine learning approach for augmenting turbulence models: A comprehensive framework. *Physical Review Fluids* **3**, 074602.

[122] Yu, Y., Abadi, M., Barham, P., Brevdo, E., Burrows, M., Davis, A., Dean, J., Ghemawat, S., Harley, T., Hawkins, P. *et al.*, 2018 Dynamic control flow in large-scale machine learning. In *Proceedings of the Thirteenth EuroSys Conference*, pp. 1–15.

[123] Gautier, N., Aider, J.-L., Duriez, T., Noack, B., Segond, M. & Abel, M., 2015 Closed-loop separation control using machine learning. *Journal of Fluid Mechanics* **770**, 442–457.

[124] Ren, F., Hu, H.-b. & Tang, H., 2020 Active flow control using machine learning: A brief review. *Journal of Hydrodynamics* **32**, 247–253.

[125] Lashkaripour, A., Rodriguez, C., Mehdipour, N., Mardian, R., McIntyre, D., Ortiz, L., Campbell, J. & Densmore, D., 2021 Machine learning enables design automation of microfluidic flow-focusing droplet generation. *Nature communications* **12**, 1–14.

[126] Shi, J., Song, J., Song, B. & Lu, W. F., 2019 Multi-objective optimization design through machine learning for drop-on-demand bioprinting. *Engineering* **5**, 586–593.

[127] Movahednejad, E., Ommi, F., Hosseinalipour, S., Chen, C. & Mahdavi, S., 2011 Application of maximum entropy method for droplet size distribution prediction using instability analysis of liquid sheet. *Heat and mass transfer* **47**, 1591.

[128] Um, K., Hu, X. & Thuerey, N., 2018 Liquid splash modeling with neural networks. In *Computer Graphics Forum*, volume 37, pp. 171–182. Wiley Online Library.

[129] Slevin, C. J. & Unwin, P. R., 1997 Measurement of liquid/liquid interfacial kinetics by directly probing the concentration profiles at expanding droplets. *Langmuir* **13**, 4799–4803.

[130] Oroian, M., 2013 Measurement, prediction and correlation of density, viscosity, surface tension and ultrasonic velocity of different honey types at different temperatures. *Journal of Food Engineering* **119**, 167–172.

[131] Dietterich, T. G., 2002. Ensemble learning, the handbook of brain theory and neural networks, ma arbib.

[132] Alam, M. E. & Samanta, B., 2017 Empirical mode decomposition of eeg signals for brain computer interface. In *SoutheastCon 2017*, pp. 1–6. IEEE.

[133] Alam, M. E. & Samanta, B., 2017 Performance evaluation of empirical mode decomposition for eeg artifact removal. In *ASME 2017 International Mechanical Engineering Congress and Exposition*, pp. V04BT05A024–V04BT05A024. American Society of Mechanical Engineers.

[134] Elith, J., Leathwick, J. R. & Hastie, T., 2008 A working guide to boosted regression trees. *Journal of Animal Ecology* **77**, 802–813.

[135] Alam, M. E., Smith, N., Watson, D., Hassan, T. & Neupane, K., 2019 Early screening of ddh using svm classification. In *2019 SoutheastCon*, pp. 1–4. IEEE.

[136] Hmeidi, I., Hawashin, B. & El-Qawasmeh, E., 2008 Performance of knn and svm classifiers on full word arabic articles. *Advanced Engineering Informatics* **22**, 106–111.

[137] Hua, J., Xiong, Z., Lowey, J., Suh, E. & Dougherty, E. R., 2005 Optimal number of features as a function of sample size for various classification rules. *Bioinformatics* **21**, 1509–1515.

[138] Cortes, C., Mohri, M. & Rostamizadeh, A., 2012 L2 regularization for learning kernels. *arXiv preprint arXiv:1205.2653* .

[139] Ruta, D. & Gabrys, B., 2005 Classifier selection for majority voting. *Information fusion* **6**, 63–81.

[140] Yang, L., 2011 Classifiers selection for ensemble learning based on accuracy and diversity. *Procedia Engineering* **15**, 4266–4270.

[141] Quinlan, J. R. *et al.*, 1996 Bagging, boosting, and c4. 5. In *AAAI/IAAI, Vol. 1*, pp. 725–730.

[142] Bühlmann, P., Yu, B. *et al.*, 2002 Analyzing bagging. *The Annals of Statistics* **30**, 927–961.

[143] Breiman, L., 1996 Bagging predictors. *Machine learning* **24**, 123–140.

[144] Skurichina, M., Kuncheva, L. I. & Duin, R. P., 2002 Bagging and boosting for the nearest mean classifier: Effects of sample size on diversity and accuracy. In *International Workshop on Multiple Classifier Systems*, pp. 62–71. Springer.

[145] Lawson, C. L. & Hanson, R. J., 1995 *Solving least squares problems*, volume 15. Siam.

[146] Gorry, P. A., 1990 General least-squares smoothing and differentiation by the convolution (savitzky-golay) method. *Analytical Chemistry* **62**, 570–573.

[147] Pasandideh-Fard, M., Qiao, Y., Chandra, S. & Mostaghimi, J., 1996 Capillary effects during droplet impact on a solid surface. *Physics of Fluids* **8**, 650–659.

[148] Fertis, D. G., 2006 *Nonlinear structural engineering*. Springer.

[149] Meirovitch, L., 1997 *Principles and Techniques of Vibrations*. Upper Saddle River, NJ: Prentice Hall.

[150] Erfanul Alam, M. & Dickerson, A. K., 2021 Sessile liquid drops damp vibrating structures. *Physics of Fluids* **33**, 062113.

[151] Loudon, C. & Tordesillas, A., 1998 The use of the dimensionless womersley number to characterize the unsteady nature of internal flow. *Journal of theoretical biology* **191**, 63–78.

[152] Blake, T. D., 2006 The physics of moving wetting lines. *Journal of colloid and interface science* **299**, 1–13.

[153] Voué, M., Rioboo, R., Adao, M., Conti, J., Bondar, A., Ivanov, D. A., Blake, T. D. & De Coninck, J., 2007 Contact-line friction of liquid drops on self-assembled monolayers: Chain-length effects. *Langmuir* **23**, 4695–4699.

[154] Chini, S. F., Bertola, V. & Amirfazli, A., 2013 A methodology to determine the adhesion force of arbitrarily shaped drops with convex contact lines. *Colloids and Surfaces A: Physicochemical and Engineering Aspects* **436**, 425–433.

[155] Brown, R., Orr Jr, F. & Scriven, L., 1980 Static drop on an inclined plate: analysis by the finite element method. *Journal of Colloid and Interface Science* **73**, 76–87.

[156] Carre, A. & Shanahan, M. E., 1995 Drop motion on an inclined plane and evaluation of hydrophobia treatments to glass. *The Journal of Adhesion* **49**, 177–185.

[157] Macdougall, G. & Ockrent, C., 1942 Surface energy relations in liquid/solid systems i. the adhesion of liquids to solids and a new method of determining the surface tension of liquids. *Proc. R. Soc. Lond. A* **180**, 151–173.

[158] Yadav, P. S., Bahadur, P., Tadmor, R., Chaurasia, K. & Leh, A., 2008 Drop retention force as a function of drop size. *Langmuir* **24**, 3181–3184.

[159] Extrand, C. & Gent, A., 1990 Retention of liquid drops by solid surfaces. *Journal of Colloid and Interface Science* **138**, 431–442.

[160] Annapragada, S. R., Murthy, J. Y. & Garimella, S. V., 2012 Droplet retention on an incline. *International Journal of Heat and Mass Transfer* **55**, 1457–1465.

[161] Kim, Y. H., Kim, K. & Jeong, J. H., 2016 Determination of the adhesion energy of liquid droplets on a hydrophobic flat surface considering the contact area. *International Journal of Heat and Mass Transfer* **102**, 826–832.

[162] Chen, K. S., Hickner, M. A. & Noble, D. R., 2005 Simplified models for predicting the onset of liquid water droplet instability at the gas diffusion layer/gas flow channel interface. *International Journal of Energy Research* **29**, 1113–1132.

[163] Zahidi, A. A. A., Lau, C. Y., Katariya, M., Liew, O. W. & Ng, T. W., 2017 Characteristics of drops on flat microplating surfaces from controlled upward longitudinal impact. *Colloids and Surfaces A: Physicochemical and Engineering Aspects* **522**, 74–82.

[164] James, A., Smith, M. & Glezer, A., 2003 Vibration-induced drop atomization and the numerical simulation of low-frequency single-droplet ejection. *Journal of Fluid Mechanics* **476**, 29–62.

[165] Tate, T., 1864 Xxx. on the magnitude of a drop of liquid formed under different circumstances. *The London, Edinburgh, and Dublin Philosophical Magazine and Journal of Science* **27**, 176–180.

[166] West, B. J., Bhargava, V. & Goldberger, A., 1986 Beyond the principle of similitude: renormalization in the bronchial tree. *Journal of Applied Physiology* **60**, 1089–1097.

[167] Dickerson, A. K., Mills, Z. G. & Hu, D. L., 2012 Wet mammals shake at tuned frequencies to dry. *Journal of the Royal Society Interface* **9**, 3208–3218.

[168] Tadmor, R., 2004 Line energy and the relation between advancing, receding, and young contact angles. *Langmuir* **20**, 7659–7664.

[169] Dickerson, A. K., Shankles, P. G. & Hu, D. L., 2014 Raindrops push and splash flying insects. *Physics of Fluids* **26**, 027104.

[170] Wang, T., Lee, S. & Zienkiewicz, O., 1961 A numerical analysis of large deflections of beams. *International Journal of Mechanical Sciences* **3**, 219–228.

[171] Denman, H. H. & Schmidt, R., 1970 An approximate method of analysis of large deflections. *Zeitschrift für angewandte Mathematik und Physik ZAMP* **21**, 412–421.

[172] Hsiao, K. M. & Hou, F. Y., 1987 Nonlinear finite element analysis of elastic frames. *Computers & structures* **26**, 693–701.

[173] Tada, Y. & Lee, G. C., 1970 Finite element solution to an elastica problem of beams. *International Journal for Numerical Methods in Engineering* **2**, 229–241.

[174] Belytschko, T., Lu, Y. Y. & Gu, L., 1994 Element-free galerkin methods. *International journal for numerical methods in engineering* **37**, 229–256.

[175] Garreta, R. & Moncecchi, G., 2013 *Learning scikit-learn: machine learning in python*. Packt Publishing Ltd.

[176] Staelin, C., 2003 Parameter selection for support vector machines. *Hewlett-Packard Company, Tech. Rep. HPL-2002-354R1* **1**.

[177] Altmann, A., Toloşi, L., Sander, O. & Lengauer, T., 2010 Permutation importance: a corrected feature importance measure. *Bioinformatics* **26**, 1340–1347.

[178] Liaw, A., Wiener, M. *et al.*, 2002 Classification and regression by randomforest. *R news* **2**, 18–22.

[179] Shi, T. & Horvath, S., 2006 Unsupervised learning with random forest predictors. *Journal of Computational and Graphical Statistics* **15**, 118–138.

[180] Natekin, A. & Knoll, A., 2013 Gradient boosting machines, a tutorial. *Frontiers in neurorobotics* **7**, 21.

[181] Chen, T., He, T., Benesty, M., Khotilovich, V., Tang, Y., Cho, H. *et al.*, 2015 Xgboost: extreme gradient boosting. *R package version 0.4-2* **1**.

[182] Ke, G., Meng, Q., Finley, T., Wang, T., Chen, W., Ma, W., Ye, Q. & Liu, T.-Y., 2017 Lightgbm: A highly efficient gradient boosting decision tree. In *Advances in neural information processing systems*, pp. 3146–3154.

[183] Dudani, S. A., 1976 The distance-weighted k-nearest-neighbor rule. *IEEE Transactions on Systems, Man, and Cybernetics* pp. 325–327.

[184] Keller, J. M., Gray, M. R. & Givens, J. A., 1985 A fuzzy k-nearest neighbor algorithm. *IEEE transactions on systems, man, and cybernetics* pp. 580–585.

[185] Kotsiantis, S. B., Zaharakis, I. & Pintelas, P., 2007 Supervised machine learning: A review of classification techniques. *Emerging artificial intelligence applications in computer engineering* **160**, 3–24.

[186] Camps-Valls, G. & Bruzzone, L., 2005 Kernel-based methods for hyperspectral image classification. *IEEE Transactions on Geoscience and Remote Sensing* **43**, 1351–1362.

[187] Hoerl, A. E. & Kennard, R. W., 1970 Ridge regression: Biased estimation for nonorthogonal problems. *Technometrics* **12**, 55–67.

[188] Tax, D. M., Van Breukelen, M., Duin, R. P. & Kittler, J., 2000 Combining multiple classifiers by averaging or by multiplying? *Pattern recognition* **33**, 1475–1485.

[189] Saeys, Y., Abeel, T. & Van de Peer, Y., 2008 Robust feature selection using ensemble feature selection techniques. In *Joint European Conference on Machine Learning and Knowledge Discovery in Databases*, pp. 313–325. Springer.

[190] Chandra, S. & Avedisian, C., 1991 On the collision of a droplet with a solid surface. *Proceedings: Mathematical and Physical Sciences* **432**, 13–41. ISSN 0962-8444.